LOW-THRUST TRAJECTORY DESIGN FOR TOURS OF THE MARTIAN MOONS

by

Beom Park

A Thesis

Submitted to the Faculty of Purdue University

In Partial Fulfillment of the Requirements for the degree of

Master of Science

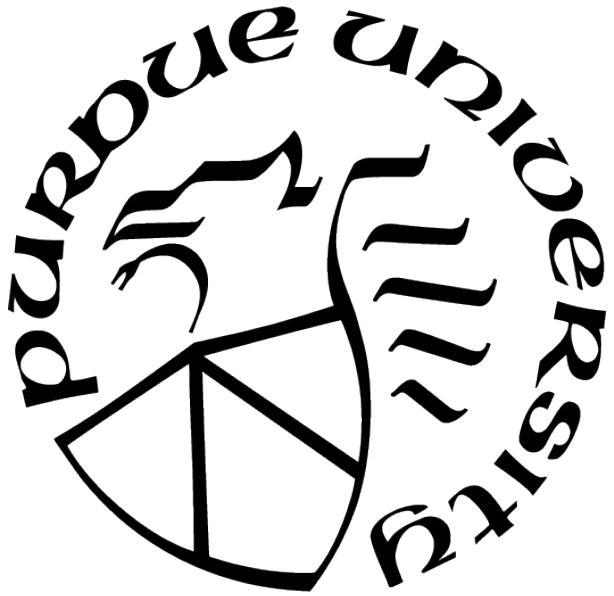

School of Aeronautics and Astronautics

West Lafayette, Indiana

May 2021

THE PURDUE UNIVERSITY GRADUATE SCHOOL
STATEMENT OF COMMITTEE APPROVAL

Dr. Kathleen Howell, Chair

School of Aeronautics and Astronautics

Dr. James Longuski

School of Aeronautics and Astronautics

Dr. Carolin Frueh

School of Aeronautics and Astronautics

Approved by:

Dr. Gregory Blaisdell

ACKNOWLEDGMENTS

First, I would like to thank the people that I love. 아버지, 어머니, 두 분의 지원과 격려가 없었으면 여기까지 오지 못했을 거에요. 우리 집에서 태어난 게 제 인생 최고의 행운이에요. 형, 사소한 레이텍 질문부터 인생 고민까지, 전천후 멘토가 되어주느라 고생이 많아. "우리" 야, 내 꿈을 이해해주고 기다려줘서 고마워. 특히 힘들었던 이번 학기 내내 응원해준 덕분에 무사히 졸업할 수 있었어.

I would like to extend the gratitude towards my advisor, Professor Kathleen C. Howell. I am forever grateful for the opportunities that you have given me. This work would not have been feasible without your guidance and support. Your passion for the field, both as a researcher and a teacher, is truly inspirational, and I am fortunate to serve you as your student as well as teaching assistant. I am excited to continue to learn from you, and I look forward to what we will discover in the future.

Next, I would like to acknowledge my friends, both in the States and back at home. I am grateful to the past and current members of the Multi-Body Dynamics Research Group for your help, feedback, and encouragement. In particular, this research owes much to Robert's past work on direct collocation, the collaborative work with David and Maaninee on the Martian moons tour, and Kenza and Juan's research on the Earth-Mars mission design.

I would also like to thank my committee members, Professor James Longuski and Professor Carolin Frueh. Thank you for reviewing the document and your valuable feedback during the defense. Finally, I would like to thank the Purdue School of Aeronautics and Astronautics and the Kwanjeong Educational Foundation for the financial support.

TABLE OF CONTENTS

LIST OF TABLES

LIST OF FIGURES

ABSTRACT

While the interest in the Martian moons increases, the low-thrust propulsion technology is expected to enable novel mission scenarios but is associated with unique trajectory design challenges. Accordingly, the current investigation introduces a multi-phase low-thrust design framework. The trajectory of a potential spacecraft that departs from the Earth vicinity to reach both of the Martian moons, is divided into four phases. To describe the motion of the spacecraft under the influence of gravitational bodies, the two-body problem (2BP) and the Circular-Restricted Three Body Problem (CR3BP) are employed as lower-fidelity models, from which the results are validated in a higher-fidelity ephemeris model. For the computation and optimization of low-thrust trajectories, direct collocation algorithm is introduced. Utilizing the dynamical models and the numerical scheme, the low-thrust trajectory design challenge associated each phase is located and tackled separately. For the heliocentric leg, multiple optimal control problems are formulated between the planets in heliocentric space over different departure and arrival epochs. A contour plot is then generated to illustrate the trade-off between the propellant consumption and the time of flight. For the tour of the Martian moons, the science orbits for both moons are defined. Then, a new algorithm that interfaces the Q-law guidance scheme and direct collocation algorithm is introduced to generate low-thrust transfer trajectories between the science orbits. Finally, an end-to-end trajectory is produced by merging the piece-wise solutions from each phase. The validity of the introduced multi-phase formulation is confirmed by converging the trajectories in a higher-fidelity ephemeris model.

1. INTRODUCTION

The natural satellites of Mars, Phobos and Deimos, are appealing destinations for future space explorations. Characterizing the physical composition of Phobos and Deimos is considered a key to solving various questions about the Martian system [1]. For instance, the origin of the Martian moons remains mysterious, while the two compelling hypotheses suggest the moons results from capture of asteroids or from formation in situ by either co-accretion or by a giant impact on Mars [2]. The observations and sample returns from the future explorations are expected to confirm one of the two scenarios, and deliver additional valuable insights. If the moons are captured asteroids, they will offer information on the process of delivering organic substances and water to the terrestrial planets [3]. Alternatively, if the composition supports the in situ hypothesis, the moons are witness to the formation of the Martian system as the materials of the moons record the early history of Mars [1]. The Martian moons are envisioned as key to the future of human exploration of Mars as well. The moons may serve as bases for teleoperations as part of robotic exploration missions on Mars. Manned missions to the moons may act as relatively low-risk stepping stones prior to eventually reaching the surface of Mars [4]. Additionally, the early observations of Phobos suggests the possibility of iced water on Phobos [5], a hypothesis that remains inconclusive [6]. If further observations of the moons confirm the existence of in situ resources including hydrogen, oxygen, and carbon, these may be extracted to enable a smaller spacecraft, leading to a cheaper configuration for human exploration missions [7], [8].

Despite the importance of the Martian moons in both planetary science and human exploration of the Martian system, no dedicated mission has successfully explored the moons [2]. In 1988, the first dedicated mission, Phobos 2, acquired 37 photos of the surface of Phobos [9] but the contact with the spacecraft was lost during its maneuver to encounter the moon. The observation of the Martian moons has subsequently been conducted solely with Earth-based telescopes and Mars orbiters or landers [2], including the Mars Express mission that measured Phobos' gravity field with multiple Phobos flybys in 2010 [6]. In the past decade, recognizing the importance of both moons, an increasing number of missions that primarily target Phobos and Deimos have been proposed by multiple space agencies. The proposed

missions include Phootprint from the European Space Agency (ESA) [10], PADME and PANDORA from the National Aeronautics and Space Administration (NASA) [11], [12], and MMX from the Japanese Aerospace eXploration Agency (JAXA) [13]. While Phobos is considered the primary target in most of the previous mission concepts, mainly due to the proximity to the red planet [14], a number of proposed missions include the exploration of both Phobos and Deimos [11], [13].

For the exploration of deep space, chemical engines that are capable of imparting large acceleration to the spacecraft over a short period of time are traditionally used. More recently, low-thrust propulsion has emerged, where the engine provides a fuel efficient maneuver but with the acceleration of a small magnitude, hence, low-thrust. The low-thrust propulsion has been tested in a number of missions from multiple space agencies, including NASA's Deep Space 1, JAXA's Hayabusa-1, and ESA's SMART-1, proving the effectiveness of the technology in both cislunar and deep space [15]–[17]. In particular, NASA's Dawn mission utilized a Mars flyby with a low-thrust engine to finally arrive at the dwarf planets Vesta and Ceres [18] and proved that low-thrust propulsion is applicable to the exploration of the Martian system. The largest benefit of the low-thrust propulsion is the efficiency of the engine, represented by a high specific impulsive in comparison to a chemical engine [19]. The efficiency allows for designing a mission to the Martian system with a smaller spacecraft and, thus, a mission with a cheaper configuration as envisioned by previous authors [20]–[22]. Accordingly, strategies the low-thrust trajectory design that are well-suited to a potential mission that explores the Martian moons, are in demand.

1.1 Low-Thrust Trajectory Design Factors and Assumptions

This investigation focuses on the trajectory design process for a potential mission scenario where both of the Martian moons are explored by a spacecraft with low-thrust propulsion capabilities. The design process depends upon with some associated challenges and assumptions as listed in Table 1.1. The focus of the current work involves the multi-body dynamics aspect of the problem, i.e., a variety of celestial bodies including the Sun, the planets, and the Martian moons that all exert gravitational forces on the spacecraft. Such a complex gravitational environment as the spacecraft moves from the Earth to the Martian moons

compounds the trajectory design process. A multi-phase approach is typically employed to address this challenge [22]–[27], where the problem is divided into smaller parts, or phases. The phases are defined via a number of criteria, including a shift in recognizing the most significant gravitational bodies depending on the location of the spacecraft. This strategy is advantageous since it allows analyses that are more tractable as the gravitational bodies with the most influence on the spacecraft are fixed within each phase. Such a strategy greatly reduces the complexity of the problem.

The multi-phase formulation in the current investigation is illustrated in Figure 1.1, where the problem is decomposed into four distinct phases: (1) departure, (2) heliocentric leg, (3) arrival, and (4) tour of the Martian moons. The first phase, departure, corresponds to the Earth vicinity where the Earth and the Sun have a strong impact on the spacecraft trajectory; the spacecraft is expected to escape from the Earth gravity field to heliocentric space. The second phase, the heliocentric leg, is the region where the gravitational force on the spacecraft is dominated by the Sun, and the spacecraft traverses from the Earth vicinity to the Mars vicinity in the heliocentric space. The third phase corresponds to the vicinity of the Martian system where the spacecraft is most influenced by the gravity of the Sun and Mars and is expected to be captured into orbit about Mars. Finally, the tour of the Martian moons is accommodated in the fourth phase, where the gravity of the Sun, Mars, or even the Martian moons may be incorporated as required. After decomposing the trajectory into multiple phases, the design challenge for each phase is identified and tackled separately. The scope of the current investigation lies in the second through the fourth phases, the heliocentric leg and a tour of the Martian moons. The heliocentric leg refers to the transfer trajectory between the Earth and Mars in heliocentric space, where the challenge is associated with characterizing the optimal heliocentric trajectories that depend on the locations of the planets, i.e., the Earth and Mars, over different epochs. It is assumed that the flybys of the Moon or the planets do not occur, although the flybys can be utilized to compute propellant efficient trajectories [28], [29]. For the fourth phase, the challenge arises from the fact that the transfer trajectory between the Martian moons requires multiple revolutions around Mars and also an additional rendezvous constraint that exists when the spacecraft departs from one of the moons and finally arrives at the second moon. The first and third

phases, i.e., departure and arrival, remain out of the scope of the current investigation, and a simplifying assumption is introduced. They share a common trait that many-revolution spiral arcs around the planets are required when the spacecraft departs from the Earth and arrives at Mars, as a low-thrust engine typically requires longer time of flight to achieve the change in energy to either escape from or be captured by gravity of the planets. Although multiple strategies are available to compute the planetocentric low-thrust trajectories [30], a trade-off generally exists between the time of flight and the propellant consumption for the optimal spiral arcs [31]. In the current investigation, simple control laws are introduced to avoid optimizing the multi-revolution arcs around the Earth and Mars. For the departure, the thrust is fixed at the maximum value while the direction is aligned with the rotating velocity. Similarly, for the arrival, the thrust level is also fixed at the maximum value but the direction is in the opposite of the rotating velocity. These control strategies represent a near time-optimal solutions given an energy gap, and provide useful reference costs for phase 1 and 3 without navigating the trade-off between the time of flight and the propellant consumption.

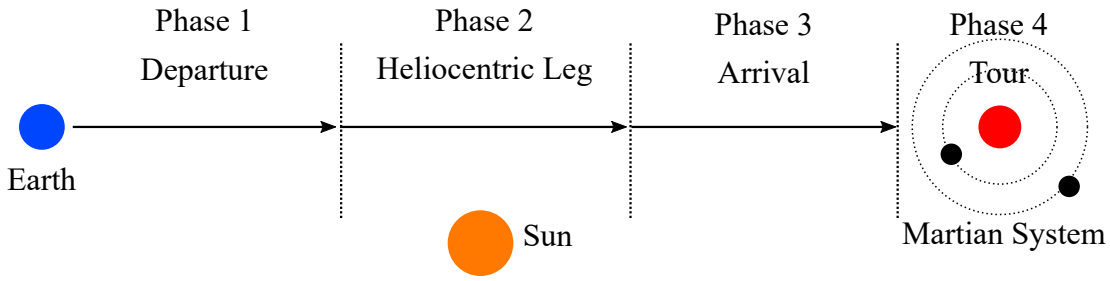

Figure 1.1. Multi-phase formulation of the trajectory design process

In addition to the multi-body dynamics aspect of the problem to explore the Martian moons, the trajectory design also depends on the departure or deployment state near the Earth. While various launch vehicles result in different departure states, the current analysis assumes one particular scenario: the spacecraft is launched as a secondary payload attached to an Evolved Expendable Launch Vehicle (EELV) Secondary Payload Adapter (ESPA) where the launch reaches a geostationary transfer orbit (GTO). This scenario corresponds to one of the novel mission concepts enabled by the low-thrust propulsion technology, and is envisioned as one of the cheapest configurations for the mission concepts in the current decade

[20]. The benefits include the flexibility offered by lacking a requirement for a dedicated launch vehicle, and also the frequent launch opportunities to the GTO, more than 10 launches per year [22].

Finally, the low-thrust propulsion capability poses additional challenges to the trajectory design process despite its benefits from increased efficiency. In contrast to a chemical engine where the trajectory is generated without considering the engine specifications, the low-thrust trajectory is bound to the spacecraft characteristics including the thrust, mass and the specific impulse. The current investigation is based on the specifications introduced by Woolley and Olikara [22], listed in Table 1.2. The numbers in Table 1.2 correspond to a realistic set of values for a spacecraft that departs from a GTO as a secondary payload and is delivered to an Areostationary orbit around Mars, solely utilizing low-thrust propulsion. When the second and fourth phases are designed independently following the multi-phase formulation, the spacecraft mass at the beginning of these phases are assumed to be $340.9kg$ and $229.3kg$, respectively. The specific impulse and maximum thrust values of the engine are consistent with the values listed in Table 1.2, $1733s$ and $90mN$, respectively. It is assumed that these values do not depend on the spacecraft power.

Table 1.1. Low-thrust trajectory design factors and respective assumptions

Design Factors	Assumptions
Multi-body dynamics	Multi-phase approach illustrated in Figure 1.1
	Phase 2: No lunar/planetary flybys
	Phase 1 and 3: Sub-optimal control law
Earth Departure Scenario	Secondary payload, GTO departure
Spacecraft Specifications	Table 1.2

Table 1.2. Spacecraft specifications (recreated from Woolley and Olikara [22] Table 1 and Figure 11)

Spacecraft Specifications		Value
Mass	Beginning of Phase 1	409.3kg
	Beginning of Phase 2	340.9kg
	Beginning of Phase 3	243.1kg
	Beginning of Phase 4	229.3kg
Specific Impulse		1733s
Maximum Thrust		90mN

1.2 Problem Definition and Previous Contributions

The overarching goal of the current investigation is the development of a multi-phase design framework for low-thrust trajectories that originate from the Earth and reach both of the Martian moons. The goal is subdivided into the following objectives:

1. Characterize the optimal transfer trajectories between the Earth and Mars (Phase 2).

2. Develop a strategy to generate tour trajectories to explore both Phobos and Deimos (Phase 4). Validate the strategy with multiple scenarios and assess the reference costs.

3. Generate sample end-to-end trajectories by collecting strategies for each phase and validating the multi-phase approach described in Figure 1.1.

Recall that the current investigation is bound to the assumptions listed in Table 1.1.

The formulation and the various analyses conducted within this investigation expand on existing methodologies. The direct collocation algorithm is the basic computational tool in the current investigation to produce the feasible, as well as optimal, low-thrust trajectories. Direct collocation is leveraged for low-thrust trajectory design by a number of previous authors [32], [33], recognized for its robustness, i.e., the ability to locate solutions even with poor initial guesses, and the computational efficiency of the solvers that are available [34]. Applying the direct collocation algorithm to a low-thrust trajectory design is very useful and, yet continue as an ongoing research field. Efforts are also underway to optimize trajectories in the complex dynamical regimes, where it is often challenging to generate a suitable initial guess. Ozimek et al. [35] compute non-Keplerian orbits around the Moon that provide constant line-of-sight to the lunar pole while considering the gravity force from multiple celestial bodies utilizing the direct collocation algorithm. Parrish et al. [36], as well as Pritchett et al. [37], demonstrate the robustness of direct collocation in the Earth-Moon multi-body dynamics regime. The robustness of the algorithm is leveraged in the current investigation to achieve the research objectives, where the exact form of the implementation is heavily based on the algorithm developed and refined by Pritchett et al. [37].

For the heliocentric leg between the Earth and Mars, or the second phase in the multi-phase formulation, attempts to characterize the family of optimal trajectories aid the prelim-

inary mission design process. Graphical tools that demonstrate the overall costs associated with the optimal trajectories, those that depend on different departure and arrival dates, are developed by various authors. Woolley et al. [38] present contour plots, termed "bacon plots", of the optimal trajectories between the Earth and Mars via MALTO, a fast, medium-fidelity optimizer developed at Jet Propulsion Laboratory (JPL), where the continuous thrust is approximated as a series of impulsive maneuvers [39] and optimized with SNOPT [40], a nonlinear programming (NLP) solver. Genta and Maffione [23] present analogous contour plots labelled "J-plots", based on an in-house MATLAB package that utilizes the Euler-Lagrange method to compute the optimal transfer trajectories [41]. The current investigation reconfirms the results from the previous works with the direct collocation algorithm.

The fourth phase in the multi-phase formulation, i.e., the tour of the Martian moons with low-thrust, requires multiple revolutions around Mars as well as an additional rendezvous constraint. There exist multiple attempts to solve this many-revolution problem combined with the terminal rendezvous constraint. Dachwald [42] as well as Cremaschi et al. [43] introduce an evolutionary neurocontroller that consists of a inner loop neurocontroller for which the parameters are optimized through an evolutionary algorithm. The rendezvous scenario is examined for the Earth to Mercury transfer as well as the tour of the Jovian moons. Based on Dachwald's algorithm, Derz et al. [44] generate a rendezvous trajectory between Deimos and Phobos, where the authors note that "the demanding rendezvous constraints resulted in a very high computational effort". More recently, Lantoine and Russell [45] introduce a hybrid differential dynamic programming algorithm and demonstrate it on a mission scenario with sequential flybys of multiple asteroids as well as the rendezvous constraint with the final target. Although the low-thrust engine acceleration is modeled as a series of impulsive maneuvers and the trajectories are comprised of a dozen of revolutions around the central body. Building on this work, Aziz [46] incorporates the eclipse constraint into the algorithm and presents a Earth to Mars rendezvous scenario, but does not demonstrate the rendezvous performance on a many-revolutions transfer. Zhibo and Guzzetti [47] offer a simplectic method that is applicable to rendezvous problem in the low-Earth orbit regime and associated with 228 revolutions while incorporating the gravity from the Earth including

the J2 perturbation. The authors note that the method converged to an optimal solution with a good initial guess. The current investigation introduces an alternative method where the Q-law algorithm, developed by Petropoulos [48], is employed as an initial guess to the direct collocation algorithm.

1.3 Document Overview

The current investigation expands upon the work of the previous authors to develop a multi-phase design framework suitable for missions to Martian moon with low-thrust propulsion. This document presents the dynamical models as well as the optimization algorithm utilized to fulfill the research objectives, followed by the analyses corresponding to each phase of the multi-phase formulation. The rest of the document is organized as follows:

- Chapter 2: Dynamical Models

  The assumptions for the dynamical models utilized in the current investigation are introduced. While the gravitational force is generally described by the $\mathcal{N}$-Body problem, two low-fidelity models, the two-body problem (2BP) and circular restricted three body problem (CR3BP) are included to facilitate tractable analysis. The equations of motion for the higher-fidelity ephemeris model are provided, with which the results from the low-fidelity models are validated. The definitions of coordinate frames as well as the rotations between the frames are discussed. Finally, the low-thrust engine model is introduced, completing the dynamical models in the current work.

- Chapter 3: Low-Thrust Trajectory Computation and Optimization Via Direct Collocation.

  The computational tools to generate and optimize low-thrust trajectories are introduced. A collocation integration scheme is described, that serves as the numerical integrator for the differential equations representing the dynamical models. The Newton-Raphson scheme serves as a core algorithm to implement differential corrections and produce feasible trajectories. Then, the optimal control problem is defined, where the direct collocation algorithm is introduced as the selected approach. An illustrative example of this process for the low-thrust trajectory design is presented.

- Chapter 4 Heliocentric Leg Design

  The process of characterizing the optimal trajectories between the Earth and Mars (Phase 2) is explained. The initial guess is obtained via a third degree polynomial approximation and a continuations scheme. The initial guess is optimized, and the results corresponding to a range of departure and arrival epochs are represented in contour plots. Discussions regarding the characteristics of the contour plots are provided.

- Chapter 5 Martian Moons Tour Design

  First, the sequence for a moon tour is fixed. Initiailly, it is a sequence detailed to explore the Deimos before Phobos, deduced as the preferred option from the energy levels of the two moon orbits in the Sun-Mars CR3BP. The science orbits for the two moons are then defined, where libration point orbits are selected as capture orbits for the moons and resonant orbits in the Mars-Phobos and Mars-Deimos CR3BPs are selected as the flyby orbits. The tour scenarios are categorized into (1) capture-to-capture, (2) flyby-to-capture, (3) and capture-to-flyby. As the low-thrust engine requires many revolutions along the thrusting arcs to arrive at the Martian system as well as to transfer between the science orbits, the strategies to compute the spiral-down arcs are introduced. From the heliocentric leg to the Deimos science orbit (Phase 3), a simple control law to thrust in the opposite direction of the velocity is employed. From the Deimos science orbit to the Phobos science orbit (Phase 4), an algorithm that combines a Q-law guidance scheme and the direct collocation method is presented to tackle the additional challenges associated with the rendezvous requirement at the end of the arc. Finally, "costs" measured as the propellant consumption as well as the required time of flight are summarized for a number of options corresponding to each tour scenario.

- Chapter 6 End-to-end Trajectory Design

  The strategies introduced in the preceding chapters are collected to complete the multi-phase design framework. A simple control law to depart from a GTO (Phase 1) is discussed. Sample end-to-end trajectories originating from a GTO, that arrive at Phobos science orbits are generated.

- Chapter 7 Conclusions

  A summary of the results is presented with the concluding remarks, followed by recommendations for future work.

2. DYNAMICAL MODELS

A spacecraft that travels from the Earth vicinity to the Martian system is under the influence of a variety of forces: the gravity from various celestial bodies, any solar radiation pressure on the vehicle, the atmospheric drag in the vicinity of the planets, and potentially, the thrust from the engine at suitable times. These forces are mathematically described by appropriate dynamical models. A trade-off already exists between the simplicity and fidelity of any dynamical model, and a common practice is to neglect the forces of relatively small magnitudes. To avoid an overly complex model, it is advantageous to start with the simplest model that efficiently captures the governing forces. To this end, the forces influencing the spacecraft are simplified into two categories for the current work: (1) gravitational forces and (2) the low-thrust engine force. Each of these models and respective assumptions are detailed as follows.

2.1 Gravitational Force Models

All bodies are assumed to be centrobaric in this investigation, that is equivalent to a point-mass approximation for the celestial bodies. Following this assumption, further simplifications are necessary in the preliminary mission design process; considering too many bodies at once often results in chaos and poses a challenge. Instead, celestial bodies that exert insignificant gravitational forces on the spacecraft are initially ignored, resulting in a much simpler model that facilitates preliminary analysis. Then, the number of the bodies included in the model may be gradually increased to validate the preliminary result in a higher-fidelity model.

For instance, incorporating all the celestial bodies that a spacecraft may encounter while moving from the Earth to Mars results in a six-body problem including the Sun, both planets, both Martian moons as well as the spacecraft. While Mars and the moons do affect the spacecraft, they only exert negligible forces compared to the Sun and Earth in the vicinity of the Earth. Thus, in a lower-fidelity model, only the Sun and Earth may be incorporated to efficiently describe motion of the spacecraft in the vicinity of the Earth. The validity of this

preliminary analysis is ensured by reconverging the obtained trajectory with a higher-fidelity model that incorporates all five celestial bodies.

All gravitational models in the current investigation originate from a general $\mathcal{N}$-body problem. As the lower-fidelity models, the two-body problem and the circular restricted three-body problem (CR3BP) are introduced. Next, A higher-fidelity ephemeris model that integrates more bodies and captures the actual motion of the bodies is defined. The higher-fidelity ephemeris model, when combined with the low-thrust engine model, is assumed to be the true representation of the dynamics that govern the motion of the spacecraft.

2.1.1 $\mathcal{N}$-Body Problem

Under the assumption that all bodies are centrobaric, gravitational forces are most generally described in terms of the $\mathcal{N}$-Body Problem, where the system is comprised of $\mathcal{N}$ total bodies, under their mutual gravitational influences. A schematic of the $\mathcal{N}$-Body Problem is represented in Figure 2.1, where $P_1, P_2, ..., P_\mathcal{N}$ denote the bodies and $\bar{\bar{R}}_1, \bar{\bar{R}}_2, ..., \bar{\bar{R}}_\mathcal{N}$ refer to the position vectors that originate from an inertially fixed origin O to each respective body. The unit vectors $\hat{X}, \hat{Y}, \hat{Z}$ represent the directions associated with the inertial frame. Throughout the document, overbars indicate vectors, carets define vectors of unit magnitude, and tilde refers to dimensional quantities. By applying Newton's second law, the motion of

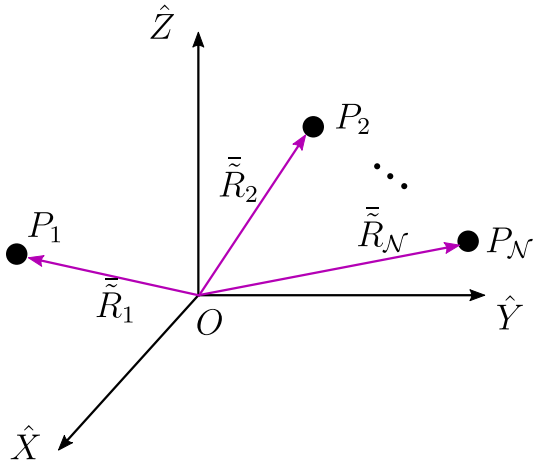

Figure 2.1. $\mathcal{N}$-Body problem schematic

any body in the system is described by a vector differential equation of the following form,

$$\tilde{m}_{\mathrm{i}} \frac{{}^{I}d^2\bar{\tilde{R}}_{\mathrm{i}}}{d\tilde{t}^2} = -\tilde{G} \sum_{\mathrm{j}=1,\, \mathrm{j}\neq\mathrm{i}}^{\mathcal{N}} \frac{\tilde{m}_{\mathrm{i}}\tilde{m}_{\mathrm{j}}}{\tilde{R}_{\mathrm{ji}}^3} \bar{R}_{\mathrm{ji}}, \tag{2.1}$$

where $\tilde{m}_{\mathrm{i}}, \tilde{m}_{\mathrm{j}}$ are the masses of $P_{\mathrm{i}}, P_{\mathrm{j}}$ for $1 \leq \mathrm{i}, \mathrm{j} \leq \mathcal{N}$, and $\tilde{G}$ is the universal gravitational constant, $\frac{{}^{I}d^2\bar{\tilde{R}}_{\mathrm{i}}}{d\tilde{t}^2}$ is the second derivative of the position vector $\bar{\tilde{R}}_{\mathrm{i}}$ with respect to the time, $\tilde{t}$. The superscript I denotes that the vector is differentiated with respect to an inertial observer. The vector $\bar{\tilde{R}}_{\mathrm{ji}}$ represents the relative position vector from P_{j} to P_{i}, or $\bar{\tilde{R}}_{\mathrm{ji}} = \bar{\tilde{R}}_{\mathrm{i}} - \bar{\tilde{R}}_{\mathrm{j}}$. The magnitude of the vector between P_{i} and P_{j}, or $|\bar{\tilde{R}}_{\mathrm{ij}}|$, is denoted by $\tilde{R}_{\mathrm{ji}}$. The minus sign on the right side of the equation represents that the gravitational force is an attractive force between any pair of bodies. While Equation (2.1) is general and written for any $\mathcal{N}$ bodies in the system, it is known that a closed-form of solution does not exist for $\mathcal{N} \geq 3$ [49]. For such cases, it is impossible to analytically express the motion for all $\mathcal{N}$ bodies and necessitates numerical simulations to describe the motion.

2.1.2 Two-Body Problem (2BP)

When $\mathcal{N} = 2$, Equation (2.1) results in two vector differential equations corresponding to $1 \leq \mathrm{i} \leq 2$. This pair of vector equations are rearranged into the following vector equation, governing the relative motion of P_2 with respect to P_1,

$$\frac{{}^{I}d^2\bar{\tilde{R}}_{12}}{d\tilde{t}^2} = -\tilde{G}\frac{\tilde{m}_1 + \tilde{m}_2}{\tilde{R}_{12}^3}\bar{\tilde{R}}_{12}, \tag{2.2}$$

where $\bar{\tilde{R}}_{12} = \bar{\tilde{R}}_2 - \bar{\tilde{R}}_1$, or the relative position vector from the first body P_1 to P_2. The vector differential equation (2.2) is integrated twice analytically, resulting in a closed-form solution [49]. The resulting trajectory for $\bar{\tilde{R}}_{12}$ is a conic arc, i.e., an ellipse, a parabola, or a hyperbola. Analytically solvable, six integrals of motion uniquely define the motion in the two-body problem: (1) semi-major axis, a_K, (2) eccentricity, e_K, (3) inclination, i_K, (4) right ascension of the ascending node, Ω_K, (5) argument of periapsis, ω_K, and (6) true anomaly, ν_K. These six parameters are also labelled Keplerian elements, or classical orbital elements. In the current analysis, the Sun-2BP approximation is a reasonable approximation

to generate an initial guess for the heliocentric leg that links the Earth and Mars. Similarly, the Mars-2BP generates an initial guess for the spiral trajectories that connect the Martian moons.

2.1.3 Circular Restricted Three-Body Problem (CR3BP)

Three-body problem, that is, when $\mathcal{N} = 3$, offers a chance to incorporate another gravitational force. To facilitate analysis, the circular restricted three-body problem (CR3BP) is formulated by introducing the following assumptions,

1. The mass of the third body is assumed to be infinitesimally small compared to the other two bodies. Or,

$$\tilde{m}_3 << \tilde{m}_1, \tilde{m}_2,$$

   where $\tilde{m}_1, \tilde{m}_2, \tilde{m}_3$ correspond to the masses of bodies P_1, P_2, P_3, respectively.

2. P_1 and P_2 move on circular orbits around their barycenter, denoted by B.

These assumptions alleviate the complexity associated with a general form of the three-body problem by assigning simple motions to P_1 and P_2; the numerical simulations are only required for the motion of P_3. The gravitational bodies P_1 and P_2 are denoted the "primaries", where P_1 is assumed to be the celestial body with a larger mass. From the first assumption, P_1 and P_2 form a 2BP where the motion of P_1 and P_2 is represented as a conic. By the second assumption, the conic becomes a circle, resulting in a more tractable motion. Figure 2.2 demonstrates a general configuration for the CR3BP. The primaries P_1 and P_2 move in circular orbits around the barycenter B. The inertial set of unit vectors $\hat{X} - \hat{Y} - \hat{Z}$ is defined so that $\hat{X}, \hat{Y}$ span the orbital plane of P_1 and P_2, and $\hat{Z}$ is the out-of-plane direction, parallel to primary orbital angular momentum vector, defined as $\hat{Z} = \hat{X} \times \hat{Y}$. A new rotating frame is defined, such that $\hat{x}$ is the direction originating from P_1 and pointing P_2, $\hat{z}$ is identical to $\hat{Z}$, and $\hat{y}$ is defined as the cross product of $\hat{z}$ and $\hat{x}$. The same frame is obtained by rotating the $\hat{X} - \hat{Y}$ vectors by θ with respect to $\hat{Z}$. Note that P_3 is allowed to move freely in space, including the out-of-plane direction, $\hat{z}$.

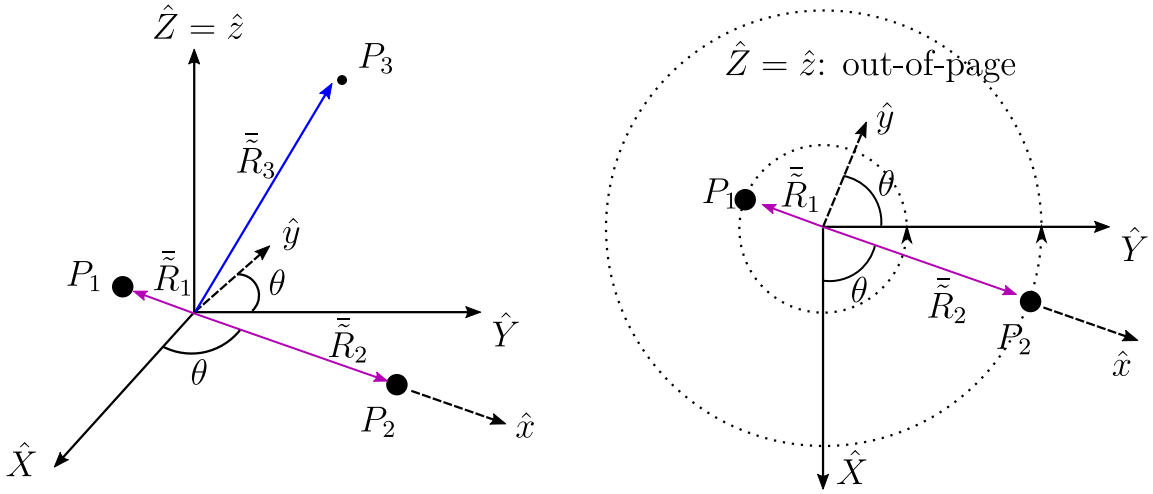

Figure 2.2. CR3BP schematic

The third body, or P_3, is often the spacecraft, of which the motion is described under the gravitation influence from the primaries. It starts with a vector differential equation obtained with Equation 2.1,

$$\frac{{}^{I}d^2\bar{\tilde{R}}_3}{d\tilde{t}^2} = -\tilde{G}\frac{\tilde{m}_1}{\tilde{R}_{13}^3}\bar{\tilde{R}}_{13} - \tilde{G}\frac{\tilde{m}_2}{\tilde{R}_{23}^3}\bar{\tilde{R}}_{23}, \tag{2.3}$$

where vectors $\bar{\tilde{R}}_{23} = \bar{\tilde{R}}_3 - \bar{\tilde{R}}_2$, $\bar{\tilde{R}}_{13} = \bar{\tilde{R}}_3 - \bar{\tilde{R}}_1$. It is known that when Equation (2.3) is written in the rotating frame, it results in a form that allows more insight into the dynamics. First, consider the position vector of the third body in the inertial frame,

$$\bar{\tilde{R}}_3 = \tilde{X}\hat{X} + \tilde{Y}\hat{Y} + \tilde{Z}\hat{Z}, \tag{2.4}$$

where $\tilde{X}, \tilde{Y}, \tilde{Z}$ denote the dimensional position components in the inertial directions. From Figure 2.2, the following equations relate the unit vectors in both frames,

$$\hat{x} = \cos(\theta)\hat{X} + \sin(\theta)\hat{Y} \tag{2.5}$$

$$\hat{y} = -\sin(\theta)\hat{X} + \cos(\theta)\hat{Y} \tag{2.6}$$

$$\hat{z} = \hat{Z}, \tag{2.7}$$

where the angle θ in Figure 2.2 denotes the orientation of the rotating frame unit vectors relative to the inertial frame. Using this relationship, the position vector of the third body in the rotating frame, $\bar{\tilde{r}}_3$, is obtained as,

$$\bar{\tilde{r}}_3 = \tilde{x}\hat{x} + \tilde{y}\hat{y} + \tilde{z}\hat{z}, \tag{2.8}$$

where $\tilde{x}, \tilde{y}, \tilde{z}$ denote the dimensional position components in each unit vector corresponding to the rotating frame. They are related to the components in the inertial frame as follows,

$$\begin{bmatrix} \tilde{x} \\ \tilde{y} \\ \tilde{z} \end{bmatrix} = \begin{bmatrix} \cos(\theta) & \sin(\theta) & 0 \\ -\sin(\theta) & \cos(\theta) & 0 \\ 0 & 0 & 1 \end{bmatrix} \begin{bmatrix} \tilde{X} \\ \tilde{Y} \\ \tilde{Z} \end{bmatrix}. \tag{2.9}$$

Since $\hat{x}$ is defined as the direction from P_1 to P_2, position vectors $\bar{\tilde{R}}_1, \bar{\tilde{R}}_2$ are written in the rotating frame as $\bar{\tilde{r}}_1, \bar{\tilde{r}}_2$, i.e.,

$$\bar{\tilde{r}}_1 = -\tilde{r}_1\hat{x} \tag{2.10}$$

$$\bar{\tilde{r}}_2 = \tilde{r}_2\hat{x}, \tag{2.11}$$

where $\tilde{r}_1 = |\bar{\tilde{r}}_1| = |\bar{\tilde{R}}_1|$, $\tilde{r}_2 = |\bar{\tilde{r}}_2| = |\bar{\tilde{R}}_2|$. Note that the magnitudes of the position vectors, or the distances, do not depend on the frames and are computed in the inertial or rotating frames. Then the relative position vectors $\bar{\tilde{r}}_{13}, \bar{\tilde{r}}_{23}$ are represented as,

$$\bar{\tilde{r}}_{13} = \bar{\tilde{r}}_3 - \bar{\tilde{r}}_1 = (\tilde{x} + \tilde{r}_1)\hat{x} + \tilde{y}\hat{y} + \tilde{z}\hat{z} \tag{2.12}$$

$$\bar{\tilde{r}}_{23} = \bar{\tilde{r}}_3 - \bar{\tilde{r}}_2 = (\tilde{x} - \tilde{r}_2)\hat{x} + \tilde{y}\hat{y} + \tilde{z}\hat{z}. \tag{2.13}$$

The equations of motion are rearranged by nondimensionalization for convenience. First, the characteristic length $\tilde{l}_*$ is defined as the constant distance between the primaries,

$$\tilde{l}_* = \tilde{r}_1 + \tilde{r}_2. \tag{2.14}$$

All quantities that represent distances are nondimensioalized via division by $\tilde{l}_*$. For example, for the position vector $\bar{\tilde{r}}_3$,

$$\bar{r}_3 = \frac{\bar{\tilde{r}}_3}{l^*} = x\hat{x} + y\hat{y} + z\hat{z}, \tag{2.15}$$

where $\bar{r}$ without the tilde accent denotes a nondimensional quantity, and $x = \tilde{x}/\tilde{l}_*, y = \tilde{y}/\tilde{l}_*, z = \tilde{z}/\tilde{l}_*$. The characteristic mass $\tilde{m}_*$ is defined as the sum of the masses of P_1 and P_2,

$$\tilde{m}_* = \tilde{m}_1 + \tilde{m}_2, \tag{2.16}$$

and μ is defined as the ratio of the mass of P_2 to the characteristic mass,

$$\mu = \frac{\tilde{m}_2}{\tilde{m}_*} \tag{2.17}$$

$$1 - \mu = \frac{\tilde{m}_1}{\tilde{m}_*}. \tag{2.18}$$

Since P_1 and P_2 form an isolated system by the assumption, and the origin is at the barycenter, the center of mass of the system should be a zero vector, i.e.,

$$\frac{\tilde{m}_1\bar{\tilde{r}}_1 + \tilde{m}_2\bar{\tilde{r}}_2}{\tilde{m}_1 + \tilde{m}_2} = \frac{-\tilde{m}_1\tilde{r}_1 + \tilde{m}_2\tilde{r}_2}{\tilde{m}_*}\hat{x} = (-\mu\tilde{r}_1 + (1-\mu)\tilde{r}_2)\hat{x} = 0\hat{x}. \tag{2.19}$$

By nondimensionalizing distances with $\tilde{l}_*$,

$$r_1 = \frac{\tilde{r}_1}{\tilde{l}_*} = \mu \tag{2.20}$$

$$r_2 = \frac{\tilde{r}_2}{\tilde{l}_*} = 1 - \mu, \tag{2.21}$$

implying that the nondimensional distances of the primaries from the barycenter are represented only with the mass ratio μ. Next, the characteristic time t^* is defined as,

$$\tilde{t}_* = \sqrt{\frac{(\tilde{l}_*)^3}{\tilde{G}\tilde{m}_*}}, \tag{2.22}$$

and the nondimensional time is denoted $t = \frac{\tilde{t}}{\tilde{t}_*}$. With the definitions of $\tilde{l}_*$, $\tilde{m}_*$, and $\tilde{t}_*$, Equation (2.3) is nondimensionalized as,

$$\frac{{}^I d^2\bar{r}_3}{dt^2} = -\frac{1-\mu}{r_{13}^3}\bar{r}_{13} - \frac{\mu}{r_{23}^3}\bar{r}_{23}, \tag{2.23}$$

where $\bar{r}_{13} = (x+\mu)\hat{x} + y\hat{y} + z\hat{z}$ and $\bar{r}_{23} = (x-1+\mu)\hat{x} + y\hat{y} + z\hat{z}$. Although all the vector quantities in Equation (2.23) are represented in the rotating frame, the second derivative

term on the left is still differentiated in the inertial frame; it must be computed in the rotating frame for consistency. The rotating velocity, or the first derivative, is represented as,

$$\frac{^R d\bar{r}_3}{d\tau} = \dot{x}\hat{x} + \dot{y}\hat{y} + \dot{z}\hat{z}, \tag{2.24}$$

where the dot indicates the differentiation with respect to the nondimensional time, t. For instance, $\dot{x} = \frac{dx}{dt}$. The rotating velocity is related to the inertial velocity by,

$$\frac{^I d\bar{r}_3}{dt} = \frac{^R d\bar{r}_3}{dt} + {}^I\bar{\omega}^R \times \bar{r}_3, \tag{2.25}$$

where the nondimensional angular velocity vector ${}^I\bar{\omega}^R$ is,

$${}^I\bar{\omega}^R = n\hat{z}, \tag{2.26}$$

where n is the nondimensional mean motion represented as,

$$n = \sqrt{\frac{\tilde{G}\tilde{m}_*}{(\tilde{l}_*)^3}} \cdot \tilde{t}_* = 1. \tag{2.27}$$

The physical meaning of n being 1 is that it requires $2\boldsymbol{\pi}$ nondimensional time units for P_1 and P_2 to complete one revolution around the barycenter. Next, the inertial acceleration is related to the rotating acceleration by,

$$\frac{^I d^2\bar{r}_3}{dt^2} = \frac{^R d^2\bar{r}_3}{dt^2} + ({}^I\bar{\omega}^R \times \frac{^R d\bar{r}_3}{dt}) + {}^I\bar{\omega}^R \times (\frac{^R d\bar{r}_3}{dt} + {}^I\bar{\omega}^R \times \bar{r}_3) \tag{2.28}$$

$$= (\ddot{x} - 2\dot{y} - x)\hat{x} + (\ddot{y} + 2\dot{x} - y)\hat{y} + \ddot{z}\hat{z}, \tag{2.29}$$

where the double dot accent indicates the second derivative with respect to the nondimensional time. For instance, $\ddot{x} = \frac{d^2x}{dt^2}$. Equations (2.23) and (2.29) are combined and expressed separately for each component as,

$$\ddot{x} - 2\dot{y} - x = -\frac{(1-\mu)(x+\mu)}{r_{13}^3} - \frac{\mu(x-1+\mu)}{r_{23}^3} \tag{2.30}$$

$$\ddot{y} + 2\dot{x} - y = -\frac{(1-\mu)y}{r_{13}^3} - \frac{\mu y}{r_{23}^3} \tag{2.31}$$

$$\ddot{z} = -\frac{(1-\mu)z}{r_{13}^3} - \frac{\mu z}{r_{23}^3}. \tag{2.32}$$

For a pseudo-potential function U^* defined as,

$$U^* = \frac{1-\mu}{r_{13}} + \frac{\mu}{r_{23}} + \frac{x^2+y^2}{2}, \tag{2.33}$$

the Equations (2.30)-(2.32) are rewritten using U^* as,

$$\ddot{x} - 2\dot{y} = \frac{\partial U^*}{\partial x} \tag{2.34}$$

$$\ddot{y} + 2\dot{x} = \frac{\partial U^*}{\partial y} \tag{2.35}$$

$$\ddot{z} = \frac{\partial U^*}{\partial z}. \tag{2.36}$$

This new form of the equations of motion, written in the rotating frame, allows an integral of motion to emerge. First perform a dot product between Equations (2.34)-(2.36) and the rotational velocity vector, $\frac{^R d\bar{r}}{dt}$, to obtain,

$$\ddot{x}\dot{x} - 2\dot{y}\dot{x} = \frac{\partial U^*}{\partial x}\dot{x} \tag{2.37}$$

$$\ddot{y}\dot{y} + 2\dot{x}\dot{y} = \frac{\partial U^*}{\partial y}\dot{y} \tag{2.38}$$

$$\ddot{z}\dot{z} = \frac{\partial U^*}{\partial z}\dot{z}, \tag{2.39}$$

and adding three equations, a single equation emerges,

$$\ddot{x}\dot{x} + \ddot{y}\dot{y} + \ddot{z}\dot{z} = \frac{\partial U^*}{\partial x}\dot{x} + \frac{\partial U^*}{\partial y}\dot{y} + \frac{\partial U^*}{\partial z}\dot{z}. \tag{2.40}$$

Since U^* is not an explicit function of time, the right side of Equation (2.40) is equivalent to $\dot{U}^*$. Then, both sides of the equation are integrated with respect to the nondimensional time t, to yield,

$$\frac{1}{2}(\dot{x}^2 + \dot{y}^2 + \dot{z}^2) = U^* - \frac{JC}{2}, \tag{2.41}$$

where the integration constant JC denotes the Jacobi constant. Solving for JC results in,

$$JC = 2U^* - (\dot{x}^2 + \dot{y}^2 + \dot{z}^2). \tag{2.42}$$

The Jacobi constant is one of several benefits from rearranging Equation (2.3) into the rotating frame. Although the number of the integration constants is drastically reduced from six to one by incorporating another celestial body, the Jacobi constant still offers great insight that is helpful for designing trajectories.

2.1.4 Higher-Fidelity Ephemeris Model

While the 2BP and the CR3BP do offer insights that are necessary for the initial mission design, the results must be validated in a higher-fidelity model. In this investigation, this model is denoted the higher-fidelity ephemeris model or simply the ephemeris model. In contrast to the lower-fidelity models, the ephemeris model incorporates any number of celestial bodies. Also, it utilizes ephemerides for the celestial bodies to deliver the true positions and velocities of the celestial bodies. Consequently, the numerical simulations are only required for the motion of the spacecraft. The SPICE toolkit, *DE421.bsp*, and *mar097.bsp* from the Jet Propulsion Laboratory's Navigation and Ancillary Information Facility [50] are utilized to access ephemerides of the Sun, planets and the moons. To derive the equations of motion for the ephemeris model, consider two separate vector differential equations from

the $\mathcal{N}$-Body problem. The first equation is written for the spacecraft, s/c, and the other one is written for a user selected reference body, or i,

$$\frac{{}^{I}d^2\bar{\tilde{R}}_{s/c}}{d\tilde{t}^2} = -\tilde{G}\sum_{\mathrm{j}=1,\ \mathrm{j}\neq s/c}^{\mathcal{N}} \frac{\tilde{m}_{\mathrm{j}}}{\tilde{R}^3_{\mathrm{j}s/c}}\bar{\tilde{R}}_{\mathrm{j}s/c} \tag{2.43}$$

$$\frac{{}^{I}d^2\bar{\tilde{R}}_{\mathrm{i}}}{d\tilde{t}^2} = -\tilde{G}\sum_{\mathrm{j}=1,\ \mathrm{j}\neq \mathrm{i}}^{\mathcal{N}} \frac{\tilde{m}_{\mathrm{j}}}{\tilde{R}^3_{\mathrm{ji}}}\bar{\tilde{R}}_{\mathrm{ji}}. \tag{2.44}$$

Then, the relative vector differential equation for the spacecraft with respect to the reference body is derived by subtracting Equation (2.44) from Equation (2.43),

$$\frac{{}^{I}d^2\bar{\tilde{R}}_{\mathrm{i}s/c}}{d\tilde{t}^2} = -\tilde{G}\frac{\tilde{m}_{\mathrm{i}}+\tilde{m}_{s/c}}{\tilde{R}^3_{\mathrm{i}s/c}}\bar{\tilde{R}}_{\mathrm{i}s/c} + \tilde{G}\sum_{\mathrm{j}=1,\mathrm{j}\neq s/c,\mathrm{i}}^{\mathcal{N}} \tilde{m}_{\mathrm{j}}\left(\frac{\bar{\tilde{R}}_{\mathrm{ji}}}{\tilde{R}^3_{\mathrm{ji}}} - \frac{\bar{\tilde{R}}_{\mathrm{j}s/c}}{\tilde{R}^3_{\mathrm{j}s/c}}\right). \tag{2.45}$$

The relative position vector of interest, $\bar{\tilde{R}}_{\mathrm{i}s/c}$, is obtained by integrating Equation (2.45) and the rest of the relative position vectors containing $\bar{R}_{\mathrm{ji}}, \bar{R}_{\mathrm{j}s/c}$ are retrieved from the ephemerides. Note that mathematically, the choice of central body should not change the true location of the spacecraft, or,

$$\bar{\tilde{R}}_{\mathrm{i}s/c} = \bar{\tilde{R}}_{\mathrm{ij}} + \bar{\tilde{R}}_{\mathrm{j}s/c}, \tag{2.46}$$

must hold for any pair of i and j bodies during the numerical propagation. However, Equation (2.46) is not perfectly satisfied due to the numerical integration errors that depend on the user-selected central body. Thus, it is required to employ a central body that results in an accurate and fast computation. The common practice is to select the celestial body that is closest to the location of the spacecraft. The dimensional quantities that appear in Equation (2.45) are nondimensionalized for consistent scaling and better numerical results. The distance, time, and mass quantities are divided by the CR3BP characteristic quantities $\tilde{l}_*$, $\tilde{t}_*$, and $\tilde{m}_*$ respectively, where two bodies with the most significant gravity forces are selected to form the CR3BP characteristic quantities. For example, when the spacecraft is near the Earth and begins its path to heliocentric space, the Sun-Earth CR3BP characteristic quantities are utilized to nondimensionalize Equation (2.45).

2.2 Coordinate Frames

The gravitational force models employ different coordinate frames. After listing all the frames that are utilized in the current analysis, the transformation formulas between the rotating and inertial frames are provided:

1. CR3BP inertial frame, represented as $\hat{X} - \hat{Y} - \hat{Z}$ in Figure 2.2

2. CR3BP rotating frame, represented as $\hat{x} - \hat{y} - \hat{z}$ in Figure 2.2

3. J2000 Earth equator inertial frame ("J2000"): the first unit vector of this frame points toward the equinox, which is either of the two positions on the sphere around the Earth, at which the ecliptic plane intersects the Earth's equatorial plane. By convention, the equinox associated with the Sun's ascending node is selected and simply denoted "the equinox." Next, the third unit vector is defined to be aligned with the Earth's rotational axis. The second unit vector is determined by the cross product between the third and the first unit vectors, in that order. The unit vectors are represented as,

$$\hat{X}_J - \hat{Y}_J - \hat{Z}_J. \tag{2.47}$$

   Since the equinox direction, as well as the out-of-plane direction, of the equatorial plane change over time, it is necessary to associate a reference epoch from which these vectors are computed. Noon on January 1, 2000, or J2000, is commonly used as the reference epoch. The detailed definitions of the directions of the unit vectors are found in the work by Standish [51].

4. J2000 Earth ecliptic inertial frame ("ECLIPJ2000"): the unit vectors for this frame are represented as,

$$\hat{X}_{EJ} - \hat{Y}_{EJ} - \hat{Z}_{EJ}, \tag{2.48}$$

   where the subscripts EJ refers to the ecliptic J2000. These unit vectors are obtained via rotating the J2000 unit vectors with respect to the equinox direction, $\hat{X}_{EJ} = \hat{X}_J$,

by the axial tilt (obliquitiy) of the Earth computed at J2000. The definition of the obliquity utilized in the SPICE toolkit is listed in the work by Seidelmann [52].

5. J2000 Mars equatorial inertial frame ("MARSIAU"): the first unit vector is defined as the direction from the center of Mars to the ascending node of the equatorial plane of Mars with respect to the Earth's equatorial plane, defined at J2000. The third unit vector is the rotational axis of Mars, and the second unit vector completes the dextral triad [53]. The unit vectors are represented as,

$$\hat{X}_M - \hat{Y}_M - \hat{Z}_M, \tag{2.49}$$

where the subcripts M refers to the fact that it is the MARSIAU frame.

Note that different origins are coupled with the listed sets of unit vectors to form different frames. For the current investigation, the origin is labelled ahead of the unit vectors to denote the coordinate frame. For the CR3BP frames, the barycenter is considered the default origin and is not mentioned. For example, the following expressions appear throughout the current work: Earth-Moon CR3BP rotating frame (the origin is at the barycenter of Earth-Moon), Earth-centered CR3BP inertial frame and Mars-centered MARSIAU frame.

2.2.1 Transformation between CR3BP Frames

Recall that the CR3BP has two associated frames, the inertial frame and the rotating frame. These frames are both based on the simplifying assumptions associated with the CR3BP, and the "inertial" frame constructed with the assumptions is not fixed in the true inertial frames such as J2000 frame or ECLIPJ2000 frame.

The transformation between these two frames is obtained. First, for simplicity, new symbols are introduced for the position and velocity vectors in the CR3BP frame,

$$\boldsymbol{r} = \bar{r}_3 \tag{2.50}$$

$$\boldsymbol{v} = \frac{^R d\bar{r}_3}{dt} \tag{2.51}$$

$$\boldsymbol{R} = \bar{R}_3 \tag{2.52}$$

$$\boldsymbol{V} = \frac{^I d\bar{R}_3}{dt}, \tag{2.53}$$

where the first two vectors correspond to the rotating position and velocity vectors, and the last two vectors denote the inertial position and velocity vectors. Note that the origin of these vectors is the CR3BP barycenter. The transformation formula is produced via a direction cosine matrix that relates the position as well as velocity vectors in two frames, i.e.,

$$\begin{bmatrix} \boldsymbol{R} \\ \boldsymbol{V} \end{bmatrix} = DCM_{R2I} \begin{bmatrix} \boldsymbol{r} \\ \boldsymbol{v} \end{bmatrix}. \tag{2.54}$$

Indeed, DCM_{R2I} is a 6 by 6 matrix, and is more straightforward to partition into the submatrices that correspond to the position and velocity. For the transformation of the position vector, recall Equation (2.9),

$$\boldsymbol{R} = C_{R2I}\boldsymbol{r}, \tag{2.55}$$

where the 3 by 3 matrix C_{R2I} is computed as,

$$C_{R2I} = \begin{bmatrix} \cos(\theta) & -\sin(\theta) & 0 \\ \sin(\theta) & \cos(\theta) & 0 \\ 0 & 0 & 1 \end{bmatrix}, \tag{2.56}$$

where θ is illustrated in Figure 2.2. Note that this angle is computed with the nondimensional time as well,

$$\theta = t + t_0, \tag{2.57}$$

where t_0 corresponds to the initial angle between the two frames, and t corresponds to the nondimensional time passed from t_0. For the relationship between velocity vector, the same matrix is used to convert the inertial velocity vector represented in both frames by,

$$\boldsymbol{V} = C_{R2I} \frac{{}^{I}d\bar{r}}{dt}, \tag{2.58}$$

where the inertial velocity vector represented in the rotating frame is computed with Equation (2.25), i.e.,

$$\frac{{}^{I}d\bar{r}}{dt} = \boldsymbol{v} + \hat{z} \times \boldsymbol{r}. \tag{2.59}$$

Then, Equation (2.58) is rewritten as,

$$\boldsymbol{V} = \begin{bmatrix} \dot{C}_{R2I} & C_{R2I} \end{bmatrix} \begin{bmatrix} \boldsymbol{r} \\ \boldsymbol{v} \end{bmatrix}, \tag{2.60}$$

where the 3 by 3 matrix $\dot{C}_{R2I}$ is,

$$\dot{C}_{R2I} = \frac{d}{dt} C_{R2I} = \begin{bmatrix} -\sin(t+t_0) & -\cos(t+t_0) & 0 \\ \cos(t+t_0) & \sin(t+t_0) & 0 \\ 0 & 0 & 1 \end{bmatrix}. \tag{2.61}$$

Finally, the direction cosine matrix that converts the rotating state to the inertial state is,

$$DCM_{R2I} = \begin{bmatrix} C_{R2I} & 0_{3\times3} \\ \dot{C}_{R2I} & C_{R2I} \end{bmatrix}. \tag{2.62}$$

Note that the same direction cosine matrix is utilized for transformation between CR3BP frames regardless of the origin. For instance, consider the vectors defined with the first primary as the origin, i.e.,

$$\boldsymbol{r}_{P1} = \boldsymbol{r} - \bar{r}_1 \tag{2.63}$$

$$\boldsymbol{v}_{P1} = \boldsymbol{v} - \frac{^R d\bar{r}_1}{dt} \tag{2.64}$$

$$\boldsymbol{R}_{P1} = \boldsymbol{R} - \bar{R}_1 \tag{2.65}$$

$$\boldsymbol{V}_{P1} = \boldsymbol{V} - \frac{^I d\bar{R}_1}{dt}, \tag{2.66}$$

where $\bar{r}_1$ is a constant vector, i.e.,

$$\bar{r}_1 = \mu\hat{x}, \tag{2.67}$$

$$\tag{2.68}$$

and consequently, $\frac{^R d\bar{r}_1}{dt}$ is a zero vector. The inertial position and velocity vectors with respect to the first primary are obtained with the same DCM_{R2I}, i.e.,

$$\begin{bmatrix} \boldsymbol{R}_{P1} \\ \boldsymbol{V}_{P1} \end{bmatrix} = DCM_{R2I} \begin{bmatrix} \boldsymbol{r}_{P1} \\ \boldsymbol{v}_{P1} \end{bmatrix}. \tag{2.69}$$

Also note that the reverse transformation is readily available with the inverse of the direction cosine matrix, i.e.,

$$\begin{bmatrix} \boldsymbol{r}_{P1} \\ \boldsymbol{v}_{P1} \end{bmatrix} = DCM_{R2I}^{-1} \begin{bmatrix} \boldsymbol{R}_{P1} \\ \boldsymbol{V}_{P1} \end{bmatrix}. \tag{2.70}$$

Equations (2.69) and (2.70) summarize the mathematical relationship between CR3BP rotating and inertial frames utilizing the first primary as the origin. Similar process is repeated for the vectors with the second primary as the origin as well.

2.2.2 Transformation between CR3BP Rotating Frame and Ephemeris Inertial Frames

The ephemeris inertial frames refer to the frames based on the ephemerides, i.e., J2000, ECLIPJ2000, and MARSIAU. The following explanation assumes J2000 as the ephemeris inertial frame, but it is be applied to other ephemeris inertial frames as well. First, $\boldsymbol{R}_J$, $\boldsymbol{V}_J$ are introduced to denote the nondimensional inertial position and velocity vectors in the J2000 frame, respectively. The origin is at the barycenter of the two primaries that constitute the CR3BP. The position and velocity vectors in the two frames, J2000 and CR3BP rotating frame, are related via the following matrix equation,

$$\begin{bmatrix} \boldsymbol{R}_J \\ \boldsymbol{V}_J \end{bmatrix} = DCM_{R2J} \begin{bmatrix} \boldsymbol{r} \\ \boldsymbol{v} \end{bmatrix}. \tag{2.71}$$

The goal is to compute the direction cosine matrix, DCM_{R2J}.

The CR3BP assumes that the two primaries are in planar, circular motion around the barycenter, not true in the actual ephemerides. Thus, the CR3BP rotating frame unit vectorsare no longer obtained as a rotation around the out-of-plane direction, since this direction is not constant. Instead, an instantaneous rotating frame is constructed based on the data retrieved from the ephemerides. First, retrieve the inertial position and velocity of the second primary with respect to the first primary, denoted by $\bar{\bar{R}}_{12}$ and $\bar{\bar{V}}_{12}$, respectively. Then, the instantaneous rotating frame unit vectors are computed as,

$$\hat{x}_{ins} = \frac{\bar{\bar{R}}_{12}}{\bar{\bar{R}}_{12}} \tag{2.72}$$

$$\bar{H}_{ins} = \frac{\bar{\bar{R}}_{12} \times \bar{\bar{V}}_{12}}{|\bar{\bar{R}}_{12} \times \bar{\bar{V}}_{12}|} \tag{2.73}$$

$$\hat{z}_{ins} = \frac{\bar{H}}{|\bar{H}|} \tag{2.74}$$

$$\hat{y}_{ins} = \frac{\hat{z}_{ins} \times \hat{x}_{ins}}{|\hat{z}_{ins} \times \hat{x}_{ins}|}, \tag{2.75}$$

where $\bar{H}_{ins}$ is the instantaneous angular momentum vector based on the ephemerides. Additionally, a pair of instantaneous characteristic quantities are defined,

$$\tilde{l}_{*,ins} = |\bar{\tilde{R}}_{12}| \tag{2.76}$$

$$\tilde{t}_{*,ins} = \sqrt{\frac{\tilde{l}^3_{*,ins}}{\tilde{G}(\tilde{m}_1 + \tilde{m}_2)}}. \tag{2.77}$$

Then, the relationship between the position vectors in the CR3BP rotating frame and J2000 inertial frame is established as,

$$\boldsymbol{R}_J = \frac{\tilde{l}_{*,ins}}{\tilde{l}_*} C_{R2J} \boldsymbol{r}, \tag{2.78}$$

where the 3 by 3 matrix C_{R2J} is,

$$C_{R2J} = \begin{bmatrix} \hat{x}_{ins} & \hat{y}_{ins} & \hat{z}_{ins} \end{bmatrix}. \tag{2.79}$$

The physical meaning of Equation (2.78) is that the position vector in the CR3BP rotating frame is rotated into the J2000 frame with an instantaneous direction cosine matrix constructed from the ephemerides. The position vector in the CR3BP rotating frame is first dimensionalized by multiplying via the instantaneous characteristic length, $\tilde{l}_{*,ins}$, and nondimensionalized again using the CR3BP characterstic length, $\tilde{l}_*$ [54].

Next, the inertial velocity vector is obtained via differentiation of Equation (2.78) with respect to the dimensional time, $\tilde{t}$. This process results the following equation,

$$\frac{{}^I d\boldsymbol{R}_J}{d\tilde{t}} = \frac{1}{\tilde{l}_*} \left(\frac{d\tilde{l}_{*,ins}}{d\tilde{t}} C_{R2J} \boldsymbol{r} + \tilde{l}_{*,ins} \frac{dC_{R2J}}{d\tilde{t}} \boldsymbol{r} + \tilde{l}_{*,ins} C_{R2J} \frac{{}^R d\boldsymbol{r}}{dt} \right) \tag{2.80}$$

$$= \frac{1}{\tilde{l}_*} \left(\tilde{V}_r C_{R2J} \boldsymbol{r} + \tilde{l}_{*,ins} \frac{dC_{R2J}}{d\tilde{t}} \boldsymbol{r} + \tilde{l}_{*,ins} C_{R2J} \frac{1}{\tilde{t}_{*,ins}} \boldsymbol{v} \right), \tag{2.81}$$

where $\tilde{V}_r = \frac{d\tilde{l}_{*,ins}}{d\tilde{t}}$ is the dimensional, instantaneous radial velocity of the second primary with respect to the first primary, and is computed with the ephemerides as,

$$V_r = \frac{\bar{\tilde{R}}_{12} \cdot \bar{\tilde{V}}_{12}}{|\tilde{R}_{12}|}. \tag{2.82}$$

And the second term of Equation (2.81) is computed with,

$$\frac{dC_{R2J}}{d\tilde{t}} = {}^{I}\bar{\tilde{\omega}}^{R}_{ins} \times C_{R2J}, \tag{2.83}$$

where ${}^{I}\bar{\tilde{\omega}}^{R}_{ins}$ is the instantaneous, dimensional angular velocity computed as,

$${}^{I}\bar{\tilde{\omega}}^{R}_{ins} = \frac{\bar{H}_{ins}}{\tilde{R}_{12}}. \tag{2.84}$$

Finally, Equation (2.80) is multiplied by $\tilde{t}_*$ for nondimensionalization, i.e.,

$$\boldsymbol{V}_J = \frac{{}^{I}d\boldsymbol{R}_J}{dt} = \frac{\tilde{t}_*}{\tilde{l}_*}\left(\tilde{V}_r C_{R2J}\boldsymbol{r} + \tilde{l}_{*,ins}({}^{I}\bar{\tilde{\omega}}^{R}_{ins} \times C_{R2J})\boldsymbol{r} + \frac{\tilde{l}_{*,ins}}{\tilde{t}_{*,ins}} C_{R2J}\boldsymbol{v}\right), \tag{2.85}$$

and all combined, the direction cosine matrix DCM_{R2J} is computed as,

$$DCM_{R2J} = \begin{bmatrix} \frac{\tilde{l}_{*,ins}}{\tilde{l}_*} C_{R2J} & 0_{3\times 3} \\ \frac{\tilde{t}_*}{\tilde{l}_*}\left(\tilde{V}_r C_{R2J} + \tilde{l}_{*,ins}({}^{I}\bar{\tilde{\omega}}^{R}_{ins} \times C_{R2J}) \right) & \frac{\tilde{l}_{*,ins}\cdot\tilde{t}_*}{\tilde{l}_*\cdot\tilde{t}_{*,ins}} C_{R2J} \end{bmatrix}. \tag{2.86}$$

The most noticeable difference between Equation (2.62) and Equation (2.86) is the additional term that depends on V_r, or the rate of change of the distance between the primaries in the ephemerides. This term accommodates the "pulsating" distances between the primaries. Also note that the C_{R2J} matrix is constructed instantaneously based on the data retrieved from the ephemerides.

2.3 Low-Thrust Engine Model

The gravitational models described thus far govern the ballistic motion of the spacecraft. To achieve a desirable change in the trajectory and to navigate through space, the spacecraft

is equipped with propulsion capabilities that deliver thrust. In the current investigation, the thrust is assumed to be generated by a low-thrust engine. The acceleration imparted on the spacecraft by a low-thrust engine is a function of a number of variables: spacecraft mass $\tilde{m}$, thrust vector $\bar{\tilde{T}}$, the available power $\tilde{\mathcal{P}}$, and specific impulse $\tilde{I_{sp}}$. The tilde accent indicates that these are dimensional quantities. Consistent with the gravitational forces, it is important to introduce simplifying but reasonable assumptions that facilitate analysis.

Generally, the power governs the maximum performance of the low-thrust engine. Thus, the maximum thrust as well as the specific impulse are written as functions of the available power,

$$\tilde{T}_{max} = f_1(\tilde{\mathcal{P}}) \tag{2.87}$$

$$\tilde{I_{sp}} = f_2(\tilde{\mathcal{P}}), \tag{2.88}$$

where f_1, f_2 are monotonically increasing functions of which the specific forms depend heavily on the engine in use. In other words, the performance of the engine, measured as (1) maximum thrust magnitude, $\tilde{T}_{max}$, and (2) efficiency of the engine, $\tilde{I_{sp}}$, depend on the available power $\tilde{\mathcal{P}}$. In the current investigation, it is assumed that the available power is constant, and thus,

$$\tilde{T}_{max} = \text{constant} \tag{2.89}$$

$$\tilde{I_{sp}} = \text{constant}. \tag{2.90}$$

The acceleration from the low-thrust engine is described with the remaining variables that do not depend on the power, thus, it is excluded from the engine model. Next, given a $\tilde{T}_{max}$ value that is constant, it is assumed that the thrust magnitude is any value between 0 and $\tilde{T}_{max}$, i.e.,

$$0 \leq \tilde{T} \leq \tilde{T}_{max}, \tag{2.91}$$

where $\tilde{T}$ is the magnitude of the thrust, $|\bar{\tilde{T}}|$. The thrust vector is represented as,

$$\bar{\tilde{T}} = \tilde{T}\hat{u}_T, \tag{2.92}$$

where $\hat{u}_T$ is a three-dimensional unit vector defined as $\bar{\tilde{T}}/\tilde{T}$. It is assumed that there is no restriction on the thrusting direction vector $\hat{u}_T$, or the spacecraft can thrust in any required direction. Also note that the thrust vector is represented in any of the frames. For example, if the CR3BP rotating frame is employed, the thrust vector is expressed as,

$$\bar{\tilde{T}} = \tilde{T}_x\hat{x} + \tilde{T}_y\hat{y} + \tilde{T}_z\hat{z}, \tag{2.93}$$

where $\tilde{T}_x, \tilde{T}_y, \tilde{T}_z$ correspond to the thrust component in the unit vectors for the CR3BP rotating frame. The acceleration from the thrust, $\bar{\tilde{a}}_T$, follows as,

$$\bar{\tilde{a}}_T = \frac{\bar{\tilde{T}}}{\tilde{m}}, \tag{2.94}$$

where the mass of the spacecraft, $\tilde{m}$, is not constant. The rate of change of $\tilde{m}$ is given by,

$$\frac{d\tilde{m}}{d\tilde{t}} = \frac{\tilde{T}}{\tilde{I_{sp}} \cdot \tilde{g}_0}, \tag{2.95}$$

where $\tilde{g}_0 = 9.80665 \times 10^{-3} km/s^2$ is the standard gravitational acceleration at the Earth's surface.

Given the low-thrust engine acceleration model, Equations (2.94) and (2.95) are incorporated into the gravitational force models. Note that any of the previously defined model are available, but the low-thrust terms must be nondimensionalized in a consistent way. Consider the case where the low-thrust terms are coupled with the CR3BP gravitational force model. The mass of the spacecraft is nondimensionlized as,

$$m = \frac{\tilde{m}}{\tilde{m}_0}, \tag{2.96}$$

where $\tilde{m}_0$ corresponds to the initial mass of the spacecraft. The thrust and the specific impulse are nondimensionlized as,

$$T = \tilde{T} \cdot \frac{(\tilde{t}_*)^2}{\tilde{l}_* \cdot \tilde{m}_0} \tag{2.97}$$

$$I_{sp} = \frac{\tilde{I_{sp}}}{\tilde{t}_*} \tag{2.98}$$

$$\bar{T} = T_x\hat{x} + T_y\hat{y} + T_z\hat{z}, \tag{2.99}$$

where $\tilde{T}$ is in kilo-newtons. Finally, the rate of change of m with respect to the nondimensional time $t = \tilde{t}/\tilde{t}_*$ is,

$$\frac{dm}{dt} = \dot{m} = \frac{\tilde{T}}{\tilde{I_{sp}} \cdot \tilde{g_0}} \cdot \frac{\tilde{t}_*}{\tilde{m}_0} = \frac{T}{I_{sp} \cdot g_0}, \tag{2.100}$$

where $g_0 = \tilde{g_0} \cdot (\tilde{t}_*)^2/\tilde{l}_*$. The nondimensional acceleration from the low-thrust engine is computed as,

$$\frac{\bar{a}_T}{m} = \frac{\bar{T}}{m} = \frac{T_x}{m}\hat{x} + \frac{T_y}{m}\hat{y} + \frac{T_z}{m}\hat{z}. \tag{2.101}$$

Then, the dynamics of the spacecraft are completely described by following set of differential equations,

$$\ddot{x} - 2\dot{y} = \frac{\partial U^*}{\partial x} + \frac{T_x}{m} \tag{2.102}$$

$$\ddot{y} + 2\dot{x} = \frac{\partial U^*}{\partial y} + \frac{T_y}{m} \tag{2.103}$$

$$\ddot{z} = \frac{\partial U^*}{\partial z} + \frac{T_z}{m} \tag{2.104}$$

$$\dot{m} = \frac{T}{I_{sp} \cdot g_0}, \tag{2.105}$$

where the first three equations now possess the extra acceleration terms from the low-thrust engine, and the last equation corresponds to the rate of change for the spacecraft mass.

From Equation (2.102) through (2.105), it is evident that the dynamics depend greatly upon the thrust T, the mass of the spacecraft m, and the specific impulse I_{sp}. And recall that the maximum level of thrust is bounded by the engine specifications,

$$T \leq T_{max}. \tag{2.106}$$

Consequently, the maximum acceleration from the low-thrust engine is also bounded as,

$$a \leq a_{T,max}, \tag{2.107}$$

where $a_{T,max}$ is,

$$a_{T,max} = \frac{T_{max}}{m}. \tag{2.108}$$

In the dimensional units, it becomes,

$$\tilde{a}_{T,max} = \frac{\tilde{T}_{max}}{\tilde{m}}. \tag{2.109}$$

Note that, as $\tilde{m}$ decreases over time by consuming the propellant, $\tilde{a}_{T,max}$ increases. This maximum acceleration value is tied to the control authority, i.e., the level to which the spacecraft can maneuver itself under the gravitational forces and has a large influence on the trajectories. Thus, the values for the low-thrust engine characteristics are carefully selected for realistic analysis. The specifications of the spacecraft are selected to be consistent with the values that appear in Table 1.2. For different phases of the transfer, different values for the initial mass, $\tilde{m}_0$, are introduced. For example, the initial mass of the heliocentric leg trajectory, 340.9kg is greater than the initial mass of the transfer trajectory between the Martian moons, 229.3kg, as the spacecraft gradually consumes the propellant. For this investigation, the model for the low-thrust engine assumes a maximum thrust level $\tilde{T}_{max} = 90mN$, and a specific impulse such that $I_{sp} = 1733$s, listed in Table 1.2.

2.4 Selecting a Lower-Fidelity Gravitational Force Model

The two-body problem and the CR3BP are utilized as the lower-fidelity gravitational force models in this investigation. They incorporate the minimum number of bodies into the model such that the dynamics can be exploited. This intermediate step is beneficial, as generating a trajectory in a higher-fidelity without an intelligent initial guess is computationally demanding, or even impossible. However, the incorporated bodies in the lower-fidelty models must still capture the core aspects of the true dynamics. Otherwise, the solutions obtained in the lower-fidelity models will not lead to converged solutions in the higher-fidelity ephemeris models. Indeed, it is necessary to include the bodies that exert significant accelerations to the spacecraft.

As a spacecraft traverses through space, the bodies that have most impact on the spacecraft path change over time. For the currently investigated problem, the spacecraft travels from the Earth to Mars. The bodies with the most dominant influence on the spacecraft gradually change over time: the Earth at departure, and then the Sun in heliocentric space and, finally, Mars at arrival. To accommodate this great variance in the dominant body, a number of different lower-fidelity models are coupled across the phases. For the departure phase, the Sun-Earth CR3BP is used as the lower-fidelity model to capture the influence of both bodies. Then, in heliocentric space, the motion of the spacecraft is largely dependent on the Sun's gravity and thus the Sun-2BP is employed. The motion in the vicinity of Mars is decomposed into multiple phases. First, Sun-Mars CR3BP approximates the motion of spacecraft upon the arrival in the Martian system. Then, Mars-2BP, coupled with Mars-Deimos CR3BP and Mars-Phobos CR3BP, is employed to generate a trajectory that connects both Martian moons.

This choice of lower-fidelity models is justified on two levels: (1) Approximate modeling to survey and (2) an eventual validation in the higher-fidelity ephemeris model. Table 2.1 includes the parameters for the celestial bodies with the most impact on the spacecraft path from the Earth to Mars. The CR3BP characteristic quantities, $\tilde{l}_*$, and $\tilde{t}_*$, follow the work done by Cox [55], who took the average of the instantaneous characteristic quantities $\tilde{l}_{*,ins}$ retrieved from the ephemerides over 100 years to compute $\tilde{l}_*$ and $\tilde{t}_*$. For the approximate

modeling, it is assumed that all the celestial bodies are in a common plane with a circular motion around their respective parent body. Then, the gravitational accelerations from the bodies are compared with the low-thrust engine acceleration to determine the bodies to be considered, depending on the location of the spacecraft en route from the Earth to Mars. To that end, the threshold distance d from each body is defined as,

$$\frac{\tilde{G}\tilde{m}}{d^2} = \frac{\tilde{a}_{T,max}}{100} \tag{2.110}$$

$$d = \sqrt{\frac{100\tilde{G}\tilde{m}}{\tilde{a}_{T,max}}}, \tag{2.111}$$

or where the gravitational acceleration from the body is equivalent to the 1/100 of the maximum acceleration from the engine, based on the similar investigation completed by Cox [55] and Muralidharan [56]. If the spacecraft is closer to the body than d, it is assumed that the body must be incorporated into the lower-fidelity model. Otherwise, it may be neglected from the lower-fidelity model as a "perturbing body", of which the acceleration is easily counteracted by the thrust. The last column of Table 2.1 includes the threshold distance values in km for the listed celestial bodies when $\tilde{a}_{T,max} = 3.3333 \times 10^{-7} km/s^2$. The areas within the threshold distance for the bodies are plotted in Figure 2.3, where $\hat{X}$ and $\hat{Y}$ correspond to the arbitrary inertial unit vectors that span the orbital plane. Figure 2.3(a) illustrates the threshold distance for the Sun, where it extends beyond Jupiter's orbit implying that, if possible, it is desirable to include the Sun's gravity into the lower-fidelity model. Indeed, the Sun is incorporated into the lower-fidelity models in this investigation via the Sun-Planet CR3BPs or the Sun-2BP. The only exception is the transfer between the Martian moons, where the Mars-Martian moon CR3BPs or the Mars-2BP are employed. More background in the reasoning for ignoring the Sun's gravity is explored later in the detailed design of the moon tours. The threshold distances for Mars, the Earth and Mars are illustrated in Figure 2.3(b) as the shaded regions surrounding the circular orbits of the planets. For a transfer trajectory between the Earth and Mars, it is reasonable to disregard Venus's gravity unless a Venus flyby is employed. From this reasoning, Sun-Earth CR3BP and Sun-Mars CR3BP are employed at the departure from the Earth and arrival at Mars, respectively. Similarly, Figure 2.3(c) illustrates that Jupiter's gravity can be neglected for

the lower-fidelity models. Figure 2.3(d) displays a zoom-in view of the boxed area in Figure 2.3(b), where the Earth and Moon's orbits are depicted. The Moon orbits around the Earth, a body that that also orbits the Sun. As a result, the darker shade corresponds to the Moon's threshold distance while orbiting around the Earth. This figure implies that, in the Earth's vicinity, the Moon may also be incorporated into the lower-fidelity model. This investigation avoids this additional complexity by focusing on the departure from the location outside of the threshold distance of the Moon. Finally, Figure 2.3(e) depicts the Martian moons' threshold distance in the Mars-centered inertial frame. Note that the shades are too thin to be noticed, but it is still desirable to consider their gravitational forces within the threshold distances. Thus, Mars-Deimos CR3BP and Mars-Phobos CR3BP are employed as the lower-fidelity models in the vicinity of the moons.

After selecting a suitable lower-fidelity model through the approximate modeling and survey, the results are ultimately validated in a higher-fidelity model. After introducing more bodies into the model, and removing the simplifying assumptions of the lower-fidelity models, the results are reconverged in the higher-fidelity model. This process justifies approximation through the selected lower-fidelity models.

Table 2.1. Parameters of celestial bodies most relevant to the Earth to Mars trajectory

Bodies	$\tilde{G}\tilde{m}(km^3/s^2)$ [1]	Parent [2]	$\mu(n.d.)$ [3]	$\tilde{l}_*(km)$ [3]	$\tilde{t}_*(s)$ [3]	$d(km)$
Sun	1.3271×10^{11}	-	-	-	-	6.3098×10^{9}
Earth	3.9860×10^{5}	Sun	3.0035×10^{-6}	1.4960×10^{8}	5.0226×10^{6}	1.0935×10^{7}
Moon	4.9028×10^{3}	Earth	1.2151×10^{-2}	3.8475×10^{5}	3.7570×10^{5}	1.2128×10^{6}
Mars	4.2828×10^{4}	Sun	3.2272×10^{-7}	2.2794×10^{8}	9.4466×10^{6}	3.5845×10^{6}
Phobos	7.0976×10^{-5}	Mars	1.6549×10^{-8}	9.3737×10^{3}	4.3853×10^{3}	4.6111×10^{2}
Deimos	9.6156×10^{-6}	Mars	2.2451×10^{-9}	2.3457×10^{4}	1.7360×10^{4}	1.6984×10^{2}

[1] Gravitation parameter from the ephemerides file, *DE421.bsp*
[2] The body around which each body orbits around
[3] The quantities corresponding to the CR3BP constructed with the parent and each body

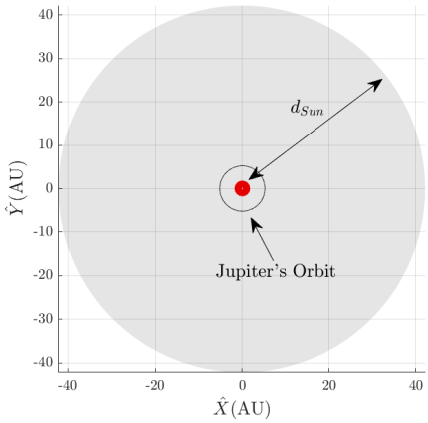

(a) Threshold distance of the Sun

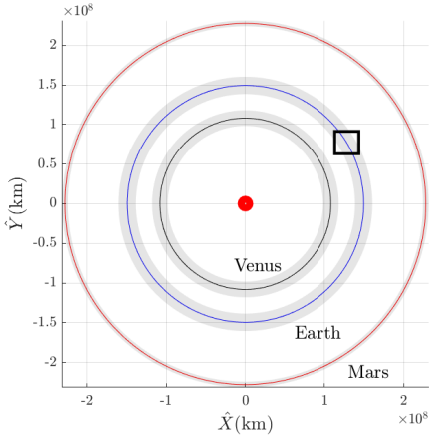

(b) Threshold distances of Mars, Earth and Venus

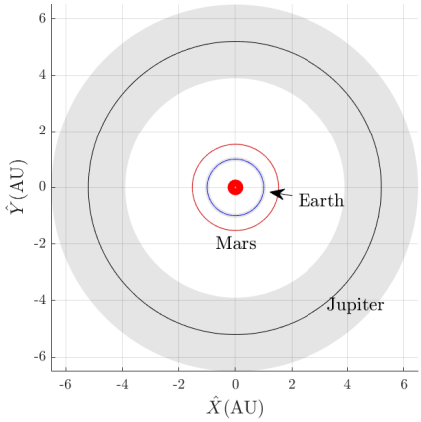

(c) Threshold distances of Jupiter, Mars, Earth

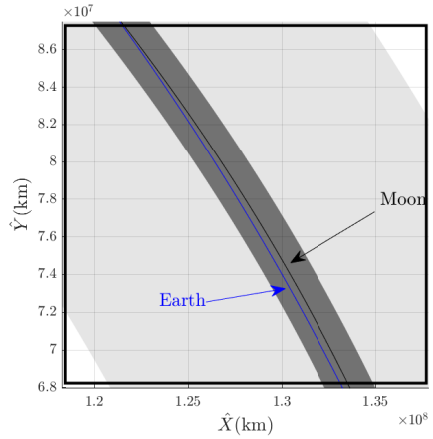

(d) Threshold distances of the Earth and the Moon

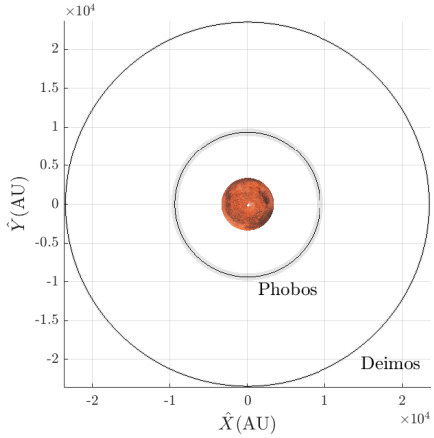

(e) Threshold distances of Phobos and Deimos

Figure 2.3. Visualization of the threshold distance d for the relevant celestial bodies when $\tilde{a}_{T,max} = 3.3333 \times 10^{-7} km/s^2$

3. LOW-THRUST TRAJECTORY COMPUTATION AND OPTIMIZATION VIA DIRECT COLLOCATION

Trajectory design is a process of producing a time history for the spacecraft state and control that satisfy a set constraints. The constraints include, but are not limited to, the dynamical constraints, i.e., the state history should satisfy the governing equations of motion, as well as the boundary constraints that specify the initial and final states of the spacecraft. While the trajectory design problem is already non-trivial, it is further complicated when a low-thrust engine model is employed. For a low-thrust trajectory, the governing equations of motion include the acceleration terms from the low-thrust engine force, increasing the dimension of the problem. Now, the time history for the low-thrust control variables, or the magnitude and direction of the low-thrust force must be obtained in addition to the history of the spacecraft states.

While multiple strategies are available to design low-thrust trajectories, one particular technique, i.e., *direct collocation*, is employed in this investigation. Direct collocation refers to an algorithm that combines collocation and direct optimization techniques. The implementation of direct collocation can be realized in various forms as detailed in previous investigations, including survey papers by Betts [57], Topputo and Zhang [58], and Conway [59]. The direct collocation algorithm utilized in this investigation is based on the one implemented and extensively explained by Ozimek [24] and Pritchett [60], and the collocation algorithm in this work is a summary of the work presented by Pritchett [60].

3.1 Collocation

The equations of motion describe the behavior of an object as it evolves within a dynamical system. As differential equations, if they cannot be integrated analytically, the equations of motion are propagated using a numerical integration scheme. For a spacecraft under the influence of both gravitational bodies and low-thrust engine force, no analytical solutions exist even with the simplest model, thus, a numerical method is required.

First, the general forms for the state vector and the corresponding equations of motion are defined. Consider a state vector of a system at a certain time, $t = t_n$, given as,

$$\boldsymbol{x} = \boldsymbol{x}(t = t_n), \tag{3.1}$$

where $\boldsymbol{x}$ denotes the state vector with dimensions $N \times 1$, i.e., the state consists of N components, and t denotes the scalar time. Then, the dynamics of the system are represented by a set of differential equations $\boldsymbol{f}$ that satisfy,

$$\frac{^I d\boldsymbol{x}}{dt} = \boldsymbol{f}(t, \boldsymbol{x}), \tag{3.2}$$

where $\frac{^I d\boldsymbol{x}}{dt}$ denotes the time derivative of the state vector. Note that it is assumed that $\boldsymbol{f}$ is a function only of the time and the state for simplicity, but can be generalized into other functions that have additional parameters as the input. Then, a numerical integration scheme is used to produce the state vector at a next time step, $\boldsymbol{x}(t_n + \Delta t)$, where Δt is the time step of the integration. Equation (3.2) fully defines the equations of motion that describe the behavior of an object within a dynamical system.

A numerical integration scheme is applied to Equation (3.2), where the scheme generally classified into explicit and implicit methods [61]. For an explicit method,

$$\boldsymbol{x}(t_n + \Delta t) = \boldsymbol{\mathcal{F}}(t, \boldsymbol{x}(t_n)), \tag{3.3}$$

where $\boldsymbol{\mathcal{F}}$ represents an explicit scheme that is obtained via numerically integrating the equations of motion, $\boldsymbol{f}$. Note that for an explicit method, the state at the next time step is a function only of the time t and the state at the current time, $\boldsymbol{x}(t_n)$, thus, Equation (3.3) is an explicit equation with respect to $\boldsymbol{x}(t_n + \Delta t)$. In contrast, for an implicit method, the state vector corresponding to the next time step is evaluated via,

$$\boldsymbol{\mathcal{G}}(t, \boldsymbol{x}(t_n), \boldsymbol{x}(t_n + \Delta t)) = 0, \tag{3.4}$$

where $\boldsymbol{\mathcal{G}}$ denotes an implicit scheme. As $\boldsymbol{\mathcal{G}}$ is a function of time and the states at both t_n and $t_n + \Delta t$, an iterative method is employed to search for $\boldsymbol{x}(t_n + \Delta t)$ that satisfies Equation (3.4) given the current state, $\boldsymbol{x}(t_n)$.

Collocation is one particular approach to implement the implicit integration method. To employ a collocation algorithm, the entire integration time interval, $[t_I, t_F]$, is divided into multiple segments along a set of boundary points Π,

$$\Pi : t_I = t_1 < t_2 < \cdots < t_s < t_{s+1} = t_F, \tag{3.5}$$

where Π is also denoted a *mesh*. A segment is comprised of two consecutive boundary points along a mesh, where the i-th segment is defined with the time interval $\mathcal{T}_\mathrm{i}$,

$$\mathcal{T}_\mathrm{i} = [t_\mathrm{i}, t_{\mathrm{i}+1}], \ (1 \leq \mathrm{i} \leq s), \tag{3.6}$$

where s segments result from $s + 1$ boundary points. Then, the time history of the state corresponding to an object within a system over each segment is approximated as a set of polynomial functions of time with degree n, $\boldsymbol{p}_\mathrm{i}(t)$, for the i-th segment over $\mathcal{T}_\mathrm{i}$. Note that $\boldsymbol{p}_\mathrm{i}(t)$ comprises N different polynomial functions of degree n, constructed for each of N components of the state vector $\boldsymbol{x}$. The coefficients of the polynomials can be different for each segment, so $\boldsymbol{p}_\mathrm{i}(t) \neq \boldsymbol{p}_k(t)$ for $\mathrm{i} \neq k$ in general. To force these polynomials to satisfy the equations of motion and to accurately describe the true time history of the state, the implicit equation (Equation (3.4), $\boldsymbol{\mathcal{G}}$) must be satisfied over all segments. Constructing $\boldsymbol{\mathcal{G}}$ for the i-th segment under a collocation algorithm starts by selecting n *collocation nodes*, or *collocation points*, $t_{\mathrm{i},1}, t_{\mathrm{i},2}, ...t_{\mathrm{i},n-1}, t_{\mathrm{i},n}$ that satisfy,

$$t_\mathrm{i} \leq t_{\mathrm{i},1} < t_{\mathrm{i},2} < ... < t_{\mathrm{i},n-1} < t_{\mathrm{i},n} \leq t_{\mathrm{i}+1} \tag{3.7}$$

Next, at each collocation node, the equations of motion are enforced to the polynomial by,

$$\frac{d\boldsymbol{p}_\mathrm{i}(t_{\mathrm{i,j}})}{dt} = \boldsymbol{f}(t_{\mathrm{i,j}}, \boldsymbol{p}(t_{\mathrm{i,j}})), \ (1 \leq \mathrm{j} \leq n), \tag{3.8}$$

where the left side of the equation represents the dynamics approximated by the polynomial $\boldsymbol{p}_{\mathrm{i}}(t)$, and the right side corresponds to the derivatives obtained by substituting $\boldsymbol{p}_{\mathrm{i}}(t)$ into the equations of motion, $\boldsymbol{f}$. The name *collocation* arises here, as the approximated and the actual dynamics are *collocated* at the collocation nodes. Equation (3.8) corresponds to the implicit equation $\boldsymbol{\mathcal{G}}$, and it is obtained for all existing segments over the mesh. Then an iterative scheme is employed to satisfy Equation (3.4), where the exact form of the equation varies depending on the specific scheme for the collocation algorithm that decides the degree n as well as the location of the collocation nodes.

3.1.1 Seventh Order Legendre-Gauss-Lobatto Scheme

While an arbitrarily high order of integration can be achieved by selecting a polynomial with a higher degree, the accuracy of the integration also depends on the location of the collocation nodes. The locations of the nodes that maximize the accuracy are known to be the roots of the Legendre polynomial, denoted as $P_n(t)$ for the n-th order polynomial, defined over the time interval $\mathcal{T}_{\mathrm{i}}$. This node placing scheme is called the Legendre-Gauss scheme, and the resulting accuracy of the integration is $2n$. While this level of accuracy bounds the theoretically highest accuracy achieved by using n-th degree polynomial approximation [61], it is typically associated with implementation challenges as the roots of $P_n(t)$ do not include the end points of the time interval, t_{i} and $t_{\mathrm{i}+1}$. To ease the implementation process, variants of Legendre-Gauss scheme were developed. In this investigation, the Legendre-Gauss-Lobatto (LGL) scheme with 7th order polynomials is considered and explained.

The n-th degree LGL scheme places $(n-2)$ nodes at the roots of $\dot{P}_{n-1}(t)$, where the dot accent indicates the derivative of the Legendre polynomial with respect to t, and two additional nodes are placed at the both end points. This node placement results in the $(2n-2)$-th order of accuracy. For example, the 7-th order LGL scheme is a 12-th order integration method. Consider a i-th segment along the mesh with $\mathcal{T}_{\mathrm{i}} = [t_{\mathrm{i}}, t_{\mathrm{i}+1}]$ as the boundary points. It is advantageous to nondimensionalize the time interval of each segment as,

$$\tau(t) = \frac{2}{t_{\mathrm{i}+1} - t_{\mathrm{i}}}(t - t_{\mathrm{i}}) - 1, \ (t_{\mathrm{i}} \leq t \leq t_{\mathrm{i}+1}) \tag{3.9}$$

where the nondimensional time τ is mapped from t over $\mathcal{T}_\mathrm{i}$ such that τ ranges between $[-1, 1]$. The derivative with respect to τ is computed as,

$$\frac{d}{d\tau} = \frac{d}{dt}\frac{t_{\mathrm{i}+1} - t_\mathrm{i}}{2}, \tag{3.10}$$

and the derivatives of the states with respect to this nondimensional time becomes,

$$\boldsymbol{x}' = \frac{d\boldsymbol{x}}{d\tau} = \frac{d\boldsymbol{x}}{dt}\frac{t_{\mathrm{i}+1} - t_\mathrm{i}}{2} = \boldsymbol{f}(t, \boldsymbol{x})\frac{t_{\mathrm{i}+1} - t_\mathrm{i}}{2}, \tag{3.11}$$

where the prime superscript indicates the differentiation with respect to τ. The introduction of τ helps the implementation of LGL scheme by enabling a consistent time scaling across all segments, and it also lets a separate formulation of the collocation algorithm apart from the length of the integration. Next, assuming a 7-th order LGL scheme, 7 collocation nodes are placed, denoted $\tau_1, \tau_2, ..., \tau_7$. The first and last nodes are placed at the end points, or, $\tau_1 = -1, \tau_7 = 1$. The 5 other nodes are placed at the roots of $\dot{P}_6(\tau)$, where the Legendre equation is constructed over $-1 \leq \tau \leq 1$. The locations of the nodes are fixed regardless of the length of the segment, and thus are computed a priori and stored. Recall that the implicit integration via collocation requires the 7-th order polynomial to satisfy Equation (3.8) at all the 7 collocation nodes. For a scheme with an odd-numbered order, this process is described as follows:

1. The states are freely selected for odd-numbered nodes, or τ_k, for $k = 1, 3, 5, 7$, as $\boldsymbol{x}_{\mathrm{i},k}$.

2. The derivatives of the states for odd-numbered nodes are computed from the equations of the motion as $\boldsymbol{x}'_{\mathrm{i},k}$,

$$\boldsymbol{x}'_{\mathrm{i},k} = \boldsymbol{f}(t_{\mathrm{i},k}, \boldsymbol{x}_{\mathrm{i},k})\frac{t_{\mathrm{i}+1} - t_\mathrm{i}}{2}. \tag{3.12}$$

3. The coefficients of a set of 7-th degree polynomials are constructed such that they satisfy $\boldsymbol{p}(\tau_k) = \boldsymbol{x}_{\mathrm{i},k},\ \boldsymbol{p}(\tau_k)' = \boldsymbol{x}'_{\mathrm{i},k}$, where $k = 1, 3, 5, 7$. Thus, the constructed polynomials automatically satisfy Equation (3.8) at the odd-numbered nodes.

4. At the even-numbered nodes, Equation (3.8) is enforced. As the states at the even-numbered nodes depend on the odd-numbered nodes, an iterative algorithm is utilized to find states of the odd-numbered nodes that satisfy Equation (3.8) at the even-numbered nodes.

Recall that when $\boldsymbol{x}$ is a N-dimensional vector, $\boldsymbol{p}_\mathrm{i}$ is also a set of N polynomials, i.e., polynomials are separately constructed for each component of $\boldsymbol{x}$. Then, the coefficients of the $\boldsymbol{p}_\mathrm{i}$ form a matrix and the above steps involve matrix algebra. Utilizing matrix representation, $\boldsymbol{p}_\mathrm{i}(\tau)$ is computed as,

$$\boldsymbol{p}_\mathrm{i}(\tau) = \boldsymbol{C}_\mathrm{i} \begin{bmatrix} 1 & \tau & \tau^2 & \cdots & \tau^7 \end{bmatrix}^T, \tag{3.13}$$

where $\boldsymbol{C}_\mathrm{i}$ is a matrix of the polynomial coefficients with dimensions $N \times 8$. The rows of $\boldsymbol{C}_\mathrm{i}$ correspond to different components of the state vector $\boldsymbol{x}$, and the columns of $\boldsymbol{C}_\mathrm{i}$ correspond to the coefficients of the τ terms with different orders. Each component of $\boldsymbol{C}_\mathrm{i}$ is determined in the way that $\boldsymbol{p}_\mathrm{i}(\tau)$ satisfies,

$$\boldsymbol{p}_\mathrm{i}(\tau_k) = \boldsymbol{x}_{\mathrm{i},k} \tag{3.14}$$

$$\boldsymbol{p}'_\mathrm{i}(\tau_k) = \boldsymbol{x}'_{\mathrm{i},k}, \tag{3.15}$$

for the odd-numbered nodes, $k = 1, 3, 5, 7$. Then, $\boldsymbol{p}'_\mathrm{i}(\tau)$ is written as,

$$\boldsymbol{p}'_\mathrm{i}(\tau) = \boldsymbol{C}_\mathrm{i} \begin{bmatrix} 0 & 1 & 2\tau & \cdots & 7\tau^6 \end{bmatrix}^T, \tag{3.16}$$

since $\boldsymbol{C}_\mathrm{i}$ does not depend on τ. Next, Equations (3.14) and (3.15) are rewritten by the matrix representation,

$$\begin{bmatrix} \boldsymbol{x}_{\mathrm{i},1} & \boldsymbol{x}_{\mathrm{i},3} & \boldsymbol{x}_{\mathrm{i},5} & \boldsymbol{x}_{\mathrm{i},7} & \dot{\boldsymbol{x}}_{\mathrm{i},1} & \dot{\boldsymbol{x}}_{\mathrm{i},3} & \dot{\boldsymbol{x}}_{\mathrm{i},5} & \dot{\boldsymbol{x}}_{\mathrm{i},7} \end{bmatrix} = \boldsymbol{C}_\mathrm{i} \begin{bmatrix} \boldsymbol{\tau} & \boldsymbol{\tau}' \end{bmatrix}, \tag{3.17}$$

where $\boldsymbol{\tau}$ and $\boldsymbol{\tau}'$ denote the matrices,

$$\boldsymbol{\tau} = \begin{bmatrix} 1 & 1 & 1 & 1 \\ \tau_1 & \tau_3 & \tau_5 & \tau_7 \\ \tau_1^2 & \tau_3^2 & \tau_5^2 & \tau_7^2 \\ \vdots & \vdots & \vdots & \vdots \\ \tau_1^7 & \tau_3^7 & \tau_5^7 & \tau_7^7 \end{bmatrix} \tag{3.18}$$

$$\boldsymbol{\tau}' = \begin{bmatrix} 0 & 0 & 0 & 0 \\ 1 & 1 & 1 & 1 \\ 2\tau_1 & 2\tau_3 & 2\tau_5 & 2\tau_7 \\ \vdots & \vdots & \vdots & \vdots \\ 7\tau_1^6 & 7\tau_3^6 & 7\tau_5^6 & 7\tau_7^6 \end{bmatrix}, \tag{3.19}$$

where the dimensions of the matrices are 8×4. Concatenating $\boldsymbol{\tau}$ and $\boldsymbol{\tau}'$, a single matrix of dimensions 8×8, $\boldsymbol{A}$ is obtained,

$$\boldsymbol{A} = \begin{bmatrix} \boldsymbol{\tau} & \boldsymbol{\tau}' \end{bmatrix}. \tag{3.20}$$

Note that $\boldsymbol{A}$ is a constant matrix across all segments, as its components only depend on $\tau_1, \tau_3, \tau_5, \tau_7$ that are fixed. The coefficient matrix $\boldsymbol{C}_\mathrm{i}$ is then computed as,

$$\boldsymbol{C}_\mathrm{i} = \boldsymbol{X}_\mathrm{i} \boldsymbol{A}^{-1}, \tag{3.21}$$

where $\boldsymbol{X}_\mathrm{i}$ is,

$$\boldsymbol{X}_\mathrm{i} = \begin{bmatrix} \boldsymbol{x}_{\mathrm{i},1} & \boldsymbol{x}_{\mathrm{i},3} & \boldsymbol{x}_{\mathrm{i},5} & \boldsymbol{x}_{\mathrm{i},7} & \dot{\boldsymbol{x}}_{\mathrm{i},1} & \dot{\boldsymbol{x}}_{\mathrm{i},3} & \dot{\boldsymbol{x}}_{\mathrm{i},5} & \dot{\boldsymbol{x}}_{\mathrm{i},7} \end{bmatrix}, \tag{3.22}$$

and depends on the choice of $\boldsymbol{x}_{\mathrm{i},1}, \boldsymbol{x}_{\mathrm{i},3}, \boldsymbol{x}_{\mathrm{i},5}, \boldsymbol{x}_{\mathrm{i},7}$. Next, Equation (3.8) is enforced at the even-numbered nodes, τ_2, τ_4, τ_6. To that end, two additional matrices, $\boldsymbol{B}$ and $\boldsymbol{D}$, are first constructed as,

$$\boldsymbol{B} = \begin{bmatrix} 1 & 1 & 1 \\ \tau_2 & \tau_4 & \tau_6 \\ \tau_2^2 & \tau_4^2 & \tau_6^2 \\ \vdots & \vdots & \vdots \\ \tau_2^7 & \tau_4^7 & \tau_6^7 \end{bmatrix} \tag{3.23}$$

$$\boldsymbol{D} = \begin{bmatrix} 0 & 0 & 0 \\ 1 & 1 & 1 \\ 2\tau_2 & 2\tau_4 & 2\tau_6 \\ \vdots & \vdots & \vdots \\ 7\tau_2^6 & 7\tau_4^6 & 7\tau_6^6 \end{bmatrix}, \tag{3.24}$$

where the dimensions of the matrices are 8×3, and the components are constant. The states at the even-numbered nodes are evaluated by the following matrix multiplication,

$$\begin{bmatrix} \boldsymbol{x}_{\mathrm{i},2} & \boldsymbol{x}_{\mathrm{i},4} & \boldsymbol{x}_{\mathrm{i},6} \end{bmatrix} = \boldsymbol{C}_{\mathrm{i}} \boldsymbol{B}, \tag{3.25}$$

where $\boldsymbol{x}_{\mathrm{i},2}, \boldsymbol{x}_{\mathrm{i},4}$, and $\boldsymbol{x}_{\mathrm{i},6}$ correspond to the states at the even-numbered nodes. Then, Equation (3.8) is identical to the following equation,

$$\boldsymbol{C}_{\mathrm{i}} \boldsymbol{D} = \begin{bmatrix} \boldsymbol{x}'_{\mathrm{i},2} & \boldsymbol{x}'_{\mathrm{i},4} & \boldsymbol{x}'_{\mathrm{i},6} \end{bmatrix}, \tag{3.26}$$

where the left side corresponds to the derivatives of the polynomials, $\boldsymbol{p}'_{\mathrm{i}}(\tau)$, at the even-numbered nodes, and the right side corresponds to the derivatives obtained with the equations of motion, $\boldsymbol{f}$, at these nodes. Note that whether the equation is satisfied depends on

the states at the odd-numbered nodes, $\boldsymbol{x}_{\mathrm{i},1}, \boldsymbol{x}_{\mathrm{i},3}, \boldsymbol{x}_{\mathrm{i},5}, \boldsymbol{x}_{\mathrm{i},7}$. The defect constraints are defined as the difference between the left and right sides of the Equation (3.26),

$$\Delta_{\mathrm{i}} = \boldsymbol{C}_{\mathrm{i}}\boldsymbol{D} - \begin{bmatrix} \dot{\boldsymbol{x}}_{\mathrm{i},2} & \dot{\boldsymbol{x}}_{\mathrm{i},4} & \dot{\boldsymbol{x}}_{\mathrm{i},6} \end{bmatrix}. \tag{3.27}$$

Under this formulation, the implicit integration is conducted by iteratively solving for a set of odd-numbered states, i.e., $\boldsymbol{x}_{\mathrm{i},1}, \boldsymbol{x}_{\mathrm{i},3}, \boldsymbol{x}_{\mathrm{i},5}$, and $\boldsymbol{x}_{\mathrm{i},7}$, that result in zero Δ_{i} for all segments, i.e., $1 \leq \mathrm{i} \leq s$.

3.1.2 Mesh Refinement

For explicit integration methods, the error of the integration is controlled below a user-defined tolerance by using a smaller time step, Δt in Equation (3.3). For implicit methods, the error control is conducted via a *mesh refinement* technique, where the locations of the boundary points are adjusted such that the error over each segment is below a set tolerance level. There exist multiple mesh refinement schemes as explained by [60], and a scheme termed Control with Explicit Propagation (CEP), proposed by Grebow and Pavlak [62], is employed here. This method utilizes the states resulting from an explicit integration method as the "true" values, from which the error of the collocation is computed.

The error control strategy consists of two different actions: (1) adding the segment and (2) removing the segment. First, the desired tolerance is denoted *tol*, and recall that the boundary points are $t_{\mathrm{i}}, t_{\mathrm{i}+1}$ for the i-th segment. Then given the initial state at t_{i} as $\boldsymbol{x}(t_{\mathrm{i}})$, the "true" state at $t_{\mathrm{i}+1}$ is computed with the explicit method,

$$\boldsymbol{x}(t_{\mathrm{i}+1}) = \boldsymbol{\mathcal{F}}(t, \boldsymbol{x}(t_{\mathrm{i}})), \tag{3.28}$$

by Equation (3.3). The state at $t_{\mathrm{i}+1}$ from the collocation algorithm, $\boldsymbol{x}_{col}(t_{\mathrm{i}+1})$, satisfies

$$\boldsymbol{\mathcal{G}}(t, \boldsymbol{x}(t_{\mathrm{i}}), \boldsymbol{x}_{col}(t_{\mathrm{i}+1})) = 0, \tag{3.29}$$

following Equation (3.4). The error of the collocation algorithm over the i-th segment is defined as,

$$\epsilon = |\boldsymbol{x}_{col}(t_{\mathrm{i}+1}) - \boldsymbol{x}(t_{\mathrm{i}+1})|, \tag{3.30}$$

where $|\boldsymbol{x}_{col}(t_{\mathrm{i}+1}) - \boldsymbol{x}(t_{\mathrm{i}+1})|$ is the L2 norm of the difference of states computed from the explicit method and the collocation algorithm. If the error ϵ is larger than tol, an extra boundary point is inserted at the middle of the i-th segment, i.e.,

$$t_{add} = \frac{t_{\mathrm{i}} + t_{\mathrm{i}+1}}{2}. \tag{3.31}$$

Then, the i-th segment is defined over the new time interval $\mathcal{T}_{add,\mathrm{i}} = [t_{\mathrm{i}}, t_{add}]$ and the $\mathrm{i}+1$-th segment is defined over $\mathcal{T}_{add,\mathrm{i}+1} = [t_{add}, t_{\mathrm{i}+1}]$, increasing the number of the total segments by 1. This process is repeated for all segments, $1 \leq \mathrm{i} \leq s$.

On the other hand, it may be desired to decrease the number of segments for smaller size of the problem and efficient computation. Consider a time interval over the i-th segment as well as the $\mathrm{i}+1$-th segment, $[t_{\mathrm{i}}, t_{\mathrm{i}+2}]$. The "true" state at $t_{\mathrm{i}+2}$ is obtained with the state at t_{i} as,

$$\boldsymbol{x}(t_{\mathrm{i}+2}) = \boldsymbol{\mathcal{F}}(t, \boldsymbol{\mathcal{F}}(t, \boldsymbol{x}(t_{\mathrm{i}}))), \tag{3.32}$$

where the explicit integration is conducted over $\mathcal{T}_{\mathrm{i}}$ as well as $\mathcal{T}_{\mathrm{i}+1}$. Then, the process is repeated with the collocation algorithm to find $\boldsymbol{x}_{col}(t_{\mathrm{i}+2})$ that satisfies,

$$\boldsymbol{\mathcal{G}}(t, \boldsymbol{x}(t_{\mathrm{i}}), \boldsymbol{x}_{col}(t_{\mathrm{i}+1})) = 0 \tag{3.33}$$

$$\boldsymbol{\mathcal{G}}(t, \boldsymbol{x}_{col}(t_{\mathrm{i}+1}), \boldsymbol{x}_{col}(t_{\mathrm{i}+2})) = 0. \tag{3.34}$$

The error of the collocation algorithm is defined as,

$$\epsilon_r = |\boldsymbol{x}_{col}(t_{\mathrm{i}+2}) - \boldsymbol{x}(t_{\mathrm{i}+2})|, \tag{3.35}$$

where subscript r indicates the error corresponds to the removing step. If the error ϵ_r is smaller than an user-selected tolerance level, tol_r, the intermediate boundary point $t_{\mathrm{i}+1}$ is deleted, since the segments are considered to be too dense. Then the new i-th segment becomes $\mathcal{T}_{remove,\mathrm{i}} = [t_{\mathrm{i}}, t_{\mathrm{i}+2}]$ and the number of segments decreases by 1. The process is repeated for all i-th segment for $1 \leq \mathrm{i} \leq s-1$. While the user can define any values for tol and tol_r, $1\mathrm{e}-12$ and $1\mathrm{e}-15$ have been selected in the current investigation.

The refinement process starts by removing the segments until $\epsilon_r > tol_r$. Then, the refinement process is repeated multiple times to ensure that the mesh satisfied $\epsilon < tol$. Note that the final solution may have segments where $\epsilon_r > tol_r$, but having more segments than necessary do not degrade the accuracy of the solution and further removal is not needed.

3.2 Newton-Raphson Method

A Newton-Raphson method is a numerical scheme that determines a root of an equation or a system of equations. For the collocation algorithm, Newton-Raphson method is utilized to determine the feasible solution of states and control that satisfy Equation (3.4) along with additional boundary and path constraints. The goal of Newton-Raphson method is to find a design vector $\boldsymbol{X}$, composed of n_d design variables, that satisfies a constraint vector $\boldsymbol{F}$ that consists of n_c scalar constraints,

$$\boldsymbol{F}(\boldsymbol{X}^*) = \boldsymbol{0}, \tag{3.36}$$

where $\boldsymbol{X} = \boldsymbol{X}^*$ denotes the root of the given constraint vector. When $\boldsymbol{X}^*$ cannot be found via an analytical relationship, it requires an iterative process based on a Taylor series expansion neglecting higher order terms around the root, $\boldsymbol{X}^*$, of Equation (3.36),

$$\boldsymbol{F}(\boldsymbol{X}^* + \Delta\boldsymbol{X}) \approx \boldsymbol{F}(\boldsymbol{X}^*) + D\boldsymbol{F}(\boldsymbol{X})\Delta\boldsymbol{X} = D\boldsymbol{F}\Delta\boldsymbol{X}, \tag{3.37}$$

where $\Delta \boldsymbol{X}$ is the deviation from $\boldsymbol{X}^*$ and $D\boldsymbol{F}(\boldsymbol{X})$ is the Jacobian of $\boldsymbol{F}$ with respect to $\boldsymbol{X}$. Assuming that at the i-th step of the iteration, $\boldsymbol{X} = \boldsymbol{X}_{\mathrm{i}}$ does not satisfy Equation (3.36) but is away from $\boldsymbol{X}^*$ by a small deviation $\Delta \boldsymbol{X}$, i.e.,

$$\boldsymbol{X}_{\mathrm{i}} = \boldsymbol{X}^* + \Delta \boldsymbol{X}, \tag{3.38}$$

Equation (3.37) is re-written as,

$$\boldsymbol{F}(\boldsymbol{X}_{\mathrm{i}}) = D\boldsymbol{F}(\boldsymbol{X}_{\mathrm{i}})\Delta \boldsymbol{X}_{approx}, \tag{3.39}$$

where $\Delta \boldsymbol{X}_{approx}$ denotes the approximate deviation from the root $\boldsymbol{X}^*$, since Equation (3.37) neglects higher-order terms. Solving Equation (3.39) for $\Delta \boldsymbol{X}_{approx}$, $\boldsymbol{X}_{\mathrm{i+1}}$ is computed as,

$$\boldsymbol{X}_{\mathrm{i+1}} = \boldsymbol{X}_{\mathrm{i}} - \Delta \boldsymbol{X}_{approx} \approx \boldsymbol{X}^*. \tag{3.40}$$

To compute $\boldsymbol{X}_{approx}$, the size of n_d and n_c should be compared, where the following two cases are considered.

1. For $n_d = n_c$, or when the number of design variables is same as the number of constraints, $\boldsymbol{X}_{approx}$ is uniquely determined via the inversion of the Jacobian,

$$\Delta \boldsymbol{X}_{approx} = (D\boldsymbol{F}(\boldsymbol{X}_{\mathrm{i}}))^{-1}\boldsymbol{F}(\boldsymbol{X}_{\mathrm{i}}). \tag{3.41}$$

   The matrix $D\boldsymbol{F}(\boldsymbol{X}_{\mathrm{i}})$ must be a non-singular matrix to allow the inverse matrix to exist, which is equivalent to having constraints that are linearly independently at a given $\boldsymbol{X}_{\mathrm{i}}$.

2. For $n_d > n_c$, or when the number of design variables is larger than the number of constraints, an infinite number of $\Delta \boldsymbol{X}_{approx}$ exist that satisfy Equation (3.39). While

multiple methods can be employed to select a specific solution among infinite choices, the minimum-norm solution is commonly utilized, i.e.,

$$\text{Minimize} \quad |\Delta \boldsymbol{X}_{approx}|^2 \tag{3.42}$$

$$\text{Subject to} \quad \boldsymbol{F}(\boldsymbol{X}_{\mathrm{i}}) = D\boldsymbol{F}(\boldsymbol{X}_{\mathrm{i}})\Delta \boldsymbol{X}_{approx}, \tag{3.43}$$

where $|\Delta \boldsymbol{X}_{approx}|^2 = \Delta \boldsymbol{X}_{approx}^T \Delta \boldsymbol{X}_{approx}$, or the square of the norm of $\Delta \boldsymbol{X}_{approx}$. This formulation represents the assumption that it is desirable to locate $\boldsymbol{X}^*$ that is closest to the given $\boldsymbol{X}_{\mathrm{i}}$. An augmented cost function is generated using a vector of Lagrangian multipliers, $\boldsymbol{\lambda}$,

$$\boldsymbol{G} = \Delta \boldsymbol{X}_{approx}^T \Delta \boldsymbol{X}_{approx} + \boldsymbol{\lambda}(\boldsymbol{F}(\boldsymbol{X}_{\mathrm{i}}) - D\boldsymbol{F}(\boldsymbol{X}_{\mathrm{i}})\Delta \boldsymbol{X}_{approx}). \tag{3.44}$$

Then, the minimum-norm solution is found when the following equations are satisfied,

$$\left(\frac{\partial \boldsymbol{G}}{\partial(\Delta \boldsymbol{X}_{approx})}\right)^T = 2\Delta \boldsymbol{X}_{approx} - D\boldsymbol{F}(\boldsymbol{X}_{\mathrm{i}})^T \boldsymbol{\lambda} = \boldsymbol{0} \tag{3.45}$$

$$\left(\frac{\partial \boldsymbol{G}}{\partial \boldsymbol{\lambda}}\right)^T = \boldsymbol{F}(\boldsymbol{X}_{\mathrm{i}}) - D\boldsymbol{F}(\boldsymbol{X}_{\mathrm{i}})\Delta \boldsymbol{X}_{approx} = \boldsymbol{0}, \tag{3.46}$$

i.e., the first derivatives of the augmented cost function must be zero vectors with respect to both $\Delta \boldsymbol{X}_{approx}$ and $\boldsymbol{\lambda}$ to be a stationary point. The combination of $\boldsymbol{\lambda}$ and $\Delta \boldsymbol{X}_{approx}$ that satisfy the necessary conditions are,

$$\boldsymbol{\lambda} = 2\Big(D\boldsymbol{F}(\boldsymbol{X}_{\mathrm{i}})(D\boldsymbol{F}(\boldsymbol{X}_{\mathrm{i}}))^T\Big)^{-1} \boldsymbol{F}(\boldsymbol{X}_{\mathrm{i}}) \tag{3.47}$$

$$\Delta \boldsymbol{X}_{approx} = (D\boldsymbol{F}(\boldsymbol{X}_{\mathrm{i}}))^T \Big(D\boldsymbol{F}(\boldsymbol{X}_{\mathrm{i}})(D\boldsymbol{F}(\boldsymbol{X}_{\mathrm{i}}))^T\Big)^{-1} \boldsymbol{F}(\boldsymbol{X}_{\mathrm{i}}), \tag{3.48}$$

where Equation (3.48) corresponds to the minimum-norm solution and is utilized.

3. For $n_d > n_c$, $\Delta \boldsymbol{X}_{approx}$ that satisfies Equation (3.39) does not exist in general. Although an optimization problem can be formulated to select $\Delta \boldsymbol{X}_{approx}$ that is most desirable, it is not explained in detail as this case does not correspond to the design problem examined in the current investigation.

3.3 Direct Optimization

When generating low-thrust transfer trajectories, the goal is often to obtain trajectories that minimize a function of costs represented as the propellant consumption and the time of flight. This optimization problem is categorized as a special case of an *optimal control problem* [63], that is mathematically described with (1) the equations of motion, (2) constraints, and (3) the cost function. The equations of motion refer to a given set of N first-order differential equations that govern the dynamics of the state vector,

$$\dot{\boldsymbol{x}} = \boldsymbol{f}(t, \boldsymbol{x}, \boldsymbol{u}, \boldsymbol{\rho}), \ (t_I \leq t \leq t_F) \tag{3.49}$$

where t_I and t_F denote the initial and final time of the problem, and $\boldsymbol{\rho}$ denotes a additional set of parameters that are constant across time. The constraints are categorized into boundary constraints, path constraints, and the bounds for the states and the control. The boundary constraints refer to the initial and final conditions, described as,

$$\boldsymbol{\Psi}_{I,l} \leq \boldsymbol{\Psi}_I[t_I, \boldsymbol{x}(t_I), \boldsymbol{u}(t_I), \boldsymbol{\rho}] \leq \boldsymbol{\Psi}_{I,u} \tag{3.50}$$

$$\boldsymbol{\Psi}_{F,l} \leq \boldsymbol{\Psi}_I[t_F, \boldsymbol{x}(t_F), \boldsymbol{u}(t_F), \boldsymbol{\rho}] \leq \boldsymbol{\Psi}_{F,u}, \tag{3.51}$$

where $\boldsymbol{\Psi}$ refers to a vector bounds with subscripts I, F denoting the initial and final time respectively, and subscripts l, u denoting the lower and upper bounds, respectively. Equality constraints are achieved by setting the upper bounds equal to the lower bounds. Additionally, there exist path constraints, or the constraints that must be satisfied at the inside of the initial and final times,

$$\boldsymbol{g}_l \leq \boldsymbol{g}[t, \boldsymbol{x}(t), \boldsymbol{u}(t), \boldsymbol{\rho}] \leq \boldsymbol{g}_u. \tag{3.52}$$

And bounds may exist for the state and control as,

$$\boldsymbol{x}_l \leq \boldsymbol{x} \leq \boldsymbol{x}_u \tag{3.53}$$

$$\boldsymbol{u}_l \leq \boldsymbol{u} \leq \boldsymbol{u}_u, \tag{3.54}$$

completing the definitions of constraints. Finally, a scalar cost is defined as,

$$J_o = \phi(t_F, \boldsymbol{x}(t_F), \boldsymbol{u}(t_F), \boldsymbol{\rho}) + \int_{t_I}^{t_F} L[t_F, \boldsymbol{x}(t_F), \boldsymbol{u}(t_F), \boldsymbol{\rho})dt, \tag{3.55}$$

where ϕ and L correspond to the terminal and the path costs, respectively. Solving the optimization problem is equivalent to finding $\boldsymbol{x}(t)$, $\boldsymbol{u}(t)$ and $\boldsymbol{\rho}$ that minimize J while satisfying all the constraints.

Multiple strategies exist to solve optimization problems for continuous time systems, and they are generally categorized into three kinds [59]: direct, indirect and global optimization methods via evoluationary algorithms (EAs). As a direct optimization method has been employed in the current investigation, detailed explanation of the method is provided, followed by the comparisons with the other methods. Note that there exist methods that cannot be strictly classified into the three categories. Hybrid methods, for example, combine more than one optimization methods.

A direct optimization method discretizes the state and control method, and the problem is represented as a finite set of variables [57]. Then, this finite-dimensional problem is solved via a parameter optimization method, also known as the nonlinear programming (NLP). The goal of a NLP problem is to locate a design vector $\boldsymbol{X}$ of dimensions $n_d \times 1$ that minimizes a scalar objective function,

$$J_o = J_o(\boldsymbol{X}), \tag{3.56}$$

subject to n_m constraints,

$$\boldsymbol{c}_L \leq \boldsymbol{c}(\boldsymbol{X}) \leq \boldsymbol{c}_U, \tag{3.57}$$

and bounds,

$$\boldsymbol{X}_L \leq \boldsymbol{X} \leq \boldsymbol{X}_U. \tag{3.58}$$

The subscripts L, U refer to the lower and upper constraints and bounds. The constraint functions $\boldsymbol{c}(\boldsymbol{X})$ taks an arbitrary form, hence labeled NLP for the general, nonlinear constraints. Note that the dynamics for the problem is converted into the algebraic constraints, so the dynamics is not explicitly present within the NLP. Finding $\boldsymbol{X}$ that minimizes the objective function while satisfying all constraints as well as bounds is achieved via the Karush-Kuhn-Tucker (KKT) condition. A specific case, where $\boldsymbol{c}_L = \boldsymbol{c}_U$ and bounds do not exist, is examined to derive the KKT condition. First consider an augmented cost function,

$$L_o = J_o + \boldsymbol{\lambda}_o^T \boldsymbol{c}(\boldsymbol{X}), \tag{3.59}$$

where $\boldsymbol{\lambda}_o$ is a $n_m \times 1$ Lagrange multiplier vector. Then for a set of vectors $(\boldsymbol{X}^*, \boldsymbol{\lambda}_o^*)$ that minimize L, the necessary conditions are derived as,

$$\frac{\partial L_o}{\partial \boldsymbol{X}} = \boldsymbol{0} \tag{3.60}$$

$$\frac{\partial L_o}{\partial \boldsymbol{\lambda}_o} = \boldsymbol{0}. \tag{3.61}$$

Since the roots are needed for Equations (3.60) and (3.61), a Newton-Raphson method can be applied to iteratively search for a combination of $\boldsymbol{X}$ and $\boldsymbol{\lambda}_o$. Equations (3.60) and (3.61) represent the KKT conditions, although the exact forms of the equation vary depending on the existence of the inequality constraints and the bounds on $\boldsymbol{X}$. A rich number of software or functions, both open-source and proprietary, exist to solve the NLP problem, including SNOPT [40], MATLAB's *fmincon* [64], IPOPT [65] and GPOPS-II [66]. The open-source software, IPOPT [65], has been utilized throughout the current investigation to generate optimal trajectories.

3.3.1 Comparison with Indirect Optimization Methods

Indirect optimization method utilizes the calculus of variations, and the necessary conditions of optimality are satisfied by applying Euler-Lagrange theorem. The optimization problem is recast into a two-point boundary value problem (TPBVP) where the costate variables are found. The indirect method results in rapid convergence given a good starting

guess for the initial costates, and an accurate solution of the optimal control can be located, as it is an outcome of the analytical optimal condition acquired via the Euler-Lagrange theorem. However, it is associated with several disadvantages compared to the direct method. The convergence radius is typically small, or it is challenging to find the initial guess that results in a solution TPBVP [57]. On the other hand, the direct optimization methods tend to be more robust to poor initial guesses, but have a larger dimension of parameters compared to the indirect method.

3.3.2 Comparison with Evolutionary Algorithms

Evolutionary algorithms (EA's) correspond to the more recent development in the optimization field, and utilize mechanisms that are inspired by the biological evolution [59]. Some of the best known methods of EA's include genetic algorithms, Particle Swarm Optimizer and ant colony optimization. The conventional indirect and direct methods rely on the necessary condition of the optimality, i.e., E-L theorem for the indirect method and KKT conditions for the direct method. These methods all require gradient-based methods including the Newton-Raphson method and NLP solvers. On the contrary, EA's in general do not require gradient-based methods as well as an initial guess to start the iteration. This feature is advantageous, as providing an initial guess that is close enough to a local minimum tends to be the most challenging step in utilizing the gradient-based methods, both for the indirect and direct methods. Additionally , EA's are capable of converging to the global minima of the solutions that are not readily accessible with the gradient-based methods. Despite these merits, EA's typically require significantly more computational resources and time compared to the gradient-based methods.

3.4 Low-Thrust Trajectory Design with Direct Collocation

The direct collocation algorithm is applied to the low-thrust trajectory design problem. Since the gravitational force models have second derivative terms, it is necessary to define the state vector $\boldsymbol{x}$ as,

$$\boldsymbol{x} = \begin{bmatrix} x & y & z & \dot{x} & \dot{y} & \dot{z} & m \end{bmatrix}^T, \tag{3.62}$$

corresponding to the position, velocity and mass in the CR3BP rotating frame in the nondimensional units. Note that the state vector can be alternatively represented in other frames too. For example, representation in the J2000 frame results in,

$$\boldsymbol{x}_J = \begin{bmatrix} X_J & Y_J & Z_J & \dot{X}_J & \dot{Y}_J & \dot{Y}_J & m \end{bmatrix}^T, \tag{3.63}$$

where X_J and $\dot{X}_J$ denote the position and inertial velocity in the J2000 frame, nondimensionlized with the user-selected CR3BP characteristic quantities. While the implemented direct collocation algorithm is capable of handling states represented in different frames, $\boldsymbol{x}$ is assumed to be associated with the CR3BP rotating frame for the explanation here. Next, the control vector, $\boldsymbol{u}$, is defined as,

$$\boldsymbol{u} = \begin{bmatrix} T & u_x & u_y & u_z \end{bmatrix}^T, \tag{3.64}$$

where T corresponds to the nondimensional low-thrust engine force, and u_x, u_y, u_z are the components of the thrust direction unit vector, i.e.,

$$\hat{u}_T = u_x\hat{x} + u_y\hat{y} + u_z\hat{z}. \tag{3.65}$$

Similar to the state, the control vector is represented in different frames as well. For example,

$$\boldsymbol{u}_J = \begin{bmatrix} T & u_{X_J} & u_{Y_J} & u_{Z_J} \end{bmatrix}^T, \tag{3.66}$$

where u_{X_J} corresponds to the thrust direction component in the $\hat{X}_J$ direction of the J2000 frame. Then, the dynamics is fully represented by the following first order vector differential equation,

$$\dot{\boldsymbol{x}} = \boldsymbol{f}(\boldsymbol{x}, \boldsymbol{u}, \boldsymbol{\rho}), \tag{3.67}$$

where $\boldsymbol{f}$ corresponds to the first order vector differential equations. The vector $\boldsymbol{\rho}$ corresponds to the constant parameters that includes the specific impulse of the engine, I_{sp} and the standard gravitational parameter, g_0. Note that $\boldsymbol{f}$ is not a function of time, since the CR3BP is a time-independent system. Writing out each component of Equation (3.67),

$$\dot{\boldsymbol{x}} = \boldsymbol{f}(\boldsymbol{x}, \boldsymbol{u}, \boldsymbol{\rho}) = \begin{bmatrix} \dot{x} \\ \dot{y} \\ \dot{z} \\ 2\dot{y} + \frac{\partial U^*}{\partial x} + \frac{Tu_x}{m} \\ -2\dot{x} + \frac{\partial U^*}{\partial y} + \frac{Tu_y}{m} \\ \frac{\partial U^*}{\partial z} + \frac{Tu_z}{m} \\ \frac{T}{I_{sp} \cdot g_0} \end{bmatrix}, \tag{3.68}$$

where the rows 4-7 are identical to Equations (2.102)-(2.105). With the definitions of the state and control vectors, as well as the first order equations of motion, the direct collocation technique is applied.

Applying the direct collocation technique to the low-thrust trajectory design problem typically requires three steps, illustrated in Figure 3.1. As the iterative process of direct collocation algorithm resorts on gradient based methods, it often fails to converge if the starting point of the algorithm is not near a local basin. The optimization process often requires significant computation time, and providing a "good" starting point is the key to obtaining an optimized trajectory. This challenge is overcome by the extra steps prior to the optimization. First, an initial guess is generated that need not satisfy all the design constraints. The initial guess guides the corrections process, through which the it is converged to a feasible trajectory. A feasible trajectory refers to a solution that satisfies all the design

constraints. The existence of a feasible trajectory alludes to the existence of a local basin as well, at the bottom of which resides an optimal trajectory. Since the corrections process typically take less time compared to the optimization process, obtaining a feasible trajectory first prevents the waste of time searching for a local basin that may not exist. Note that when ultimately validating a trajectory in a higher-fidelity ephemeris model, the process in Figure 3.1 is repeated. It is first employed for a lower-fidelity dynamics model, and the resulting optimized trajectory is utilized as an initial guess in a higher-fidelity model and then is converged to an optimal trajectory again.

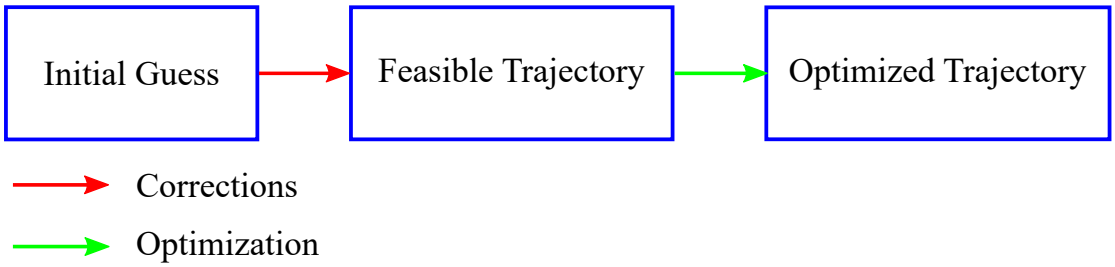

Figure 3.1. Process of low-thrust trajectory design

3.4.1 Design Variable Vector Formulation

Recall that a Newton-Raphson method as well as a NLP algorithm requires a $n_d \times 1$ design vector $\boldsymbol{X}$ that determines n_d scalar design variables. For the low-thrust trajectory design problem, the design variables are categorized into the state, control, slack variables, as well as the optional, additional variables. First, the states at the variable nodes of each segment form $\boldsymbol{X}_s$,

$$\boldsymbol{X}_s = \begin{bmatrix} \boldsymbol{x}_{1,1}^T & \boldsymbol{x}_{1,3}^T & \boldsymbol{x}_{1,5}^T & \boldsymbol{x}_{1,7}^T & \cdots & \boldsymbol{x}_{s,1}^T & \boldsymbol{x}_{s,3}^T & \boldsymbol{x}_{s,5}^T & \boldsymbol{x}_{s,7}^T \end{bmatrix}^T, \tag{3.69}$$

where the subscripts i, k pair refers to the states belonging to i-th segment where $1 \leq \mathrm{i} \leq s$, and k is the index of the variable nodes. Similarly, the control of each segment form $\boldsymbol{X}_u$,

$$\boldsymbol{X}_u = \begin{bmatrix} \boldsymbol{u}_1^T & \boldsymbol{u}_2^T & \cdots & \boldsymbol{u}_s^T \end{bmatrix}^T, \tag{3.70}$$

where $\boldsymbol{u}_{\mathrm{i}}$ corresponds to the control vector at each segment,

$$\boldsymbol{u}_{\mathrm{i}} = \begin{bmatrix} T_{\mathrm{i}} & u_{x,\mathrm{i}} & u_{y,\mathrm{i}} & u_{z,\mathrm{i}} \end{bmatrix}^T. \tag{3.71}$$

Note that the components of the control vector are constant over each segment; the thrust and the direction do not change within a segment. While this assumption may limit the optimality of the final solution, it helps reduce the size of the design vector and mirrors the "turn and hold" strategy that is utilized in realistic missions [67]. Next, the slack variables that are necessary to handle inequality constraints form $\boldsymbol{X}_{slack}$,

$$\boldsymbol{X}_{slack} = \begin{bmatrix} \sigma_1 & \sigma_2 & \cdots & \sigma_s \end{bmatrix}^T, \tag{3.72}$$

where the slack variable σ_{i} corresponds to an inequality constraint over i-th segment. If other inequality constraints exist, the additional slack variables $\begin{bmatrix} \kappa_1 & \kappa_2 & \cdots & \kappa_s \end{bmatrix}^T$ are concatenated to $\boldsymbol{X}_{slack}$. Finally, depending on the setup of the problem, additional variables may be incorporated,

$$\boldsymbol{X}_{add} = \begin{bmatrix} x_{add,1} & x_{add,2} & \cdots & x_{add,n_a} \end{bmatrix}^T, \tag{3.73}$$

where $x_{add,\mathrm{j}}$ corresponds to any additional design variables where $1 \leq \mathrm{j} \leq n_a$, where n_a corresponds to the number of the additional design variables. The design vector $\boldsymbol{X}$ is formed by concatenating the above vectors,

$$\boldsymbol{X} = \begin{bmatrix} \boldsymbol{X}_s^T & \boldsymbol{X}_u^T & \boldsymbol{X}_{slack}^T & \boldsymbol{X}_{add}^T \end{bmatrix}^T. \tag{3.74}$$

When $n_a = 0$, $\boldsymbol{X}_{add}$ becomes a blank vector and is not incorporated to the design vector, $\boldsymbol{X}$. The concatenated vector, $\boldsymbol{X}$, is utilized as the design vector of the Newton-Raphson method and the NLP algorithm.

3.4.2 Constraint Vector Formulation

The design constraints associated with the low-thrust trajectory design are incorporated into a constraint vector. Assume the Newton-Raphson method is employed to obtain a feasible solution, then from Equation (3.36),

$$\boldsymbol{F} = \boldsymbol{F}(\boldsymbol{X}), \tag{3.75}$$

where the constraint vector $\boldsymbol{F}$ depends on the design vector $\boldsymbol{X}$, and it consists of different types of constraints. First, consider the dynamical constraints that are formed as the defect constraints by Equation (3.27),

$$\boldsymbol{F}_{defect} = \begin{bmatrix} \Delta_1^T & \Delta_2^T & \cdots & \Delta_s^T \end{bmatrix}^T, \tag{3.76}$$

where Δ_{i} is the defect constraints over i-th segment and the dimensions are 21×1. The next type of the constraint is the continuity of the states at the boundary points of mesh,

$$\boldsymbol{F}_{cont} = \begin{bmatrix} (\boldsymbol{x}_{2,1} - \boldsymbol{x}_{1,7})^T & (\boldsymbol{x}_{3,1} - \boldsymbol{x}_{2,7})^T & \cdots & (\boldsymbol{x}_{s,1} - \boldsymbol{x}_{s-1,7})^T \end{bmatrix}, \tag{3.77}$$

where $\boldsymbol{x}_{\mathrm{i}+1,1} - \boldsymbol{x}_{\mathrm{i},7}$ corresponds to the continuity constraint between the state of the first variable node of the $(\mathrm{i}+1)$-th segment and the state of the last variable node of the i-th segment for $1 \leq \mathrm{i} \leq s-1$. Next, an inequality constraint exists for the magnitude of the thrust, or recalling Equation (2.91),

$$0 \leq T_{\mathrm{i}} \leq T_{max}, \tag{3.78}$$

where T_{i} corresponds to the thrust magnitude at each segment. This inequality constraint is transformed to an equality constraint by utilizing the slack variables as,

$$\boldsymbol{F}_{T,slack} = \begin{bmatrix} (T_1 - T_{max}\sin(\sigma_1)^2) & (T_2 - T_{max}\sin(\sigma_2)^2) & \cdots & (T_s - T_{max}\sin(\sigma_s)^2) \end{bmatrix}, \tag{3.79}$$

where σ_{i} is the slack variable at the i-th segment that belongs to $\boldsymbol{X}_{slack}$. Also, an equality constraint is imposed on the direction vector of the thrust direction to be 1,

$$\boldsymbol{F}_{T,unit} = \begin{bmatrix} (u_{x,1}^2 + u_{y,1}^2 + u_{z,1}^2 - 1) & (u_{x,2}^2 + u_{y,2}^2 + u_{z,2}^2 - 1) & \cdots & (u_{x,s}^2 + u_{y,s}^2 + u_{z,s}^2 - 1) \end{bmatrix}^T. \tag{3.80}$$

Next, boundary constraints, if they exist, are imposed at the initial and the final states as,

$$\boldsymbol{F}_{\mathrm{ini}} = \boldsymbol{x}_{1,1}(\mathbf{j}_{\mathrm{ini}}) - \boldsymbol{x}_{\mathrm{ini}} \tag{3.81}$$

$$\boldsymbol{F}_{fin} = \boldsymbol{x}_{s,7}(\mathbf{j}_{fin}) - \boldsymbol{x}_{fin}, \tag{3.82}$$

where $\boldsymbol{x}_{\mathrm{ini}}$ and $\boldsymbol{x}_{fin}$ are user-defined initial and final states. $\mathbf{j}$ corresponds to the index vector of the component that needs to be targeted. For example, if $\mathbf{j}_{\mathrm{ini}} = \begin{bmatrix} 1 & 3 \end{bmatrix}^T$, the first and third components of the state vector, or x and z of the initial state are incorporated as the boundary constraints. Typically, following index vectors are utilized,

$$\mathbf{j}_{\mathrm{ini}} = \begin{bmatrix} 1 & 2 & 3 & 4 & 5 & 6 & 7 \end{bmatrix}^T \tag{3.83}$$

$$\mathbf{j}_{fin} = \begin{bmatrix} 1 & 2 & 3 & 4 & 5 & 6 \end{bmatrix}^T, \tag{3.84}$$

where all seven components are targeted for the initial state, and all components except the mass are targeted for the final state. These index vectors can also be blank, corresponding to a problem without any boundary constraints. Finally, an additional constraint vector $\boldsymbol{F}_{add}$ can be incorporated. The additional constraints may include a minimum distance constraint from the gravitational bodies, or inexact forms of boundary constraints such as departure from periodic orbits, where $\boldsymbol{x}_{\mathrm{ini}}$ and $\boldsymbol{x}_{fin}$ also depend on additional variables, $\boldsymbol{X}_{add}$. The constraint vector $\boldsymbol{F}$ is formed as,

$$\boldsymbol{F} = \begin{bmatrix} \boldsymbol{F}_{defect}^T & \boldsymbol{F}_{cont}^T & \boldsymbol{F}_{T,slack}^T & \boldsymbol{F}_{T,unit}^T & \boldsymbol{F}_{\mathrm{ini}}^T & \boldsymbol{F}_{fin}^T & \boldsymbol{F}_{add}^T \end{bmatrix}^T. \tag{3.85}$$

While the general structures of $\boldsymbol{X}$ and $\boldsymbol{F}$ persists, $\boldsymbol{X}_{add}$, $\boldsymbol{F}_{\mathrm{ini}}, \boldsymbol{F}_{fin}, \boldsymbol{F}_{add}$ may vary much depending on the specific scenarios. Also note that the variable vector and the constraint

vector for the NLP problem is similar, but typically result in a smaller number of variables and constraints as the linear constraints are handled separately, i.e., the user need not define slack variables.

3.4.3 Jacobian Formulation

Recall that the gradient based methods, i.e., the Newton-Raphson method and NLP algorithms, all depend on computing the Jacobian of the constraint vector with respect to the design vector,

$$D\boldsymbol{F}(\boldsymbol{X}) = \frac{\partial \boldsymbol{F}}{\partial \boldsymbol{X}}. \tag{3.86}$$

As $\boldsymbol{X}$ and $\boldsymbol{F}$ consist of different categories of variables and constraints, it is more efficient to compute different parts of the Jacobian matrix separately and then concatenate the parts together. Consider the Jacobian of the defect constraint $\boldsymbol{F}_{defect}$ with respect to the state variable vector $\boldsymbol{X}_s$,

$$\frac{\partial \boldsymbol{F}_{defect}}{\partial \boldsymbol{X}_s}. \tag{3.87}$$

One advantageous trait of the Jacobian from the collocation algorithm is that it typically results in a sparse matrix. For example, the i-th defect constraints Δ_{i} is a function only of the states of the same segment, i.e.,

$$\Delta_{\mathrm{i}} = \Delta_{\mathrm{i}}(\boldsymbol{x}_{\mathrm{i},1}, \boldsymbol{x}_{\mathrm{i},3}, \boldsymbol{x}_{\mathrm{i},5}, \boldsymbol{x}_{\mathrm{i},7}). \tag{3.88}$$

Thus, the matrix from Equation (3.87) is written as a sparse matrix,

$$\frac{\partial \boldsymbol{F}_{defect}}{\partial \boldsymbol{X}_s} = \begin{bmatrix} \frac{\partial \Delta_1}{\partial \boldsymbol{x}_1} & \mathbf{0}_{21\times 28} & \cdots & \mathbf{0}_{21\times 28} \\ \mathbf{0}_{21\times 28} & \frac{\partial \Delta_2}{\partial \boldsymbol{x}_2} & \cdots & \mathbf{0}_{21\times 28} \\ \vdots & \vdots & \ddots & \vdots \\ \mathbf{0}_{21\times 28} & \mathbf{0}_{21\times 28} & \cdots & \frac{\partial \Delta_s}{\partial \boldsymbol{x}_s} \end{bmatrix}, \tag{3.89}$$

where $\boldsymbol{x}_{\mathrm{i}}$ is a 28×1 vector composed of $\boldsymbol{x}_{\mathrm{i},1}, \boldsymbol{x}_{\mathrm{i},3}, \boldsymbol{x}_{\mathrm{i},5}$, and $\boldsymbol{x}_{\mathrm{i},7}$. $\frac{\partial \Delta_{\mathrm{i}}}{\partial \boldsymbol{x}_{\mathrm{j}}}$ is a zero matrix of dimensions 21×28 if $\mathrm{i} \neq \mathrm{j}$. Thus, only the non-zero elements are computed to leverage the sparsity of the matrix from Equation (3.87). Other parts of the Jacobian matrix $D\boldsymbol{F}(\boldsymbol{X})$ also have sparse structures that are leveraged for efficient computations. Figure 3.2 illustrates the sparsity pattern of the Jacobian $D\boldsymbol{F}(\boldsymbol{X})$ when the number of the segment, s, is three, where the blue dots correspond to the non-zero elements. For simplicity, additional variables as well as additional constraints are not considered. Note that as the segment number grows, the Jacobian becomes more sparse, or the ratio of the non-zero elements decreases.

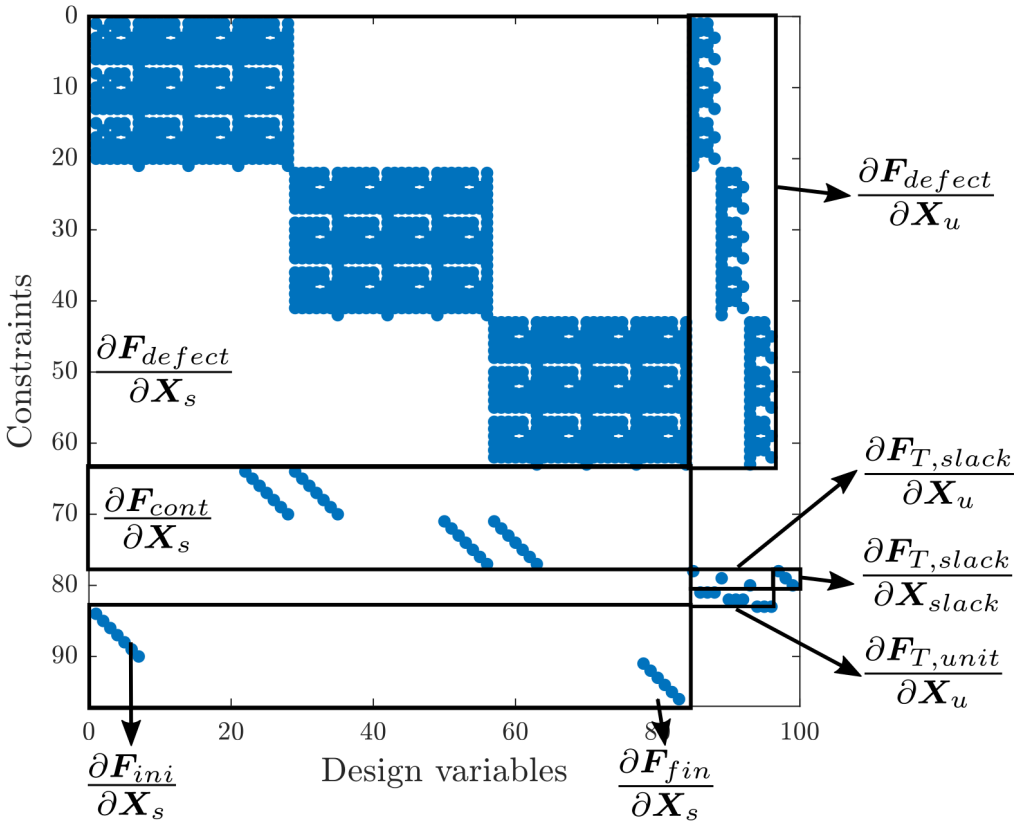

Figure 3.2. Sparsity pattern of the Jacobian matrix $D\boldsymbol{F}(\boldsymbol{X})$ for $s = 3$

The non-zero elements of the Jacobian is computed analytically if the constraint equations allows an analytical differentiation with respect to the design vector. Otherwise, a numerical

method, also known as the finite difference method, is utilized to compute the elements of the Jacobian.

3.4.4 Cost Function for Optimization

The two main costs associated with the low-thrust trajectory are the propellant and the time of flight. While either of these two cost variables, or even a combined cost may be utilized, this investigation only considers the minimization of the propellant consumption. The cost function is formulated as,

$$J_o = -m_{s,7}, \tag{3.90}$$

where $m_{s,7}$ corresponds to the final mass of the spacecraft. Minimizing J_o is equivalent to minimizing the propellant consumption over the trajectory. Optimal or optimized trajectories in this work refer to trajectories that minimize the defined cost function, J_o. These optimal trajectories are also denoted the propellant optimal or mass optimal trajectories throughout the current analysis.

3.4.5 An Example Scenario

The low-thrust trajectory design via direct collocation is illustrated with a sample scenario which is recreated from the work by Pritchett [60]. Consider a transfer between L_1 halo orbit a L_2 halo orbit in the Earth-Moon CR3BP, where the initial and final states of the transfer as well as the associated Jacobi constants are included in Table 3.1. The spacecraft is assumed to be associated with the initial mass of $2000kg$ and is equipped with a low-thrust engine with $\tilde{I_{sp}} = 2000s$ and $\tilde{T}_{max} = 0.2N$. Figure 3.3 illustrates the process of low-thrust trajectory design, both for the state history of the transfer trajectory in the three-dimensional position space, as well as the control history. Figure 3.3(a) represents the initial guess of the transfer, which consists of one ballistic revolution of the initial L_1 halo orbit and two ballistic revolutions of the final L_2 halo orbit. This strategy is denoted orbit stacking, where ballistic periodic orbits of the CR3BP are stacked as an initial guess of the state history [60]. This initial guess results in the violation of the constraints as the trajectory is not continuous.

Figure 3.3(b) illustrates the control history, or the thrust profile of the initial guess. Note that the magnitude of the thrust is assumed to be 70% of the maximum thrust level. And the thrust vector is selected to be parallel to the rotating velocity vector. This initial guess for the state and control is passed to the Newton-Raphson algorithm to converge in Figure 3.3(c) and 3.3(d). Note that the blue lines indicates the segments where the thrust is below 5% of the maximum thrust, T_{max}. The dotted lines illustrate the initial and final halo orbits. The feasible trajectory is utilized as the starting point for the NLP solver, and results in the optimal trajectory as illustrated in Figure 3.3(e) and 3.3(f). It is evident that it requires less propellant after the optimization, as the thrust profile indicates less thrust segments. Note that the optimization process employs J_o defined from Equation (3.90) and does not change the time of flight of the transfer. The optimal trajectory requires $\Delta m = 18.57$kg for $TOF = 40.75$days.

Table 3.1. Sample transfer scenario between Earth-Moon L_1 halo orbit and Earth-Moon L_2 halo orbit: initial and final states information

	Initial State	Final State
Orbit	L_1 halo orbit	L_2 halo orbit
x [n.d.]	0.828389	1.163325
z [n.d.]	0.103044	0.115930
$\dot{z}$ [n.d.]	0.218573	-0.204262
JC [n.d.]	3.099490	3.099800

If the goal is to generate generate a trajectory in a higher-fidelity model, the feasible or optimal trajectory from a lower-fidelity model, e.g., CR3BP, can be utilized as the initial guess again. This process is illustrated in Figure 3.4. Figure 3.4(a) illustrates the initial guess from the CR3BP as the dotted cyan arc. Utilizing this arc as the initial guess, the design process in Figure 3.1 is repeated in the Sun-Earth-Moon ephemeris model, resulting in a magenta arc. Note that the transformation Equation (2.71) is utilized to transform the states into the J2000 frame first, and they are rotated back into the Earth-Moon CR3BP rotating frame. Figure 3.4(a) illustrates the thrust profile of the optimal trajectory in the higher-fidelity ephemeris model. Although the magnitude of the thrust reveals similar trend as in Figure 3.3(f), the components of the thrust vector are different as the thrust direction is

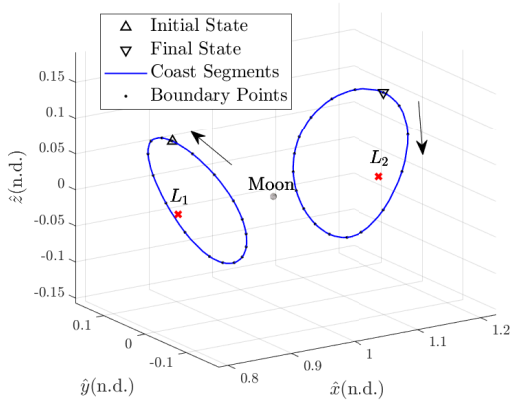

(a) Initial guess of the state in the position space

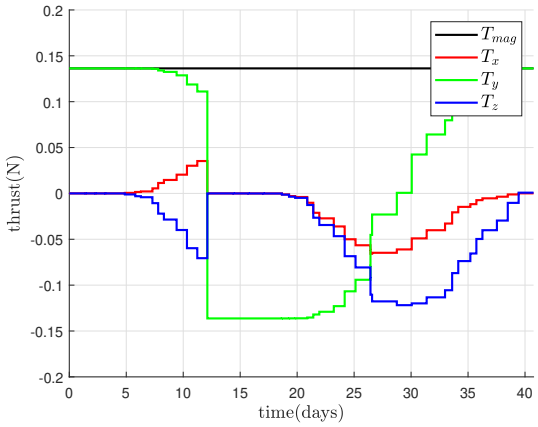

(b) Initial guess of the control

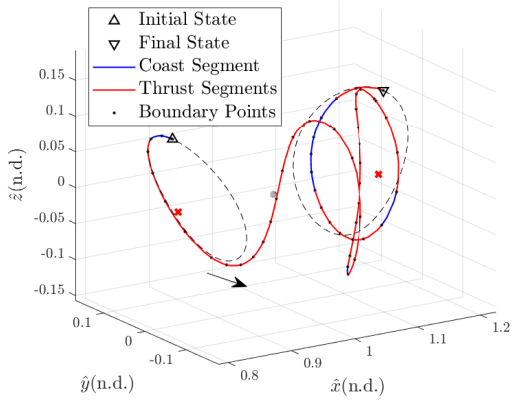

(c) Feasible trajectory in the position space

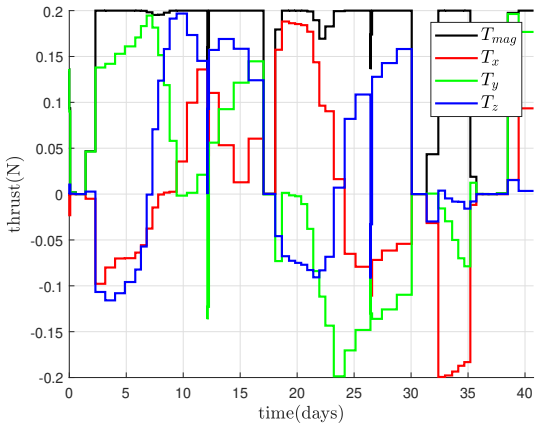

(d) Feasible trajectory: control

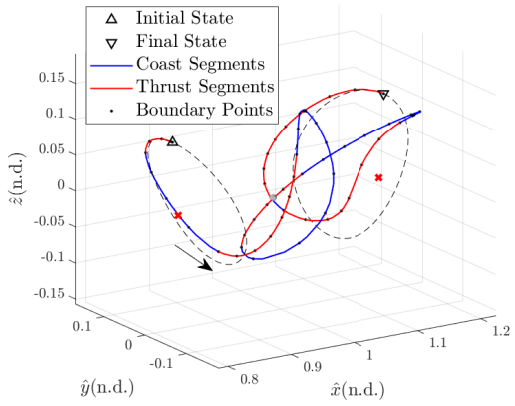

(e) Optimal trajectory in the position space

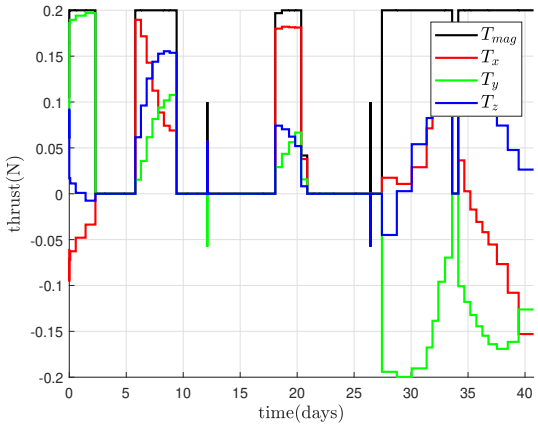

(f) Optimal trajectory: control

Figure 3.3. An example transfer from the L_1 halo orbit to L_2 halo orbit in the Earth-Moon CR3BP

defined in $\hat{X}_J - \hat{Y}_J - \hat{Z}_J$ unit vectors instead of $\hat{x} - \hat{y} - \hat{z}$ unit vectors. The optimal trajectory requires $\Delta m = 18.30kg$ for $TOF = 40.75days$.

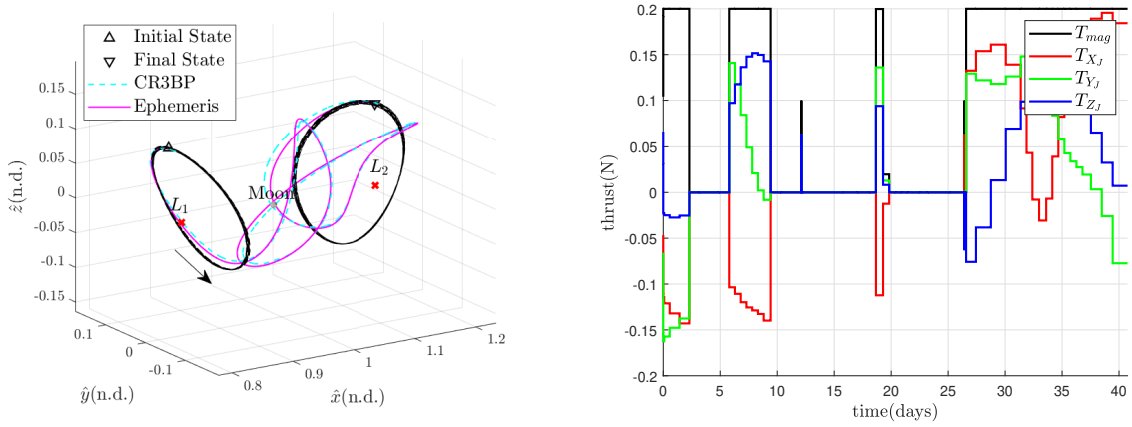

(a) Optimal trajectory

(b) Initial guess for the control

Figure 3.4. An example transfer from the L_1 halo orbit to L_2 halo orbit in the Sun-Earth-Moon ephemeris model

4. HELIOCENTRIC LEG DESIGN

Any potential mission from the Earth to Mars with a low-thrust engine expends a considerable amount of propellant in the heliocentric space. Woolley et al. [38] indicate that for a mission from a GTO to Phobos, the propellant spent for the heliocentric leg accounts for more than a half of the total propellant consumption. Thus, analyzing the the optimal propellant costs corresponding to the heliocentric leg, is a necessary step.

The most immediate challenge with computing the heliocentric leg is the time-dependent nature of the problem; the locations of the planets in the heliocentric space are constantly changing. Moreover, the transfer trajectories between the Earth and Mars are not perfectly periodic [23]. Table 4.1 includes the mean orbital elements of the Earth and Mars around the Sun over the time span between 2000 and 2050, where the inclination, i_K, is computed with respect to the ECLIPJ2000, or the Earth ecliptic inertial frame. The information is obtained from the SPICE database [50]. The orbit of Mars is associated with a large eccentricity compared to that of the Earth, and it is slightly inclined with respect to the Earth ecliptic plane. Thus, the relative configuration of the planets in heliocentric space does not exactly repeat itself, as the orbits of the Earth and Mars are not coplanar nor circular. Instead, the configuration is uniquely defined by a selected pair of departure and arrival epochs. The heliocentric leg, or the transfer trajectory between the Earth and Mars is characterized by separately obtaining solutions corresponding to a range of possible configurations of the planets.

Table 4.1. Sun-2BP orbital data of the Earth and Mars

	a_K [km]	e_K [nd]	i_K [°]
Earth	1.497×10^8	0.017	0.001
Mars	2.279×10^8	0.093	1.850

Utilizing an impulsive engine, or an engine that is capable of imparting an instantaneous change in velocity, characterizing the transfer trajectories between the Earth and Mars is relatively straightforward. Traditionally, Lambert's equation has been employed, where a two-point boundary value problem is formulated based on the departure and arrival epochs.

The positions of the planets in heliocentric space are retrieved at the respective epochs and set as the boundary constraints of the transfer arc. Then, an iterative solver is utilized to solve for the initial and final velocities that result in a ballistic, Sun-2BP conic arc that links the boundary positions with the given time of flight. The impulsive engine provides the required velocity changes between the end points of the ballistic arc and the states of the planets, corresponding to the cost associated with the transfer. This method is employed for a range of departure and arrival epochs of interest to obtain multiple transfer arcs. To efficiently illustrate the trend of cost over the epochs, a contour plot, denoted "porkchop plot", is produced from the solutions to characterize the transfer trajectories and guide the mission design process [68].

On the contrary, a ballistic transfer arc cannot be utilized for a low-thrust engine as it fails to instantaneously deliver the required velocity change at the ends of the ballistic arc. Rather, it results in a continuous optimal control problem where the history of the state and control that enables a transfer between the planets must be obtained. It is further compounded by the fact that the low-thrust trajectory optimization problem also depends on additional design parameters including the Earth departure scenario as well as the spacecraft specifications (Table 1.1), which necessitates simplifying assumptions. Previous authors investigate methods that iteratively solve the optimal control problem over multiple pairs of epochs under specific assumptions. Woolley et al. [38] compute families of optimal trajectories by approximating the continuous thrust to a series of impulsive burns where different sets of low-thrust design parameters each result in a unique family of transfer arcs. Similarly, Genta and Maffione [23] solve the optimal control problem via the Euler-Lagrange method while assuming a departure from a 800km altitude circular orbit around the Earth. A variable specific impulse engine, where the specific impulse is also an optimized variable, is mainly investigated. Both methods produce contour plots that illustrate the overall costs of the Earth-to-Mars transfer trajectories over a range of departure and arrival epochs, i.e., the plots effectively characterize the heliocentric leg.

The current work expands on these existing methods by computing the optimal transfer trajectories via the direct collocation algorithm (Chapter 3) and produces an analogous contour plot. The setup of the optimization problem as well as the corresponding assumptions

are introduced. Two strategies to generate an initial guess for the direct collocation algorithm are presented, followed by the resulting contour plot.

4.1 Problem Formulation

To characterize the heliocentric leg, a set of simplifying assumptions are introduced to avoid the complexity from the perturbations from multi-body dynamics as well as the planetocentric arcs around the Earth and Mars [23], [38]. The assumptions utilized in the current investigation are as follows:

1. The Sun-2BP is utilized as the dynamical model for the heliocentric leg, i.e., gravity from other celestial bodies is ignored.

2. For a given pair of departure and arrival epochs, the boundary constraints of the heliocentric leg are set as the states of the planets in heliocentric space.

The first assumption implies that at both end states of the heliocentric leg, the spacecraft has effectively escaped the gravity of the planets and only the Sun's gravity needs to be considered for the leg. The second assumption is also denoted rendezvous constraint [23], [38], as the states of the spacecraft coincide with those of the planets in the heliocentric space at the end points. While the results in the current chapter are bound to these assumptions, they are validated in the higher-fidelity ephemeris model in Chapter 6.

To generate a contour plot over different pairs of the epochs, an optimal control problem is formulated for each pair of epochs. The time of flight, $T\tilde{O}F$, of the leg is fixed to be the difference between the provided dates,

$$T\tilde{O}F = JD_A - JD_D, \tag{4.1}$$

where JD_D and JD_A correspond to the Julian dates of the departure and arrival epochs, respectively. Then, the boundary states of the legs are fixed as the states of the Earth

and Mars in the heliocentric space, retrieved from the ephemerides file. In the Cartesian coordinate, the states are written as,

$$\tilde{\boldsymbol{X}}_{Earth,Cart} = \begin{bmatrix} \tilde{X}_{Earth} & \tilde{Y}_{Earth} & \tilde{Z}_{Earth} & \tilde{V}_{X,Earth} & \tilde{V}_{Y,Earth} & \tilde{V}_{Z,Earth} \end{bmatrix}^T \tag{4.2}$$

$$\tilde{\boldsymbol{X}}_{Mars,Cart} = \begin{bmatrix} \tilde{X}_{Mars} & \tilde{Y}_{Mars} & \tilde{Z}_{Mars} & \tilde{V}_{X,Mars} & \tilde{V}_{Y,Mars} & \tilde{V}_{Z,Mars} \end{bmatrix}^T, \tag{4.3}$$

where the tilde accent refers to the dimensional quantities. Each element of these vectors corresponds to the position and inertial velocity component in the Sun-centered ECLIPJ2000 frame. For example, the position vector of the Earth is represented as,

$$\tilde{\boldsymbol{R}}_{Earth} = \tilde{X}_{Earth}\hat{X}_{EJ} + \tilde{Y}_{Earth}\hat{Y}_{EJ} + \tilde{Z}_{Earth}\hat{Z}_{EJ}, \tag{4.4}$$

where the unit vectors correspond to the directions in the ECLIPJ2000 frame. Similarly, the velocity of the Earth is represented as,

$$\tilde{\boldsymbol{V}}_{Earth} = \frac{{}^{I}d\tilde{\boldsymbol{R}}_{Earth}}{d\tilde{t}} = \tilde{V}_{X,Earth}\hat{X}_{EJ} + \tilde{V}_{Y,Earth}\hat{Y}_{EJ} + \tilde{V}_{Z,Earth}\hat{Z}_{EJ}. \tag{4.5}$$

The state of the Earth at JD_D becomes the initial state of the heliocentric leg, and similarly, the state of Mars at JD_A is set as the final state of the leg.

Next, the transfer trajectory is discretized into multiple segments to formulate an optimization problem suitable for the direct collocation algorithm. While the number of segments affect the computation time and also the optimality of the solution, 40 segments are employed, a number consistent with a previous work [69]. The segments are placed by equally dividing the given time of flight. Thus, the mesh of the direct collocation algorithm is constructed as,

$$\tilde{\Pi} = \tilde{t}_1 < \tilde{t}_2 < \cdots < \tilde{t}_{40} < \tilde{t}_{41}, \tag{4.6}$$

where the length of each segment is constant as,

$$\tilde{t}_{\mathrm{i}+1} - \tilde{t}_{\mathrm{i}} = \frac{T\tilde{O}F}{40} (\mathrm{i} \leq \mathrm{i} \leq 40). \tag{4.7}$$

Then, the direct collocation algorithm searches for the design vector $\boldsymbol{X}(Equation(3.74))thatsatisfiesthecon$ corresponds to the mass of the spacecraft at the last node of the 40th segment, or the final mass.

This process of setting and solving an optimization problem is repeated over a grid of the departure epochs and the time of flight. For the departure epochs, or JD_D, 2000 days starting from 01/01/2024, are sampled with a 10-day increment. The arrival epochs are selected such that the time of flight from each departure epoch spans between 900 and 100 days by a 10-day decrement. For example, for the departure epoch of 01/01/2024, the arrival epoch is selected to be between 06/19/2026 ($T\tilde{O}F = 900$ days) and 04/10/2024 ($T\tilde{O}F = 100$ days), equally spaced by 10 days. The steps to compute the optimal transfer arc corresponding to each point of the grid are provided in Algorithm 1, which consists of two iteration loops. The outer loop corresponds to the iteration on the departure epoch, JD_D. The inner loop iterates on the $T\tilde{O}F$ value, starting from 900 days and gradually decreasing until $T\tilde{O}F = 100$ days. Within each iteration of the inner loop, an initial guess is formed and passed to the optimizer to result in a propellant optimal trajectory for the departure epoch and $T\tilde{O}F$ pair. If the direct collocation algorithm fails to converge, it is considered that the $T\tilde{O}F$ is too short to allow for a feasible trajectory to exist for the given departure epoch, and the algorithm proceeds to the next iteration of the outer loop.

Algorithm 1 Sun-2B Propellant Optimal Solution

```
for Every departure epoch do
    for TÕF = 900, 890, 880, ..., 100 (days) do
        if TÕF == 900 (days) then
            Initial guess from the polynomial approximation
        else
            Initial guess from the continuation
        end if
        Optimize J_o via direct collocation
        if Fails to converge then
            Break
        end if
    end for
end for
```

4.2 Initial Guess

Obtaining an optimal trajectory for each pair of the epochs requires a suitable initial guess (Figure 3.1). Two different strategies, (1) polynomial approximation and (2) continuation, are provided to generate an initial guess for the heliocentric leg. The inner loop of Algorithm 1 iterates on the time of flight that starts from 900 days and gradually decreases. For the maximum value, 900 days, a third degree polynomial approximation is utilized to generate an initial guess, and for the rest of the iteration within the inner loop, previously converged solution is utilized as the initial guess.

4.2.1 Third Degree Polynomial Approximation

An approximate solution of the heliocentric leg is formed as a third degree polynomial function of time to serve as an initial guess. The known data points of the function are the states of the planets corresponding to the departure and arrival epochs, which are also the boundary constraints of the optimization problem. For the polynomial fitting, it is advantageous to transition the Cartesian state vectors, Equations (4.2) and (4.3), to the vectors in the cylindrical coordinate frame. The position and velocity components in the $\hat{Z}_{EJ}$ direction stay constant in both coordinate frames, whereas the rest of the components are transformed via the following equations,

$$\tilde{R}_{XY} = \tilde{X}^2 + \tilde{Y}^2 \tag{4.8}$$

$$\phi = \tan_2^{-1} \frac{\tilde{Y}}{\tilde{X}} \tag{4.9}$$

$$\frac{d\tilde{R}_{XY}}{d\tilde{t}} = \tilde{V}_{R_{XY}} = \frac{\tilde{X}\tilde{V}_X + \tilde{Y}\tilde{V}_Y}{\tilde{R}_{XY}} \tag{4.10}$$

$$\frac{d\phi}{d\tilde{t}} = \tilde{V}_\phi = \frac{\tilde{X}\tilde{V}_Y - \tilde{Y}\tilde{V}_X}{\tilde{R}_{XY}^2} \tag{4.11}$$

where $\tan_2^{-1}$ is a four quadrant arctangent. Then, the states of the planets are re-written in the cylindrical coordinate frame as,

$$\tilde{\boldsymbol{X}}_{Earth,Cyl} = \begin{bmatrix} \tilde{R}_{XY,Earth} & \phi_{Earth} & \tilde{Z}_{Earth} & \tilde{V}_{R_{XY},Earth} & \tilde{V}_{\phi,Earth} & \tilde{V}_{Z,Earth} \end{bmatrix}^T \tag{4.12}$$

$$\tilde{\boldsymbol{X}}_{Mars,Cyl} = \begin{bmatrix} \tilde{R}_{XY,Mars} & \phi_{Mars} & \tilde{Z}_{Mars} & \tilde{V}_{R_{XY},Mars} & \tilde{V}_{\phi,Mars} & \tilde{V}_{Z,Mars} \end{bmatrix}^T. \tag{4.13}$$

These vectors are considered as the boundary constraints that the approximated polynomial function must satisfy. For example, $\tilde{R}_{XY,Earth}, \tilde{V}_{R_{XY},Earth}, \tilde{R}_{XY,Mars}, \tilde{V}_{R_{XY},Mars}$ correspond to the values and the time derivatives of the variable $\tilde{R}_{XY}$ at the departure and arrival epochs. Any approximated polynomial function for $\tilde{R}_{XY}$ between the two planets must satisfy these four boundary constraints. Since a third degree polynomial is associated with four coefficients, the four boundary conditions for each variable uniquely determine the polynomial function. Consider a third degree polynomial function for $\tilde{R}_{XY}$,

$$p_{R_{XY}}(\tau_p) = C_0 + C_1\tau_p + C_2\tau_p^2 + C_3\tau_p^3, \tag{4.14}$$

where C_0, C_1, C_2, and C_3 denote the four unknown coefficients of the polynomial, and τ_p corresponds to the nondimensional time computed as,

$$\tau_p = 2\frac{\tilde{t} - \tilde{t}_1}{T\tilde{O}F} - 1, \tag{4.15}$$

where $\tilde{t}_1$ corresponds to the first boundary point of the mesh from Equation (4.6), and τ_p is defined between -1 and 1 that correspond to the initial and final times, respectively. Enforcing the boundary constraints to the polynomial function results in the following equations,

$$p_{R_{XY}}(1) = C_0 + C_1 + C_2 + C_3 = \tilde{R}_{XY,Earth} \tag{4.16}$$

$$p_{R_{XY}}(-1) = C_0 - C_1 + C_2 - C_3 = \tilde{R}_{XY,Mars} \tag{4.17}$$

$$\frac{dp_{R_{XY}}}{d\tau_p}|_1 = C_1 + 2C_2 + 3C_3 = \tilde{V}_{R_{XY},Earth} \tag{4.18}$$

$$\frac{dp_{R_{XY}}}{d\tau_p}|_{-1} = C_1 - 2C_2 + 3C_3 = \tilde{V}_{R_{XY},Mars}, \tag{4.19}$$

which are interchangeably represented with the following matrix equation,

$$\begin{bmatrix} C_0 \\ C_1 \\ C_2 \\ C_3 \end{bmatrix} = \begin{bmatrix} 1 & 1 & 1 & 1 \\ 1 & -1 & 1 & -1 \\ 0 & 1 & 2 & 3 \\ 0 & 1 & -2 & 3 \end{bmatrix}^{-1} \begin{bmatrix} \tilde{R}_{XY,Earth} \\ \tilde{R}_{XY,Mars} \\ \tilde{V}_{R_{XY},Earth} \\ \tilde{V}_{R_{XY},Mars} \end{bmatrix}. \tag{4.20}$$

The same process is repeated for the other two variables to construct three different third degree polynomial functions that together approximate the transfer trajectory between the planets given the epochs. It is noted that other formulations of the polynomial approximation are available too. Patel et al. [70] introduce an algorithm where Chebyshev polynomials of higher degrees are utilized to compute a feasible Earth-to-Mars heliocentric trajectories. In this investigation, it is discovered that a third degree polynomial already works properly as an initial guess for the direct collocation algorithm, and higher order polynomial functions are not considered.

To illustrate the steps of generating an initial guess, consider a departure from the Earth on 01/01/2024, and arrival at Mars after 900 days, or on 06/19/2026. The initial and final Cartesian states of the planets in the Sun-centered ECLIPJ2000 are retrieved as,

$$\tilde{\boldsymbol{X}}_{Earth,Cart} = \begin{bmatrix} -2.4811 \times 10^{7} km \\ 1.4499 \times 10^{8} km \\ -8.2153 \times 10^{3} km \\ -2.9841 \times 10^{1} km/s \\ -5.1263 km/s \\ 1.1842 \times 10^{-3} km/s \end{bmatrix}, \tag{4.21}$$

$$\tilde{\boldsymbol{X}}_{Mars,Cart} = \begin{bmatrix} 1.8761 \times 10^{8} km \\ 1.0247 \times 10^{8} km \\ -2.4529 \times 10^{6} km \\ -1.0687 \times 10^{1} km/s \\ 2.3334 \times 10^{1} km/s \\ 7.5106 \times 10^{-1} km/s \end{bmatrix}, \tag{4.22}$$

where the $\hat{X}_{EJ}$ and $\hat{Y}_{EJ}$ components of the position for the boundary constraints are plotted in Figure 4.1. The dotted lines correspond to the orbits of the planets. The Cartesian vectors

are then transitioned into the cylindrical coordinate frame via Equations (4.8)-(4.9) to result in,

$$\tilde{\boldsymbol{X}}_{Earth,Cyl} = \begin{bmatrix} 1.4710 \times 10^{8} km \\ -4.5429 rad \\ -8.2153 \times 10^{3} km \\ -1.9614 \times 10^{-2} km/s \\ 2.0583 \times 10^{-7} rad/s \\ 1.1842 \times 10^{-3} km/s \end{bmatrix} \tag{4.23}$$

$$\tilde{\boldsymbol{X}}_{Mars,Cyl} = \begin{bmatrix} 2.1378 \times 10^{8} km \\ 4.9992 \times 10^{-1} rad \\ -2.4529 \times 10^{6} km \\ 1.8062 km/s \\ 1.1976 \times 10^{-7} rad/s \\ 7.5106 \times 10^{-1} km/s \end{bmatrix}. \tag{4.24}$$

Then, three third degree polynomials are formed by solving Equation (4.20) for each variable in the cylindrical coordinate frame, $\tilde{R}_{XY}, \phi$ and $\tilde{Z}$. The position history of the computed polynomials in the $\hat{X}_{EJ} - \hat{Y}_{EJ}$ plane is plotted in Figure 4.2. From the polynomial approximations, an initial guess is constructed by first dividing the polynomials over the mesh, $\tilde{\Pi}$. This process is illustrated in Figure 4.3, where the polynomial functions are equally divided into 40 segments that each contains four nodes, plotted as black dots. Although the polynomials are constructed in the cylindrical coordinate frame, the discretized states are transitioned back into the Cartesian coordinate frame to be consistent with the frame utilized in the direct collocation algorithm. Figure 4.3 only illustrates the position components in the $\hat{X}_{EJ}$ and $\hat{Y}_{EJ}$ directions, but the same process is executed for the rest of the components, i.e., the position in the $\hat{Z}_{EJ}$ direction as well as the velocities in all three directions.

While the position and velocity components of the initial guess are readily available from the polynomial approximations, additional steps are required to generate the initial guess for

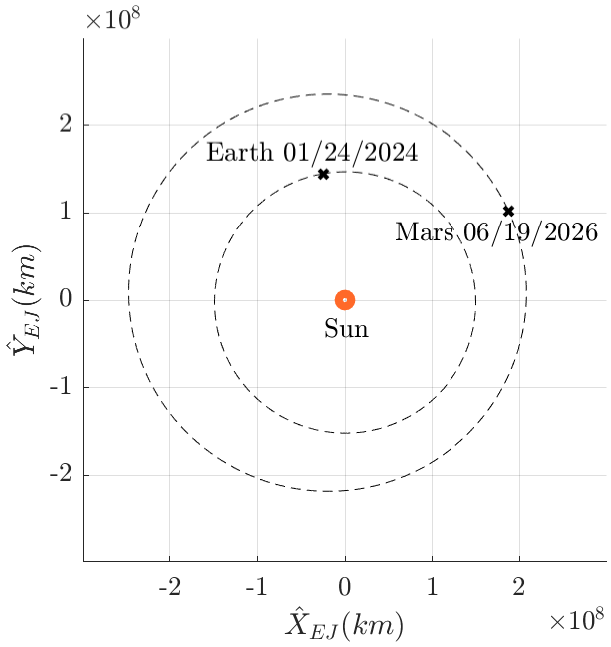

Figure 4.1. The retrieved states in the position space, Sun-centered ECLIPJ2000 frame view

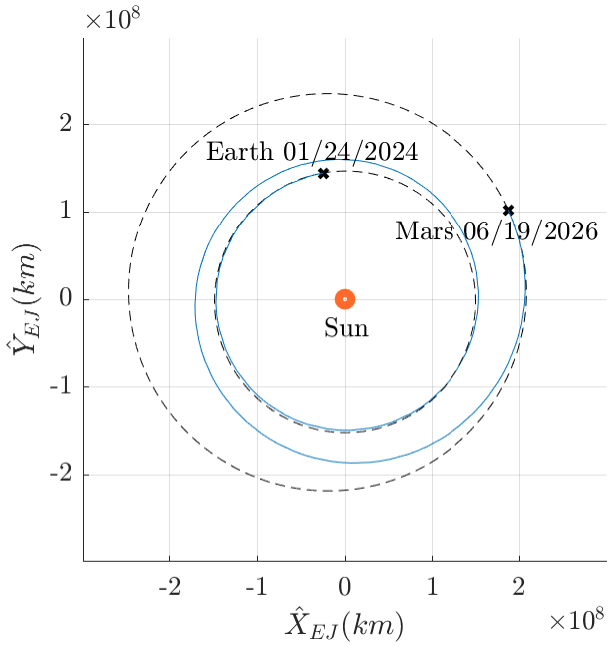

Figure 4.2. Position history of the constructed polynomials

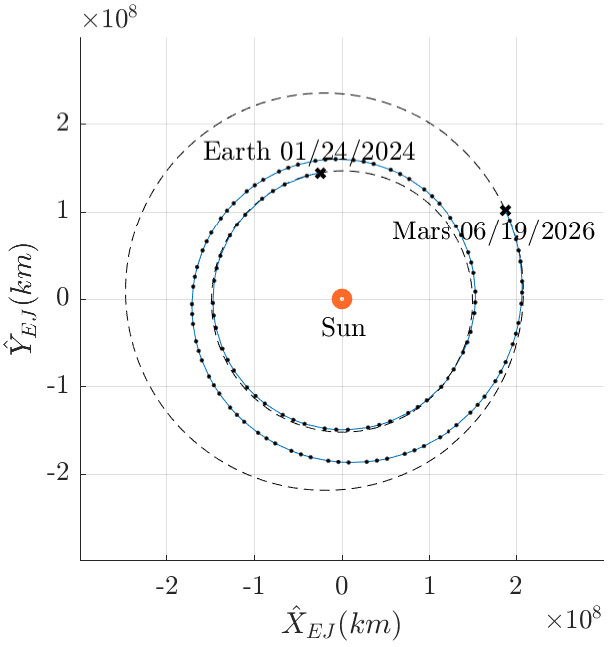

Figure 4.3. Discretized states from the polynomials

the mass and the control. To this end, the spacecraft is assumed to thrust at the maximum available value, that results in a constant decrease of the spacecraft mass, i.e.,

$$\tilde{T} = \tilde{T}_{max} \tag{4.25}$$

$$\tilde{m} = \tilde{m}_0 - \frac{\tilde{T}}{\tilde{g}_0 \tilde{I}_{sp}} \Delta\tilde{t}, \tag{4.26}$$

where $\Delta\tilde{t}$ is the dimensional time since the initial time, $\Delta\tilde{t} = \tilde{t} - \tilde{t}_1$. $\tilde{m}_0$ corresponds to the initial mass of the spacecraft upon the departure of the Phase 2, the heliocentric leg, and is assumed to be 340.9 kg following the assumptions listed in Table 1.1. Then, the values of the mass corresponding to each of 160 nodes are computed and incorporated into the initial guess. While the thrust magnitude is fixed at the maximum value, the direction of the thrust must also be obtained. An error is defined over each segment to be the difference of the velocities between the value from the polynomial approximations and the propagated value utilizing the Sun-2B dynamical model for the segment. Then, the initial guess for the thrust direction is decided to be aligned with the error vector, such that the thrust allows the polynomial approximations to better follow the actual dynamics. Finally, the state and control of the constructed initial guess are nondimensionalized utilizing the Sun-Earth CR3BP characteristic quantities (Table 2.1) to avoid scaling problems during optimization. The initial guess obtained via this process is employed as the input to the direct collocation method to converge to a feasible as well as optimal trajectory, illustrated in Figure 4.4.

4.2.2 Continuation

Recall that the inner loop of Algorithm 1 iterates on the time of flight. When $T\tilde{O}F \neq 900$ days, or when an optimized solution already exists from the previous iteration, it is utilized as the initial guess for the current step. Assume, for example, that an optimal transfer converged from the pair of epochs (01/01/2024, 06/19/2026) is,

$$\boldsymbol{X}_{opt,900} = \arg\min_{\boldsymbol{X}} J_o(\boldsymbol{X}), \tag{4.27}$$

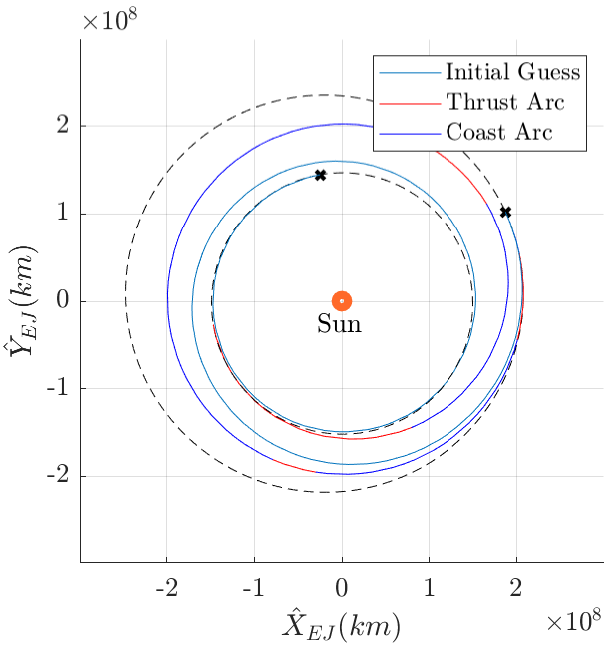

Figure 4.4. The converged optimal trajectory

where the subscript 900 refers to the time of flight of the transfer. Then, the next step of the inner loop iteration solves for the pair of epochs with the same departure date, i.e., 01/01/2024, and the arrival date of 06/09/2026, corresponding to $T\tilde{O}F = 890$ days. The initial guess for this new pair of dates is readily derived from $\boldsymbol{X}_{opt,900}$. The state and the control from the optimal solution are utilized without any change, but the mesh is reconstructed to mirror the decreased total time of flight from 900 days to 890 days. Additionally, the state of Mars corresponding to the new arrival epoch is retrieved again to update the final constraint on the heliocentric leg.

4.3 Results

Based on two strategies for the initial guess generation, Algorithm 1 is run to generate a contour plot, demonstrated in Figure 4.5. The x and y axes correspond to the departure epoch and the time of flight, respectively, and the color scheme describes the level of the propellant consumption. While the colored region corresponds to the points of the grid where the algorithm succeeds in finding an optimal trajectory, the white region indicates where the algorithm fails to converge to a feasible solution. Although smaller steps for the time of flight may be utilized to slightly expand the solutions to the white region, it still corresponds to the end of the family of the heliocentric leg, where a feasible solution stops to exist under the given set of spacecraft parameters, listed in Table 1.2. It is noted that the plot is analogous to the results that appear in the previous literature (Potter et al. [69] Figure 10, Genta and Maffione [23] Fig. 4). The difference originates from the problem formulation, i.e., different launch scenarios from the Earth and different models utilized for the engine.

The contour plots illustrate a general tendency of trade-off between the time of flight and the propellant consumption, where for a given departure epoch, the propellant consumption decreases in exchange for an increased time of flight. It is noted that the propellant consumption decreases asymptotically, i.e., once a certain level of time of flight is reached, the required propellant does not decrease significantly. Three blue triangular shapes are apparent in Figure 4.5, that represent the points of the grid where the required propellant only slowly decreases for an increase in the time of flight, requiring approximately 100 kg of propellant. Although these shapes do not exactly repeat themselves, the patterns do demonstrate peri-

odicity, where the period roughly corresponds to the synodic period of the Earth and Mars, i.e., 780 days. The result are also illustrated with different axes as in Figure 4.6, where the y-axis corresponds to the arrival epoch instead of the time of flight. The discontinuities are apparent in the contour plots, where a small increment in the departure epoch results in a large change in the optimized propellant level. In Figure 4.7(a), two pairs of the initial epoch and the time of flight are selected across the discontinuity. One of the pair, illustrated in Figure 4.7(b), corresponds to the solution where the number of revolutions around the Sun is larger than 1 but smaller than 2, whereas the other pair, plotted in Figure 4.7(c) illustrates the optimal solution with number of revolutions between 2 and 3. The configuration of the planets changes in a time-dependent way, where the Earth rotates more around the Sun compared to Mars for a given length of time. Thus, when departure date is moved forward, at certain epochs, the transfer arcs corresponding to number of revolutions between n and $n+1$ cease to exist, as the configuration of the planets does not allow such transfer trajectories. Then, the new family of solutions emerge, corresponding to number of revolutions between $n+1$ and $n+2$. This discontinuity is also observed and discussed in Potter et al. [69]. Thus, Figure 4.5 contains four different families, differentiated by the three discontinuities where the color shifts dramatically over departure epochs. Except for these discontinuities, the propellant consumption over different pairs of epochs change continuously.

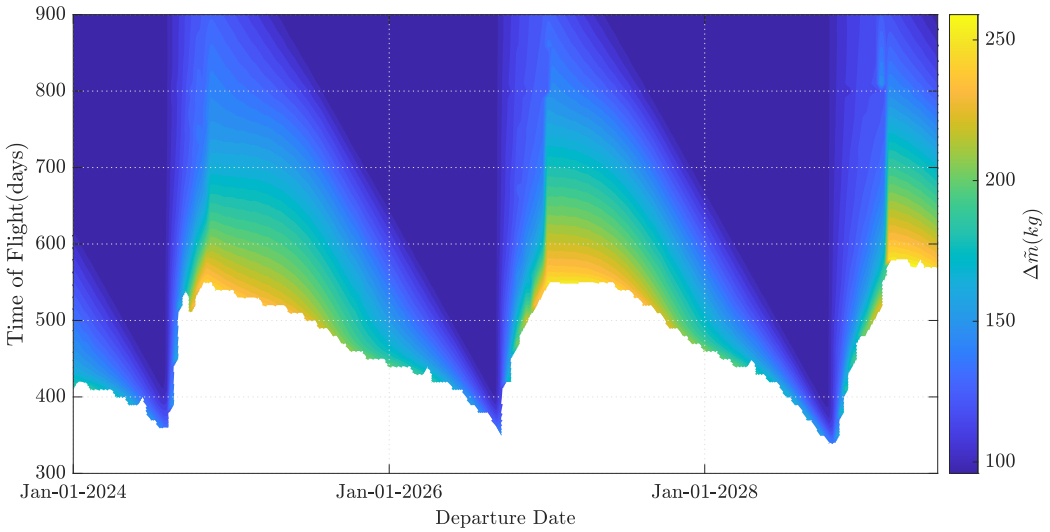

Figure 4.5. The contour plot of the propellant optimal transfers between the Earth and Mars

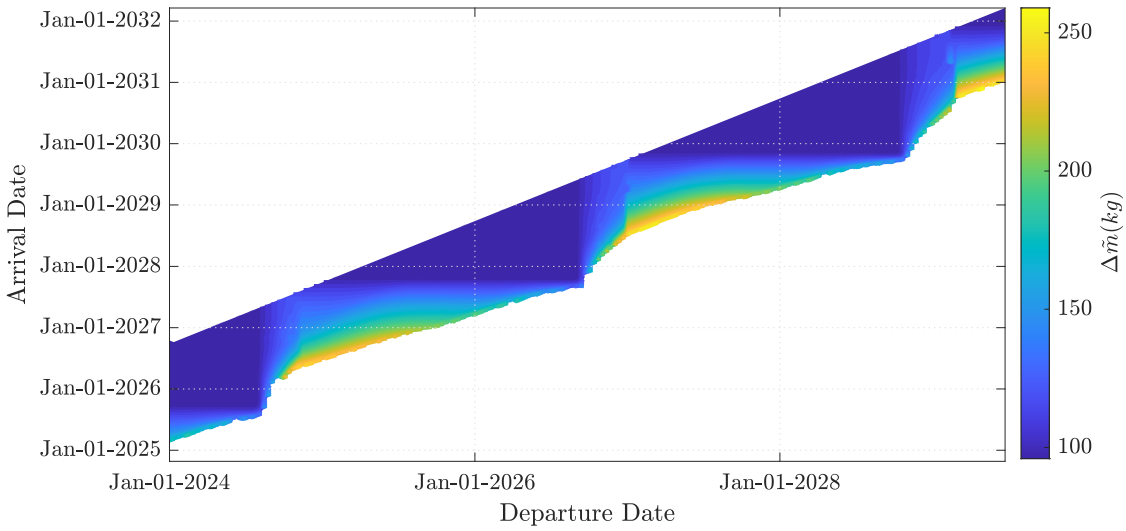

Figure 4.6. The contour plot with the arrival date for the y-axis

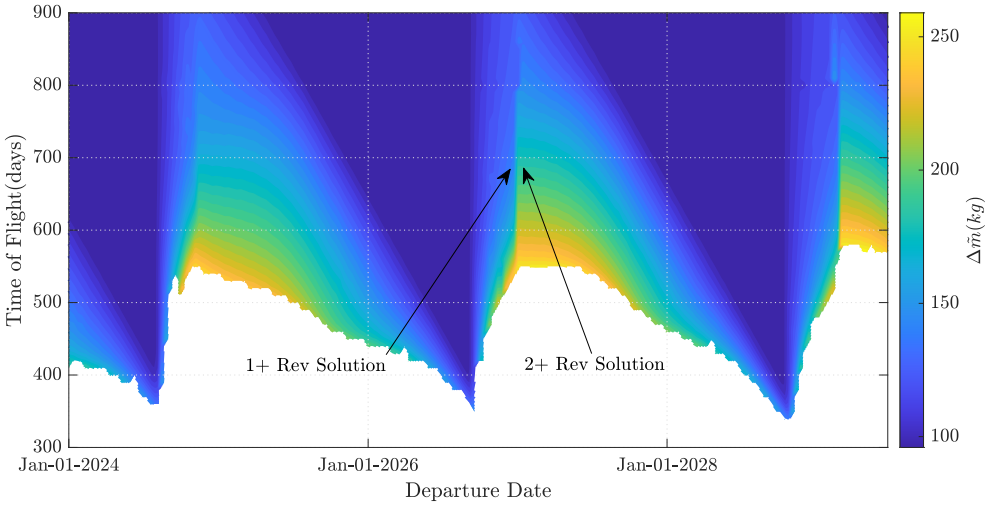

(a) Selected pairs to illustrate the discontinuity of the families

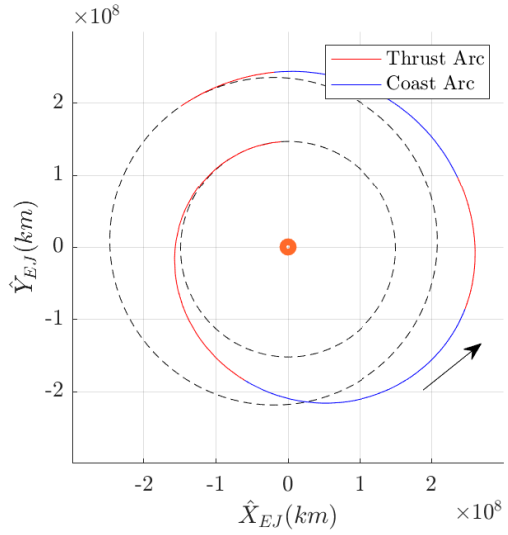

(b) Solution corresponding to revolutions larger than 1 but smaller than 2

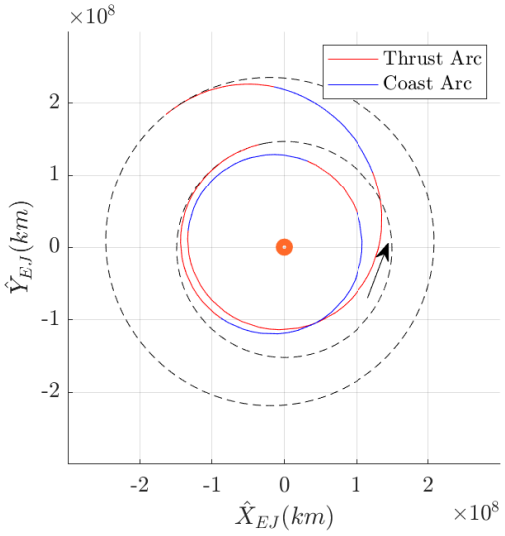

(c) Solution corresponding to revolutions larger than 2 but smaller than 3

Figure 4.7. Discontinuity between the optimal transfer families

5. MARTIAN MOONS TOUR DESIGN

Recall that the overarching goal of the current investigation is to develop a framework for designing low-thrust trajectory that includes the observation of both Martian moons, or *tour* of Martian moons. This concept of sequentially approaching different moons of the planets has been investigated by previous authors over different planetary systems. For the Saturnian system, a successful mission, Cassini-Huygens [71] visited a number of Saturnian moons via flybys. And Jupiter has been a popular location as the proving ground of the tour concept, as the masses of Jovian moons are relatively large with respect to the mass of Jupiter compared to the other planetary systems, that aids fuel-efficient transfer between the moons by enabling low-energy trajectories. Including a seminal work by Ross et al. [72], missions have been proposed to for Jovian moons tour, including JIMO [73] and JUICE [74] missions, proposed by National Aeronautics and Space Administration (NASA) and European Space Agency (ESA), respectively. Finally, research on the tour of the Martian system has been conducted as well, including the work by Derz et al. [44], and an active project by Japan Aerospace Exploration Agency (JAXA), MMX [13].

While the tour of moons of a planet is indeed an appealing oppotunity, providing an "all-in-one" option to explore multiple moons with a single spacecraft, it poses additional challenges. Apart from the systems requirement from the prolonged mission duration from exploring multiple moons, it is associated with problems that are related to the trajectory design as well. The most apparent problem is that the tour concept requires a rendezvous; when the spacecraft departs from a moon and arrives at another, the other moon must be collocated with the spacecraft and results in a phasing issue. For the impulsive engine, while the well-known Hohmann transfer [63] can be used as an approximate solution to the problem, it assumes that the initial and final orbits of the moons are coplanar as well as circular, and it neglects the gravity from the departure and arrival moons.

These assumptions may limit the accuracy of the approximate solution, as the orbital data of the Martian moons indicate that they reside in different orbital planes, as apparent from Table 5.1, where the orbital elements are computed in the MARSIAU frame. It is also noted that both moons have negligible eccentricities compared to other celestial bodies, for

examples, Earth (0.017) and Mars (0.093) around the Sun. And although the masses of Phobos and Deimos are negligible compared to that of Mars (Table 2.1), they still affect the trajectories in the vicinity of the moons. Previous authors have investigated methods that remove some of the simplifying assumptions to facilitate a realistic analysis. One of the proposed strategy is to utilize coupled CR3BP between the planet-departure moon CR3BP and the planet-arrival moon CR3BP [75]-[76]. Then, the dynamical structures from the CR3BP as well as the Poincaré section technique are utilized to find the connections between two moons. However, the moons are still assumed to be in the same plane, and the relative phasing issue remains. More recently, Canales et al. [77] introduces a necessary condition that need be satisfied for a single-burn transfer trajectory to exist between two moons, considering the real orbital planes of the moons as well as the relative phase.

Table 5.1. Orbital data of Phobos and Deimos around Mars (recreated from Canales et al. [78] Table 1)

	a_K [km]	Period [hour]	e_K [nd]	i_K [°]	Ω_K [°]	Radius [km]
Phobos	9,377.82	7.65	0.01482	1.05	131.71	11.2
Deimos	23,459.61	30.29	0.00019	2.44	260.12	6.2

The strategies from these previous investigations cannot be applied directly to the low-thrust trajectory design, as they require an impulsive burn, or a significantly large but instantaneous change in the velocities. A low-thrust engine typically requires longer time of thrust to provide the same amount of change in velocity compared to an impulsive engine, and results in a many-revolution trajectories [46], i.e., spiral trajectories. As the thrust is modeled as a continuous variable, it results in an optimal control problem, where the direction and magnitude of the thrust at each instant must be provided to produce the transfer trajectories between the moons. Thus, the low-thrust engine model compounds the tour design problem with a larger size of the problem consisting of many revolutions of arc around the planet, for which the continuous thrust direction and magnitude must be found to generate a feasible or an optimal solution. The assumptions regarding the low-thrust trajectory design of the Martian tour are introduced, followed by the explanation of the selected strategies to tackle the challenges associated with the low-thrust engine model. Utilizing these strategies, tour trajectories are generated and the corresponding results, including the transfer geometry

as well as the costs, are presented. It is noted that the remaining part of this chapter is a restatement of and an augmentation to the work by Canales et al. [78].

5.1 Structure of Tour of the Martian Moons

As there exist an infinite number of possible routes to explore both moons using a low-thrust engine, simplifying assumptions are introduced. After an analysis of the energy history of a low-thrust trajectory corresponding to a potential Martian tour mission, the sequence of the mission is fixed to be first exploring Deimos and then Phobos. The tour trajectory is divided into two types of arcs: the first type that approaches the Deimos science orbit from heliocentric space (Phase 3), and the second type that connects the Deimos science orbit to the Phobos science orbit (Phase 4). The options for science orbits for both moons are defined, that provide either capture or flyby opportunities of the moons.

5.1.1 Jacobi Constant History from the Heliocentric Leg

Due to the small masses of the Martian moons, the Sun and Mars mainly govern the dynamics of the vicinity of Mars (Table 2.1, Figure 2.3(e)). If the Sun-Mars CR3BP is employed for the preliminary analysis, the JC_{SM}, or the Jacobi constant in the system efficiently captures the energy variation of the spacecraft states in the vicinity of the Martian system. It is noted that a greater JC_{SM} indicates less energy in the Sun-Mars CR3BP system, and vice a versa. The Earth, Phobos and Deimos's states in the Sun-Mars CR3BP rotating frame possess the Jacobi constants included in Table 5.2, where the second column illustrates the difference from the Jacobi constant of Sun-Mars L_1. Note that the Jacobi constants of the Earth and the moons depend on the epoch. The states of the bodies are retrieved from the ephemerides over one year for $10,000$ equally spaced points in time, and then the states are rotated into the Sun-Mars CR3BP rotating frame to compute the mean JC_{SM} of the bodies over this period. While Mars-2BP energy can be utilized to compare the energy levels of the moons, JC_{SM} offers an opportunity to consider the energy of the Earth as well as the Sun-Mars libration points, L_1 and L_2. It is noted that JC_{SM} and the Mars-2BP energy follow similar trends for the orbits associated with the energy levels of the moons, and both

energy quantities are used interchangeably. This investigation utilizes JC_{SM} for a consistent analysis.

Four energy levels corresponding to the Earth, $JC_{SM,Earth}$, one exemplary energy level above JC_{SM,L_2}, $JC_{SM} = 3.00020000$, and the moons, $JC_{SM,Deimos}$ and $JC_{SM,Phobos}$ are illustrated in Figure 5.1. The plotted zero velocity curves and the forbidden regions indicate the required variations in energy of the state along a transfer trajectory from the Earth to Mars. If a spacecraft approaches the Martian system from the Earth through a low-energy trajectory discussed in Chapter 4, the energy level of the spacecraft state upon departure can be roughly estimated to be the Jacobi constant of the Earth, $JC_{SM,Earth}$. At this level of energy, the spacecraft cannot reach the Martian system, as the L_1 gateway is blocked by the forbidden region as it is apparent from Figure 5.1(a), i.e., the energy is insufficient. The blue dotted line corresponds to the Earth's orbit over a year starting from Jan 01, 2022, viewed in the Sun-Mars CR3BP rotating frame. The energy level of the spacecraft must be raised until it is high enough to open the L_1 gateway. Figure 5.1(b) and 5.1(c) illustrate the energy level corresponding to $JC_{SM} = 3.00020000$, or when the gateways are open both at L_1 and L_2. Then, the energy must be lowered again until Mars captures the spacecraft, and the spacecraft enters an orbit around Mars that offers access to the Martian moons. Figure 5.1(d)-5.1(g) illustrate the energy levels corresponding to Deimos and Phobos. It is noted that the views in Figure 5.1(d) and 5.1(f) do not effectively demonstrate the size of the Deimos and Phobos's orbits, and are zoomed-in further as in Figure 5.1(e) and 5.1(g); a significant amount of energy must changed to close the L_1 gateway and force the spacecraft to be captured by Mars.

Table 5.2. Jacobi constants in the Sun-Mars CR3BP: Sun-Mars L_1, L_2, Phobos, and Deimos

	JC_{SM}	$JC_{SM} - JC_{L_{1,SM}}$
L_1	3.00020249	0
L_2	3.00020206	$\approx -4e-7$
Earth	3.11977074	$\approx 1e-1$
Phobos	3.00745257	$\approx 7e-3$
Deimos	3.00298702	$\approx 3e-3$

Since the energy level of Phobos is lower than that of Deimos, it is straightforward to first explore Deimos and then transfer to Phobos from the low-thrust engine perspective; the energy can only be changed in a continuous manner, and it is more efficient to visit Deimos before finally lowering the energy until the level of Phobos. Previous investigations also assume the sequence from the outer moons to the inner moons, for the Jovian system [73] and the Martian system [44]. Note that the reverse sequence may be considered efficient only when the spacecraft first arrives at a highly elliptic orbit around Mars that offers Phobos flybys, then the maneuver may be employed to transfer to Deimos science orbits. However, it is also noted that the eccentricity of the moons are negligibly small, implying that the capture orbits around the moons possess similar level of eccentricity. And any attempts to utilize highly eccentric orbits may increase the propellant consumption associated with the transfers from these eccentric orbits to nearly circular capture orbits around the moons. For this reason, current analysis focuses on the sequence that is based on the energy order.

5.1.2 Science Orbit Definition

Figure 5.2 illustrates the tour concept and sequence investigated in the current work. As a low-thrust engine requires a significantly long time to achieve the energy change, it requires spiral-down trajectories, demonstrated as black and purple arcs in Figure 5.2(a). These spiral-down arcs are divided into two types to facilitate analysis. The first type of trajectory, labeled spiral-down (A), is required to close the energy gap between the incoming heliocentric leg that is associated with greater energy than Sun-Mars L_1, and the Deimos science orbit. This arc corresponds to the Phase 3 of the multi-phase formulation of the current investigation, illustrated in Figure 1.1. Then the second type of spiral-down arc, spiral-down (B), is employed to transfer from the Deimos science orbit to the Phobos science orbit. Spiral-down (B) corresponds to the Phase 4 of the multi-phase formulation, described in Figure 1.1. The sequence is also labeled in Figure 5.2(b) with the associated chapters. While the tour sequence is fixed, there exist multiple options to explore both moons. Hence, it is necessary to define the science orbits for both moons, and they are categorized into two options: (1) capture and (2) flyby.

As the masses of the Martian moons are small compared to that of Mars, it is necessary to include both Mars and moons to the dynamical models to describe the motion of the spacecraft that is captured by the moons. As Phobos has been considered as a primary target for a number of previously proposed missions, the motion of spacecraft in the vicinity of Phobos, or the capture orbit around Phobos, is investigated by a number of authors who include the gravity from both Mars and Phobos. Chen et al. [79] as well as Wallace et al. [80] utilize the Mars-Phobos CR3BP, where the retrograde orbits around Phobos are computed. Other authors, including Zamaro et al. [81] and Wang et al. [82], investigated higher-fidelity models by utilizing Mars-Phobos elliptic restricted three body problem to account for the eccentricity of Phobos and to incorporate the irregular gravitational field of Phobos. As these previous works prove that both Phobos and Mars gravity must be included to facilitate transition to higher-fidelity model, the Mars-Phobos CR3BP and the Mars-Deimos CR3BP are considered for the capture orbits around Phobos and Deimos, respectively. More specifically, Lyapunov orbits around Mars-Phobos L_2 and Mars-Deimos

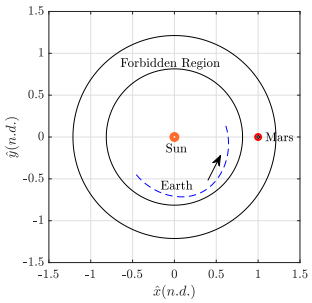

(a) $JC_{SM} = JC_{SM,Earth}$

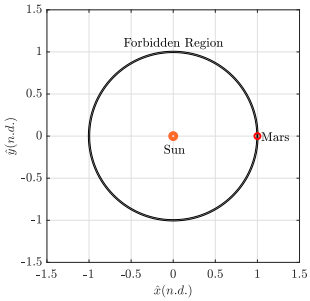

(b) $JC_{SM} = 3.00020000 < JC_{SM,2}$

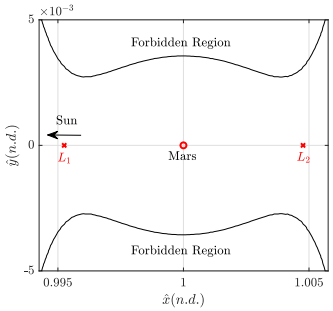

(c) $JC_{SM} = 3.00020000 < JC_{SM,2}$ zoomed-in

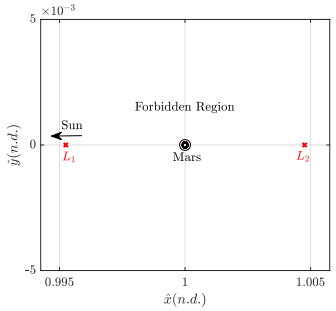

(d) $JC_{SM} = JC_{SM,Deimos}$ zoomed-in

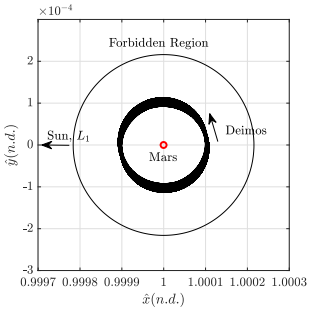

(e) $JC_{SM} = JC_{SM,Deimos}$ further zoomed-in

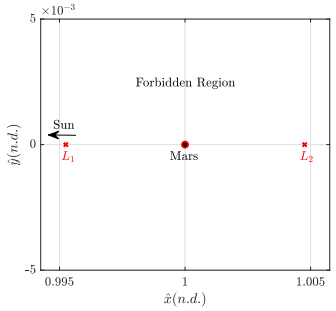

(f) $JC_{SM} = JC_{SM,Phobos}$ zoomed-in

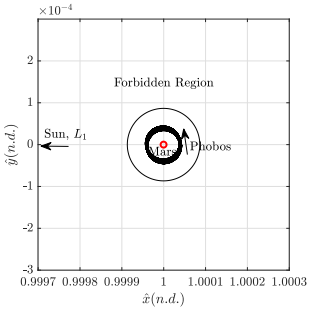

(g) $JC_{SM} = JC_{SM,Deimos}$ further zoomed-in

Figure 5.1. Zero velocity surface and the forbidden region corresponding to different energy levels

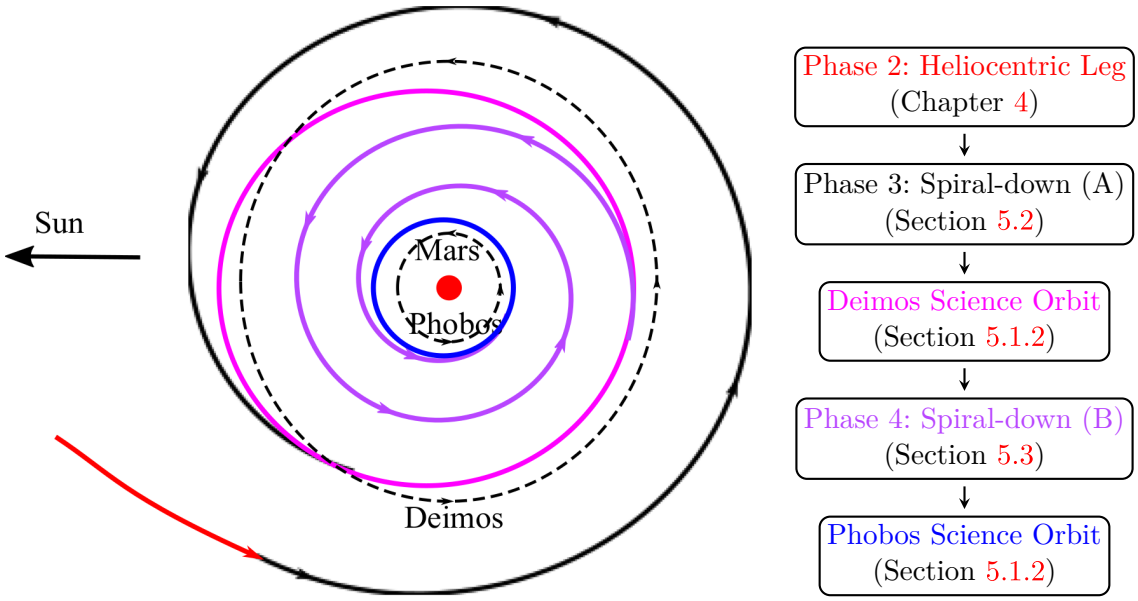

(a) Tour schematic (recreated from Canales et al. [78], Figure 11)

(b) Labels and relevant sections

Figure 5.2. Sequence of a Martian tour with a low-thrust engine

L_1 are considered. Note that it is still assumed that Deimos and Phobos are centrobaric; the irregular shapes of the moons are not considered in the current investigation.

For the Phobos capture option, libration point orbits around the Mars-Phobos L_2 are considered. Figures 5.3(a) and 5.3(b) illustrate the L_2 Lyapunov and halo orbit families in the Mars-Phobos CR3BP, respectively, plotted in the Mars-Phobos CR3BP rotating frame. The color scheme represents the variation of Jacobi constant of the Mars-Phobos CR3BP, JC_{MP}, along the orbit, where the same color corresponds to the same JC_{MP} for two plots. Even though halo orbits are spatial, the energy level is associated with similar spectrum as the planar, Lyapunov orbit. The energy of these libration point orbits is also investigated in the Sun-Mars CR3BP system with JC_{SM}, as shown in Figure 5.4. For the starting epoch at Jan 1st of 2023, the initial states of the orbits are rotated into the Sun-Mas CR3BP along 1000 equally spaced times for one year and JC_{SM} is computed as the average over the 1000 sampled times. Note that across all members of the both families, the maximum variation in JC_{SM} is less than $5e-5$, two orders smaller than the difference of the Jacobi constant of both moons. This small variation implies that any member of the two families would result in similar results with respect to the associated propellant consumption and time of flight; they represent similar options viewed from the larger scale in the Sun-Mars CR3BP system. For this investigation, the capture orbit is selected to be a member of the family with $JC_{MP} = 3.000023$, illustrated in black arc in Figure 5.3(a). Again, it is emphasized that the results demonstrated in the following sections can be easily extrapolated to any other members of the both families in Figures 5.3(a) and 5.3(b). The initial state of the selected Phobos capture orbit, and period as well as the associated Jacobi constants in relevant CR3BP system are included in Table 5.4.

Next, for the Deimos exploration, the capture option is represented as the Mars-Deimos L_1 orbits in the Mars-Deimos CR3BP. Applying the preceeding reasoning here, it is deduced that any member of the Mars-Deimos L_1 Lyapunov or halo orbit families result in orbits with similar level of energy in the Sun-Mars CR3BP. The selected orbit is associated with the Jacobi constant in Mars-Deimos CR3BP as 3.000005, but the costs obtained with this orbit can be extrapolated to any other members of the same family. The data for the selected Deimos science orbit are provided in Table 5.3.

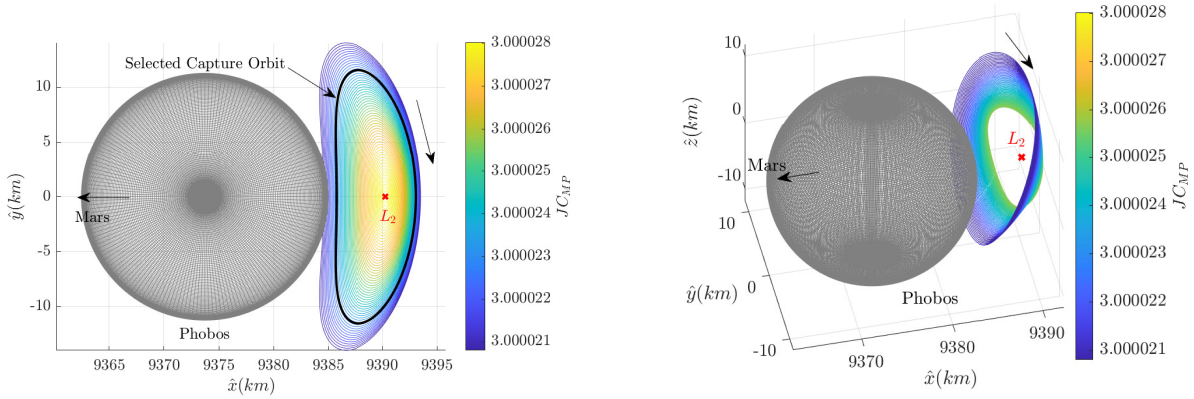

(a) Mars-Phobos L_2 Lyapunov orbit family with the selected capture orbit (Recreated from [78], Figure 6(a))

(b) Mars-Phobos L_2 halo orbit family (Recreated from [78], Figure from [78], Figure 6(b))

Figure 5.3. Mars-Phobos L_2 libration point orbit families: Lyapunov and halo orbit families

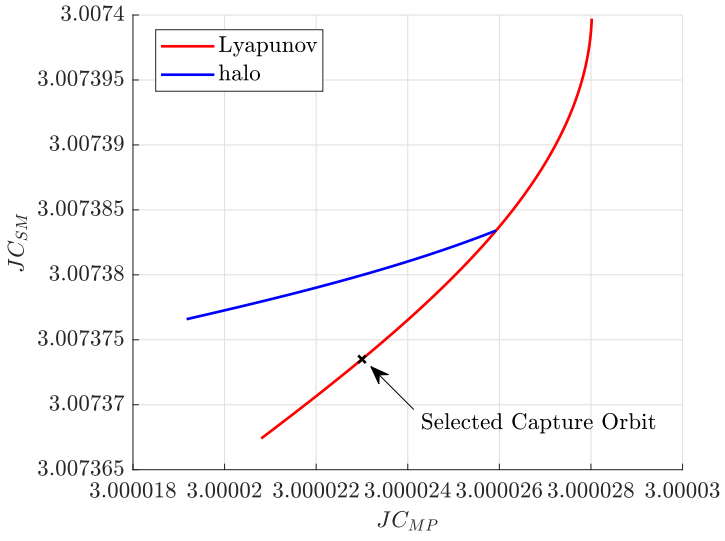

Figure 5.4. JC_{SM} variation of the Mars-Phobos L_2 Lyapunov and halo orbit families

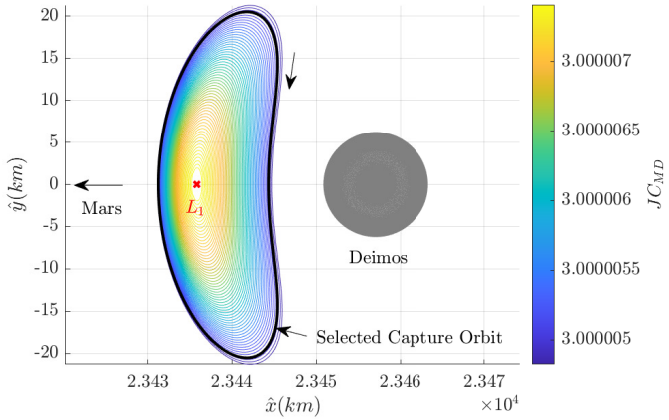

Figure 5.5. Mars-Deimos L_1 Lyapunov orbit family with the selected capture orbit

It is noted that the selected capture orbits are unstable by the Lyapunov criterion, and the spacecraft departs the capture orbits within few revolutions unless stationkeeping maneuvers are employed. However, these capture orbits are utilized as an intermediate science orbits, from which another capture orbit with desired characteristics [83] or landing on the moons [84] is achieved. The current work focuses on the selected capture orbits that are representative of the libration point orbits around Mars-Phobos L_2 and Mars-Deimos L_1.

The other kind of option considered by previous authors is the flyby opportunities enabled by resonant orbits. The resonant orbits are represented with $p : q$ ratio, where p denotes the number of revolutions of the spacecraft around Mars and q denotes the number of revolutions of moons around Mars for the same time. For example, $2 : 1$ Mars-Deimos resonant orbit refers to an orbit that completes two revolutions around Mars while Deimos completes one revolution. Many previously proposed missions include the resonant orbits to obtain flyby opportunities for the moons. The PADME mission [85] proposes repeated flybys of Phobos through Mars-Phobos resonant orbits (MP-ROs) and flybys of Deimos through Mars-Deimos resonant orbits (MD-ROs), where a number of intermediate ΔVs are required to adjust the apoapsis and periapsis of the orbits around Mars. Total of 16 Phobos flybys and 9 Deimos flybys are obtained, where the altitudes of flybys vary from $2km$ to $10km$ for both moons, and the relative velocities vary from $0.946km/s$ to $2.27km/s$ for the Phobos flybys, and $0.643km/s$ to $1.016km/s$ for the Deimos flybys. Gonzales-Franquesa et al. [86] survey a range of MD-ROs that can be potentially utilized for Deimos exploration of the MMX mission. $1 : 1$, $2 : 1$, $3 : 1$, $2 : 3$, $3 : 5$ MD-ROs are analyzed that offer relative velocities between $377m/s$ and $1223m/s$ with the altitudes of flybys ranging from $100km$ to $1000km$. Note that the previous authors focused on the Mars-Deimos resonant orbits computed in the Mars-2B dynamics, where the flybys may not occur at the apsis of the resonant orbits. For the current investigation, resonant orbits that exist in the Mars-Phobos CR3BP and the Mars-Deimos CR3BP are considered for the flyby opportunities. The CR3BP resonant orbits are periodic in the respective CR3BP dynamics models, where the flybys of the moons occur only at one of the apsis. For example, for the CR3BP MP-ROs plotted in Figure 5.6, Phobos flybys occur at the periapsis of the orbit, illustrated in Figure 5.6(b).

Of course, as the spacecraft spends most of the time in a resonant orbit that does not provide science opportunities of a moon except during the flyby, the flyby option provide less science gain compared to the capture option. However, the key concept behind utilizing the flyby orbits is that without strictly matching the energy level of the spacecraft to that of the moon, the spacecraft is nonetheless able to observe the target moon. For example, the investigated capture orbits in Tables 5.4 and 5.3 are associated with closer energy levels measured as JC_{SM}, to the respective moons compared to the flyby orbits. Thus, energy-wise, it is cheaper to employ flyby orbits instead of the capture orbits. Despite the opportunity to gain access to the moons with less adjustment of energy, it is yet associated with a negative factor; the flyby opportunities are obtained essentially by introducing a non-negligible eccentricity to the Mars-centered orbits. For the Phobos flyby orbits, the periapsis of the orbit are fixed at the Phobos radius from Mars, while different levels of eccentricity can be introduced for larger apoapsis and thus greater energy that implies less energy adjustment from the Deimos science orbits. Assuming that the spacecraft departs from the Deimos capture orbit that is associated with negligible eccentricity of the moon itself, the maneuver from a low-thrust engine is required to gradually change the eccentricity of the trajectory to target the value of the Phobos flyby orbit. Thus, a major trade-off exists between the energy, measured as JC_{SM}, and the eccentricity around Mars, in the Mars-2BP system. Although Phobos and Deimos reside in different planes and the low-thrust maneuvers are required to change the inclination and direction of the orbit, it is noted that significant portions of the maneuvers are required to correct the energy, JC_{SM}, and the eccentricity, e_K.

For the Phobos flyby option, the Mars-Phobos resonant orbits in the Mars-Phobos CR3BP are considered. As an infinite number of resonant orbits exist depending on the combination of p and q of the $p : q$ ratio, it is necessary to narrow down to a fewer families of the resonant orbits to facilitate analysis. Considering the sequence of the exploration, i.e., Deimos first and then Phobos, it is reasonable to assume that $p < q$, such that the resonant orbits have bigger energy than Phobos, or a smaller JC_{SM}. Then, a series of resonant orbits are selected so that $p = q - 1$ for $2 \leq q \leq 5$. Although the selected Mars-Phobos resonant orbit families do not represent all possible configuration of the resonant orbit families, they are sufficient to illustrate the relationship between the $p : q$ ratio and the costs associated

with the transfer from the Deimos science orbit to the Phobos science orbit. For a larger p/q ratio, the energy gap from the Deimos science orbit is larger, but the shape of the flyby orbit becomes more circular. Among the selected $1:2$, $2:3$, $3:4$ and $4:5$ MP-RO families, the members that are associated with the flyby altitude of 3.73km are selected and plotted in Figure 5.6. The MP-RO with the largest ratio, $4:5$ corresponds to the option where the flyby orbit is associated with a smaller eccentricity but a larger energy gap from the Deimos science orbit. Vice a versa, $1:2$ represents the option is associated with less energy difference from the Deimos science orbit but also a significant eccentricity. The numbers of the MP-ROs for the energy, JC_{SM}, and the eccentricity, e_K are included in Table 5.4. FA, FV, and OW refer to flyby altitude, flyby velocity, and observation window, respectively. Observation is defined as the radius of Deimos divided by the flyby velocity.

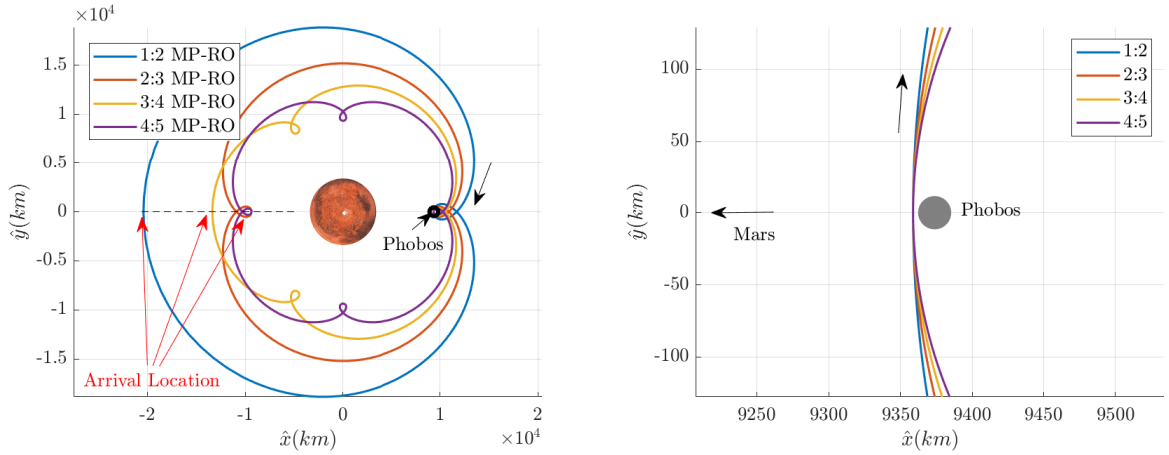

(a) Mars-Phobos rotating frame view

(b) Selected Phobos flyby orbits: zoomed-in view near Phobos

Figure 5.6. Selected Phobos flyby orbits: Mars-Phobos $1:2$, $2:3$, $3:4$, and $4:5$ resonant orbits

The flyby option of Deimos using MD-ROs in the Mars-Deimos CR3BP is extensively investigated by Canales et al. [78], where the candidate resonant orbits are selected among a large number of resonant orbit families depending on the impulsive engine costs associated with the transfer trajectories from the resonant orbits to a Phobos L_2 Lyapunov orbit. This investigation adopts the same members of the previous work that provide Deimos flybys at the altitude of 17.257 km, which is closer compared to the orbits investigated by Gonzales-

Franquesa [86] but is farther than the ones proposed for PADME [11]. The selected three MD-ROs are demonstrated in Figure 5.7, where Figure 5.7(a) illustrates MD-ROs as well as the Phobos's orbit in the Mars-Deimos rotating frame. The zoom-in view near Deimos is plotted in Figure 5.7(b).

Table 5.3. Initial condition, energy, and flyby characteristics of the selected Deimos science orbit

Type	Name	x_0 [n.d.]	y_0 [n.d.]	$\dot{x}_0$ [n.d.]	$\dot{y}_0$ [n.d.]	Period [days]	JC_{MD} [n.d.]	JC_{SM} [n.d.]	e_K [n.d.]	FA [km]	FV [km/s]	OW [s]
Capture	L_1 Lyapunov	0.99945	0	0	−0.00204	0.67	3.00000	3.00301	0.013	-	-	-
Flyby	2:1 MD-RO	1.00100	0	0	−0.36022	1.26	2.87025	3.00473	0.585	17.257	0.4867	12.7
	3:2 MD-RO	1.00100	0	0	−0.17178	2.52	2.9705	3.00391	0.312	17.257	0.2321	26.7
	5:4 MD-RO	1.00100	0	0	−0.08581	5.05	2.9926	3.00346	0.162	17.257	0.115	53.5

Table 5.4. Initial condition, energy, and flyby characteristics of the selected Phobos science orbits

Type	Name	x_0 [n.d.]	y_0 [n.d.]	$\dot{x}_0$ [n.d.]	$\dot{y}_0$ [n.d.]	Period [hours]	JC_{MD} [n.d.]	JC_{SM} [n.d.]	e_K [n.d.]	FA [km]	FV [km/s]	OW [s]
Capture	L_2 Lyapunov	1.001284	0	0	0.002766	3.9	3.00002	3.00737	0.001	-	-	-
Flyby	1:2 MP-RO	0.998400	0	0	0.173515	15.3	2.96992	3.00470	0.403	3.73	0.3709	30.4
	2:3 MP-RO	0.998400	0	0	0.115271	19.8	2.98674	3.00569	0.250	3.73	0.2464	45.7
	3:4 MP-RO	0.998400	0	0	0.086949	25.1	2.99247	3.00615	0.196	3.73	0.1859	60.6
	4:5 MP-RO	0.998400	0	0	0.070127	35.1	2.99511	3.00642	0.128	3.73	0.1499	75.2

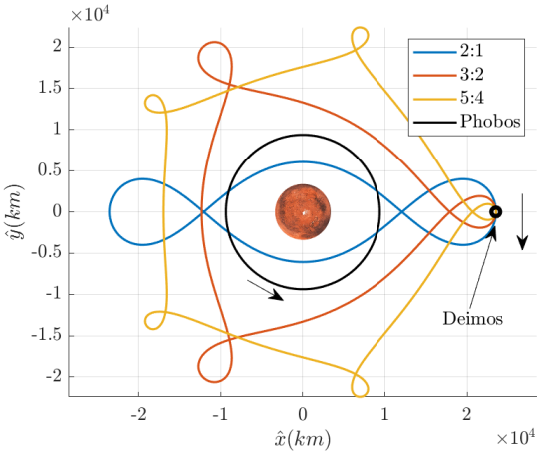

(a) Mars-Deimos rotating frame view

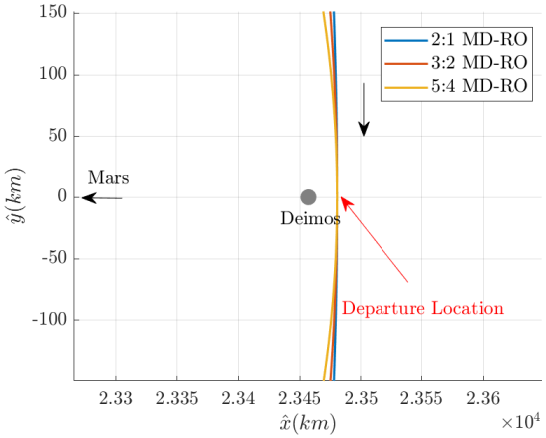

(b) Selected Deimos flyby orbits: zoomed-in view near Deimos (recreated from Canales et al. [78], Figure 5

Figure 5.7. Selected Deimos flyby orbits: Mars-Deimos 2 : 1, 3 : 2, and 5 : 4 resonant orbits

5.2 Phase 3: Spiral-Down (A)

The spiral-down (A) arc connects the incoming heliocentric trajectory to each Deimos science orbit. As the the vicinity of the Martian system is governed by Sun and Mars gravity, the Sun-Mars CR3BP is utilized to compute the first type of arc. Specifically, an anti-velocity steering law in the Sun-Mars CR3BP is employed to generate spiral-down (A), where the s/c is thrusting with the maximum thrust magnitude in the direction opposite to the rotating velocity. Thus, the low-thrust term in Eq. (2.102)-(2.104) is evaluated as follows: $\bar{T} = T\frac{\boldsymbol{v}}{|\boldsymbol{v}|}$, where $\boldsymbol{v}$ denotes the rotating velocity of the s/c in the Sun-Mars CR3BP. This steering law offers a minimum time of flight for a given difference in JC_{SM}, and is a useful reference value for the cost associated with a specified time of flight and propellant consumption, corresponding to arrival at a Deimos science orbit. From each Deimos science orbit, the trajectories are propagated in reverse time with the anti-velocity steering law until the value of the Jacobi constant reaches a threshold value $JC_{SM} = 3.00018 < JC_{SM,L_1} \approx 3.00020$, or when the energy is sufficient to open the L_1 gateway. Although this strategy offers a limited control over the targeted quantity, it can be coupled with a differential corrections scheme to produce feasible and optimized trajectories from the Earth vicinity to connect to the heliocentric leg to generate an end-to-end trajectory. Since back-propagating from the Deimos science orbit assumes that the remaining mass of the spacecraft upon the arrival at the orbit a priori, it is assumed that the remaining mass is $\tilde{m} = 150kg$. It is also assumed that the rest of the engine parameters are $\tilde{T} = 60mN$ and $\tilde{I_{sp}} = 3000s$. This set of parameters are consistent with the numbers defined in Table 1.2, as both sets produce similar levels of maximum thrust.

Figure 5.8 illustrates a low-thrust arc connected to a heliocentric leg that enters the Martian system through the Sun-Mars L_1 gateway, where the arrival state corresponds to $JC_{SM} = 3.00018$, the threshold value. Thus, the anti-velocity steering law provides useful estimates of the costs associated with arriving at the Deimos science orbits given the difference in the energy of the s/c along a heliocentric path and the energy of the s/c in the Deimos science orbits. The corresponding costs, measured as the time of flight and the pro-

pellant consumption for spiral-down (A) are included in Table 5.5. The ΔV corresponds to the equivalent ΔV, computed as,

$$\Delta V = \tilde{I_{sp}} \tilde{g_0} \ln \frac{\tilde{m}_0}{\tilde{m}_0 - \Delta \tilde{m}}, \tag{5.1}$$

where $\tilde{m}_0$ and Δm correspond to the initial mass before the spiral-down (A) arc, and the consumed mass, respectively. The threshold value for JC_{SM} can be adjusted for different set of reference values, but the order of the costs of the spiral-down (A) corresponding to each Deimos science orbit remains the same, as the costs depend heavily on the JC_{SM} of the Deimos science orbit. It is noted that the costs may vary depending on the epoch, since the Deimos science orbit states are defined in the Mars-Deimos CR3BP rotating frame, and should be rotated into the Sun-Mars CR3BP rotating frame in the respective epochs. The costs included in Table 5.5 are computed as the mean value over 365 Earth days, starting from Jan 01, 2022.

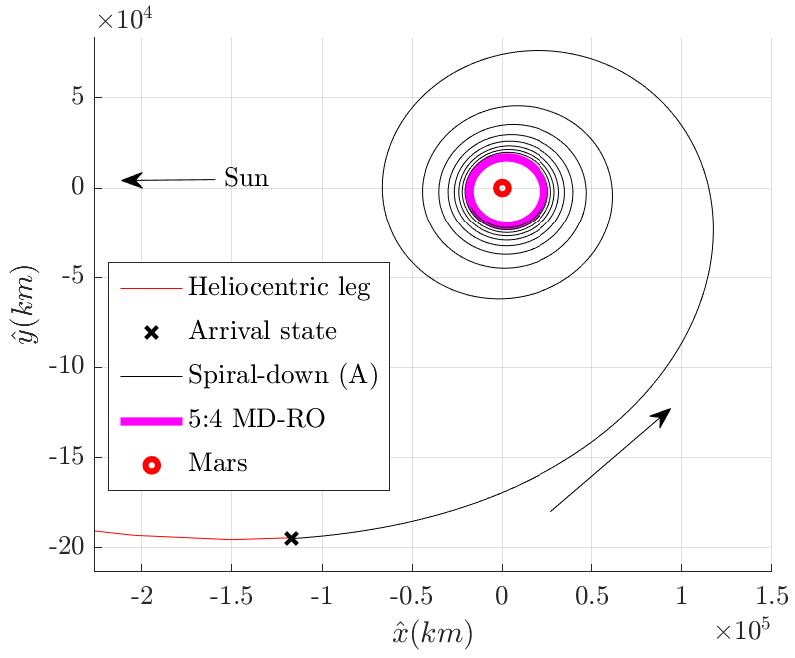

Figure 5.8. Spiral-down (A) example in the Sun-Mars CR3BP rotating frame

5.3 Phase 4: Spiral-Down (B)

Another arc with multiple of revolutions is introduced to connect the Deimos science orbits to the Phobos science orbits, defined as the spiral-down option (B) in Figure 5.2(a). Since all the Deimos science orbits are periodic in the Mars-Deimos CR3BP, the spiral-down (B) is solved independently from the spiral-down (A). A spiral-down (B) arc differ from an (A) arc due to an additional boundary constraint on the final state along the arc that coincides with the state of the Phobos science orbit that is defined in the Mars-Phobos rotating frame. The initial and final states are defined in different rotating frames, i.e., Mars-Deimos CR3BP rotating frame and Mars-Phobos CR3BP rotating frame, respectively, and it may be considered as a rendezvous problem; Phobos should be at the desired location at the end of the spiral-down (B) arc for the spacecraft to arrive at the final state defined in the Mars-Phobos CR3BP rotating state. An algorithm capable of incorporating multiple revolutions as well as the terminal rendezvous constraint is required, as the state along the manifold or the MP-RO changes with the epoch when it is rotated into the inertial frame. Note that this is equivalent to targeting all six elements of the target object while also controlling the time of flight of the transfer.

As an alternative method to the previously developed techniques, a methodology that combines a Lyapunov feedback controller, Q-law [48], and direct collocation [60] is developed. The difference of the proposed method to the previously investigated strategies is that it generates rendezvous trajectory with multiple revolutions over 50, while incorporating third body gravity from the Sun and the moons over a reasonable computation time. While pairing a controller with the direct collocation algorithm are proposed by a number of authors including Betts [87] and Shannon et al. [88], it is noted that the rendezvous requirement is not dealt in these investigations. The history of state and control along the spiral-down (B) arc generated by Q-law is introduced as an initial guess for the direct collocation process, by which the rendezvous is achieved and also the trajectory is optimized. First, the assumptions on the spiral-down (B) arcs are provided, and the dynamical model is recast to the Gaussian Variational Equations to facilitate generation of an initial guess. The Q-law algorithm

is briefly summarized, followed by a step-by-step description of the interface between the algorithms.

5.3.1 Assumptions

Additional assumptions on the spiral-down (B) arc are introduced for a consistent analysis. The resulting trajectory for the spiral-down (B) trajectory depends on the exact locations of the departure and arrival along the Deimos and Phobos science orbits that are periodic in the respective CR3BP system. First, for the Phobos capture orbit, or the Mars-Phobos L_2 Lyapunov orbit plotted in black from Figure 5.3(a), is associated with a planar stable manifold in the Mars-Phobos CR3BP. The manifold offers a dynamical channel through which the spacecraft arrives at the Phobos capture orbit without maneuver. To utilize this advantage, the final state for the Phobos capture orbit is defined as the state along the stable manifold of the Phobos capture orbit where the gravity from Phobos is small enough to be neglected. This threshold radius from Phobos, also called the sphere of influence (SoI), and follows the definition by Canales et al. [77]. The threshold distance is computed at the location along the $\hat{x}$ axis of the respective CR3BP rotating frame, where the ratio of the gravity force from the second primary, or the moon, to the first primary, Mars, is equal to 5×10^{-4}. Following this definition, the radii of Phobos's SoI and Deimos's SoI are $174km$ and $158km$, respectively. Similarly, for the Deimos capture orbit, or the selected Mars-Deimos L_1 Lyapunov orbit illustrated in Figure 5.5, the initial state is defined as the state along the unstable manifold of Deimos with the same definition of the SoI ratio. The intersection between the manifolds and the SoI of the moons result in a portion of arc of the SoI, enabling infinite choices of the boundary states.

The low-thrust maneuvers of spiral-down (B) are required to close the gaps between the energy as well as the eccentricity, or the shapes, of the Phobos and Deimos science orbits. From this perspective, the manifold is deemed as a natural flow that utilizes the gravity of the second primaries, the moons, to adjust the energy of the state of the spacecraft. Figure 5.10 illustrates the trade-off of the energy and eccentricity change along the manifold for both moons. The x-axis of the plots indicate the different locations along the periodic orbit where the spacecraft transitions to the manifolds. For the Deimos capture orbit, it is

desirable if the unstable manifold provides the decrease in the energy such that the energy level is closer to that of Phobos, or the increase of JC_{SM}. But as apparent from Figure 5.10(a), the arc of the manifold that provides maximum "boost" in energy also changes the eccentricity by the largest amount. As the capture orbits are nearly circular around Mars, it is considered desirable to minimize the variation of the eccentricity so that the transfer depends less on the relative phasing of the moons. Thus, the arc that provides minimum change in the eccentricity, that also provides minimum change in the energy is selected and plotted in Figure 5.9(a). Vice a versa, for the Phobos capture orbit manifold, decrease in the energy is desired but is in the trade-off between the eccentricity. From the similar reasoning, the arc that provides minimum eccentricity change is selected and plotted in figure 5.9(b).

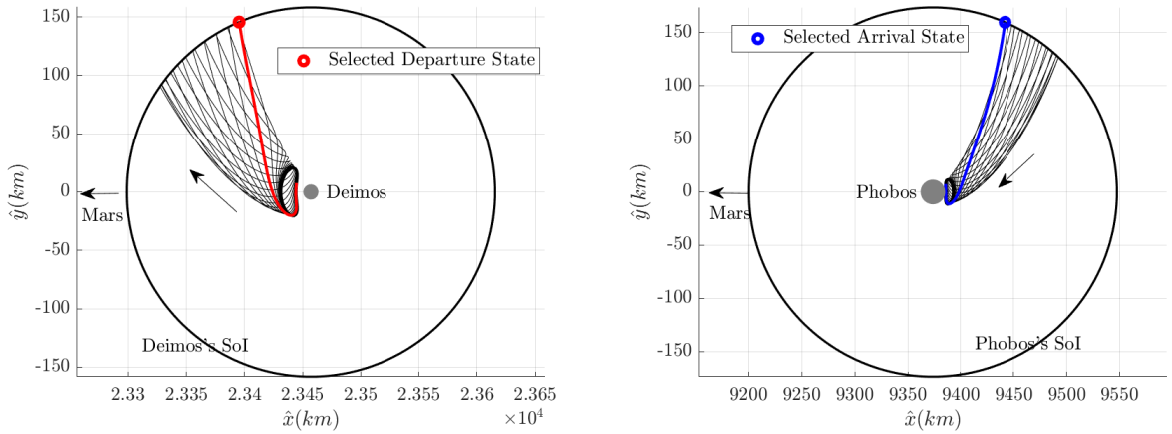

(a) Selected departure state for the Deimos capture orbit, along the unstable manifold from the selected capture orbit

(b) Selected arrival state for the Phobos capture orbit, along the stable manifold into the selected capture orbit

Figure 5.9. Departure and arrival states along the manifolds at the SoIs of the moons

For the flyby orbits defined as the Mars-Deimos or Mars-Phobos resonant orbits in Table 5.4 and 5.3, the departure and arrival locations are illustrated in Figure 5.7(b) and 5.6(a). For the Mars-Deimos resonant orbits, the spacecraft is assumed to depart from the apse that is closer from Deimos, and for the Mars-Phobos resonant orbits, the spacecraft is assumed to depart from the apse that is farther from Phobos in order to avoid numerical problems that may occur when trying to target a state very close to Phobos. Finally, the departure epoch, JD_0, is fixed for every investigated scenario to be Nov 12th, 2021.

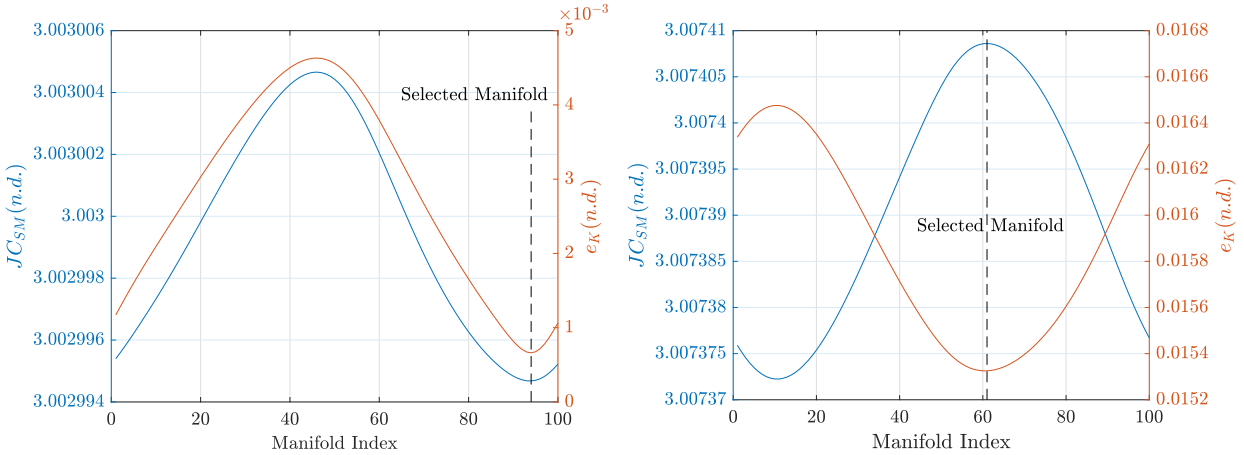

(a) Tradeoff of Deimos captur orbit, unstable manifold

(b) Tradeoff of Phobos captur orbit, stable manifold

Figure 5.10. Tradeoff between energy and eccentricity of different arcs along the manifold: JC_{SM} and e_K variations depending on different locations of the departure from and arrival at the capture orbits.

5.3.2 Gaussian Variational Equations

For the initial guess of low-thrust trajectories between the martian moons, it is advantageous to initially consider only the Martian gravity that results in a Keplerian motion of the spacecraft. This simplification allows the description of the spacecraft state with Keplerian elements: a_K, e_K, i_K, Ω_K, ω_K, and ν_K, where the six elements stay constant without any perturbing forces. Introducing the low-thrust engine thrust as the only perturbing force, the Gaussian variational equations (GVE) are obtained [49], where the rates of change of the six orbital elements are represented as functions of the orbital elements and the perturbing low-thrust acceleration terms, i.e.,

$$\frac{da_K}{d\tilde{t}} = \frac{2a_K^2}{h^2}\left(\mathrm{e}_K \sin\nu_K \frac{\tilde{T}_r}{m} + \frac{p}{r}\frac{\tilde{T}_t}{m}\right) \tag{5.2}$$

$$\frac{d\mathrm{e}_K}{d\tilde{t}} = \frac{1}{h}\left(p\sin(\nu_K)\frac{\tilde{T}_r}{m} + ((p+r)\cos\nu_K + r\mathrm{e})\frac{\tilde{T}_t}{m}\right) \tag{5.3}$$

$$\frac{d\mathrm{i}_K}{d\tilde{t}} = \frac{r\cos(\nu_K+\omega_K)}{h}\frac{\tilde{T}_h}{m} \tag{5.4}$$

$$\frac{d\Omega_K}{d\tilde{t}} = \frac{r\sin(\nu_K+\omega_K)}{h\sin\mathrm{i}_K}\frac{\tilde{T}_h}{m} \tag{5.5}$$

$$\frac{d\omega_K}{d\tilde{t}} = \frac{1}{\mathrm{e}_K+h}(-p\cos\nu_K\frac{\tilde{T}_r}{m} + (p+r)\sin\nu_K\frac{\tilde{T}_t}{m}) - r\sin(\nu_K+\omega_K)\frac{\cos\mathrm{i}_K}{h\sin\mathrm{i}_K}\frac{\tilde{T}_h}{m} \tag{5.6}$$

$$\frac{d\nu_K}{d\tilde{t}} = \frac{h}{r^2} + \frac{1}{\mathrm{e}h}(p\cos\nu_K\frac{\tilde{T}_r}{m} - (p+r)\sin\nu_K\frac{\tilde{T}_t}{m}), \tag{5.7}$$

$$\tag{5.8}$$

where $p = a_K(1-\mathrm{e}_K^2), h = \sqrt{\tilde{G}\tilde{m}_{Mars}p}$, and $r = p/(1+\mathrm{e}\cos\nu)$. The thrust components, $\tilde{T}_r, \tilde{T}_t$, and $\tilde{T}_h$, are represented in the local-vertical local-horizontal (LVLH) frame,

$$\bar{\tilde{T}} = \tilde{T}_r\hat{r} + \tilde{T}_t\hat{h} + \tilde{T}_h\hat{h}, \tag{5.9}$$

where the unit vectors are defined as,

$$\hat{r} = \frac{\bar{\tilde{R}}_{12}}{\tilde{R}_{12}} \tag{5.10}$$

$$\hat{h} = \frac{\bar{\tilde{R}}_{12} \times \frac{{}^{I}d\bar{\tilde{R}}_{12}}{d\tilde{t}}}{|\bar{\tilde{R}}_{12} \times \frac{{}^{I}d\bar{\tilde{R}}_{12}}{d\tilde{t}}|} \tag{5.11}$$

$$\hat{t} = \hat{h} \times \hat{r}, \tag{5.12}$$

where $\bar{\tilde{R}}_{12}$ corresponds to the vector defined in Equation (2.2), and is the position vector from the central body, Mars, to the spacecraft. Two thrusting angles α and β are defined as,

$$\alpha = \tan^{-1} \frac{\tilde{T}_t}{\tilde{T}_r} \tag{5.13}$$

$$\beta = \sin^{-1} \frac{\tilde{T}_h}{\tilde{T}}, \tag{5.14}$$

to result in,

$$\tilde{T}_r = \tilde{T} \cos\beta \sin\alpha \tag{5.15}$$

$$\tilde{T}_t = \tilde{T} \cos\beta \cos\alpha \tag{5.16}$$

$$\tilde{T}_h = \tilde{T} \sin\beta. \tag{5.17}$$

With GVE, a many-revolution low-thrust trajectory problem is recast into a two-body problem, where low-thrust engine accelerations are utilized to control the orbital elements to target the elements of the destination orbit. It is noted that the right sides of Equations (5.2)-(5.7) are not explicit functions of time, $\tilde{t}$.

Although the rates of change of the orbital elements are coupled with thrust in three directions, some orbital elements are more strongly affected by a portion of the directions and are conceptually separated. The angles i_K and Ω_K are only coupled with the out-of-plane direction thrust, $\tilde{T}_h$. Additionally, when e_K is small, the rate of change of a_K is under a greater influence of $\tilde{T}_t$, or the tangential direction thrust, compared to the radial direction thrust, $\tilde{T}_r$. The eccentricity, e_K, is coupled with both $\tilde{T}_r$ and $\tilde{T}_t$, but the the relative influence they have on e_K depends strongly on the true anomaly, ν_K, especially when e_K is small. If

the spacecraft is at a location where $|\sin\nu_K| > 2|\cos\nu_K|$, the radial direction thrust $\tilde{T}_r$ has generally more influence on the eccentricity compared to $\tilde{T}_t$. When e_K is small, while a_K is mainly changed via $\tilde{T}_t$, e_K is changed via both $\tilde{T}_t$ and $\tilde{T}_r$. And for the investigated scenarios, the e_K is small near departing from or approaching the capture orbits of the moons. It is noted that the portion of $\tilde{T}_r$ compared to $\tilde{T}_t$ may serve as an indirect indication of the maneuvers that are required to change the eccentricity, while portion of $\tilde{T}_h$ compared to the thrust magnitude, $\tilde{T}$, indicates the maneuvers needed to change the orbital plane, i_K and Ω_K.

5.3.3 Q-law

The Q-law algorithm used in this investigation is originally presented by Petropoulos [48], and part of this section is a restatement of his work. A Q-law control strategy utilizes a candidate Lyapunov function, Q, to quantify the distance from the osculating orbital elements to the target orbital elements,

$$Q = (1 + W_P P) \sum_{\text{œ}} \boldsymbol{W}_{\text{œ}} \boldsymbol{S}_{\text{œ}} \left(\frac{d(\text{œ}, \text{œ}_T)}{\dot{\text{œ}}_{xx}} \right)^2, \tag{5.18}$$

where œ represents the osculating orbital elements and œ_T denotes the target elements, except for the true anomaly, i.e.,

$$\text{œ} = a_K, \mathrm{e}_K, \mathrm{i}_K, \Omega_K, \omega_K \tag{5.19}$$

$$\text{œ}_T = a_{K,T}, \mathrm{e}_{K,T}, \mathrm{i}_{K,T}, \Omega_{K,T}, \omega_{K,T}. \tag{5.20}$$

Note that all six osculating orbital elements follow the equations of motion described by Equations (5.2)-(5.7) that depend only on the osculating elements as well as the low-thrust engine acceleration. P represents the minimum periapsis constraint and takes the form as,

$$P = \exp\left(k(1 - \frac{r_p}{r_{p,min}}) \right), \tag{5.21}$$

where k is a scalar, r_p and $r_{p,min}$ are osculating periapsis radius and the minimum periapsis radius, respectively. The term W_P denotes a scalar weight for the penalty function. Next, $\boldsymbol{S}_{\text{œ}}$ corresponds to a scaling function that prevents the a_K from diverging from the target value, and takes the form,

$$\boldsymbol{S}_{\text{œ}} = \begin{cases} \left(1 + \left(\frac{a_K - a_{K,T}}{c_1 a_{K,T}}\right)^{c_2}\right)^{1/c_3} & \text{for } \text{œ} = a_K \\ 1 & \text{for } \text{œ} = \mathrm{e}_K, \mathrm{i}_K, \Omega_K, \omega_K, \end{cases} \tag{5.22}$$

where the user-selected constants c_1, c_2, and c_3 are defined as $3, 4$, and 5, respectively, following Petropoulos's definition. The function $d(\text{œ}, \text{œ}_T)$ denotes the distance from the osculating elements to the target elements, defined as,

$$d(\text{œ}, \text{œ}_T) = \begin{cases} \text{œ} - \text{œ}_T & \text{for } \text{œ} = a_K, \mathrm{e}_K, \mathrm{i}_K \\ d(\text{œ}, \text{œ}_T) = \cos^{-1}\Big(\cos(\text{œ} - \text{œ}_T)\Big) & \text{for } \text{œ} = \Omega_K, \omega_K, \end{cases} \tag{5.23}$$

where cosine functions for Ω_K, ω_K are introduced to search for distances that are smaller than 180°. Next, $\dot{\text{œ}}_{xx}$ refers to the maximum rate of change of the orbital elements given the current œ, that is achievable by constantly thrusting at the maximum level, and depends on the direction of the force, α, β, as well as the location along the osculating Keplerian orbit, ν_K, i.e,

$$\dot{\text{œ}}_{xx} = \begin{cases} \max\limits_{\alpha,\beta,\nu_K} (\dot{\text{œ}}) & \text{for } \text{œ} = a_K, \mathrm{e}_K, \mathrm{i}_K, \Omega_K \\ \max\limits_{\alpha,\nu_K} (\dot{\text{œ}}|_{\beta=0}) & \text{for } \text{œ} = \omega_K, \end{cases} \tag{5.24}$$

where Petropoulos introduced a simplifying assumption to ω_K that $\beta = 0$, due to the complexity of the right hand side of Equation (5.6) [89]. Note that the analytical expressions for $\dot{\text{œ}}$ are provided in Petropoulos [48]. Finally, $\boldsymbol{W}_{\text{œ}}$ denotes the user-defined scalar weights, or control gains, for each orbital elements, greater than or equal to zero. As it determines the priority of the elements to be targeted, different combinations of the gains for result in significantly varying performance. While an outer-loop genetic algorithm can be utilized for

gain tuning and to obtain globally optimal solution of the inner-loop Q-law algorithm, [90], it remains out of the scope of the current investigation. Therefore, the gains for all five target elements are set to be 1 for an unbiased formulation.

Equation (5.18), Q, denotes the distance of the osculating orbital elements to the target orbital elements, measured as the square of the estimated time that is required for the targeting. Note that it is not an actual measure of the time, but an overly optimistic projection since the distance for each element is divided by the corresponding maximum rate of change achievable. And this maximum value for each element occurs at different set of α, β, ν_K values and cannot be reached simultaneously for all œ. Since when Q becomes zero, the target orbital elements are achieved, the goal is to minimize the time rate of change of Q at each instant, i.e.,

$$\frac{dQ}{d\tilde{t}} = \sum_{\text{œ}} \frac{\partial Q}{\partial \text{œ}} \frac{d\text{œ}}{d\tilde{t}}, \tag{5.25}$$

where minimizing $\frac{dQ}{d\tilde{t}}$ results in decreasing Q in the fastest way until Q becomes zero. It is noted that Q is not an explicit function of time, $\tilde{t}$. Instead, it is a function of the thrusting angles α and β at each instant, and is re-written as [91],

$$\frac{dQ}{d\tilde{t}} = D_1 \cos\beta \cos\alpha + D_2 \cos\beta \sin\beta + D_3 \sin\beta, \tag{5.26}$$

where D_1, D_2, and D_3 are the partial derivatives of Q with respect to each thrust component, i.e.,

$$D_1 = \sum_{\text{œ}} \frac{\partial Q}{\partial \text{œ}} \frac{\partial \text{œ}}{\partial \tilde{T}_t} \tag{5.27}$$

$$D_2 = \sum_{\text{œ}} \frac{\partial Q}{\partial \text{œ}} \frac{\partial \text{œ}}{\partial \tilde{T}_r} \tag{5.28}$$

$$D_3 = \sum_{\text{œ}} \frac{\partial Q}{\partial \text{œ}} \frac{\partial \text{œ}}{\partial \tilde{T}_h}. \tag{5.29}$$

Then, the optimal thrusting angles, α^*, β^* that minimizes $\frac{dQ}{dt}$ is computed as,

$$\alpha^* = \tan_2^{-1}(D_2, -D_1) \tag{5.30}$$

$$\beta^* = \tan^{-1}(\frac{-D_2}{\sqrt{D_1^2 + D_2^2}}), \tag{5.31}$$

where $\tan_2^{-1}$ is a four quadrant arctangent. Note that the partial derivatives of the orbital elements with respect to the thrust components are readily available from Equations (5.2)-(5.7). The partial derivatives of Q with respect to the orbital elements, on the other hand, may be difficult to obtain. In this investigation, finite difference method is utilized to compute the derivatives. Although Q-law, in its simplest form, is efficient in generating a possible transfer between two orbits, it fails to target the fast-variable (true anomaly), implying that it cannot specify the exact location along the destination orbit where the spacecraft arrives at. Moreover, the time of flight along a trajectory generated with Q-law is unknown a priori; thus, the Q-law algorithm by itself cannot handle a rendezvous problem. This poses a problem since in this analysis, for the spacecraft to arrive at the Phobos science orbit, both the true anomaly of the s/c along the Phobos science orbit at the arrival and the time of flight for the spiral-down arc should be specified. This investigation overcomes this challenge by leveraging direct collocation, and the trajectory generated with Q-law only serves as an initial guess and remains a preliminary transfer solution.

An example of this preliminary solution generated with the Q-law algorithm is illustrated in Figure 5.11. First, the departure state from the Deimos science orbit, 5:4 MD-RO in the example, is rotated into the MARSIAU frame to be converted into the oscualating Mars-2BP orbital elements at JD_0. Then, the the state of Phobos is retrieved from the ephemerides at an epoch 30 days later from JD_0, and is converted to Mars-2BP orbital elements. Then, all the Phobos's orbital elements except for the true anomaly become the target orbital element, $œ_T$ for the Q-law algorithm. The Q-law algorithm produces a transfer geometry in Figure 5.11(a), where the yellow and the red circles correspond to the state of Phobos at the final epoch and the final state of the Q-law trajectory, respectively. Indeed, the algorithm fails to target the true anomaly. Figure 5.11(b) illustrates the time history of the orbital elements of the Q-law trajectory. It is noted that the elements gradually approach the target

elements through by continuously thrusting at the maximum level with the Q-law controller. As Q-law only approaches the target elements asymptotically, it is possible that the process takes significantly long time to arrive at the targeted elements. To prevent this behavior, the tolerances for each element are introduced, below which the Q-law algorithm stops targeting that element by setting the respective gain to zero [88]. $1km, 0.001, 0.001°, 0.001°, 0.001°$ have been utilized in this investigation for $a_K, \mathrm{e}_K, \mathrm{i}_K, \Omega, \omega$, respectively. Again, it is emphasized that the time of the flight of the Q-law algorithm is not known a priori.

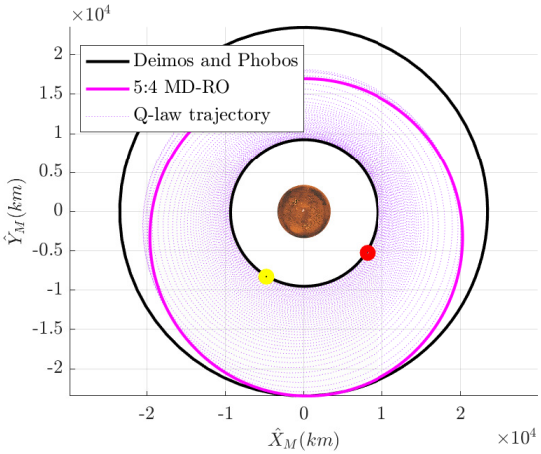

(a) Geometry of the transfer in the MARSIAU frame

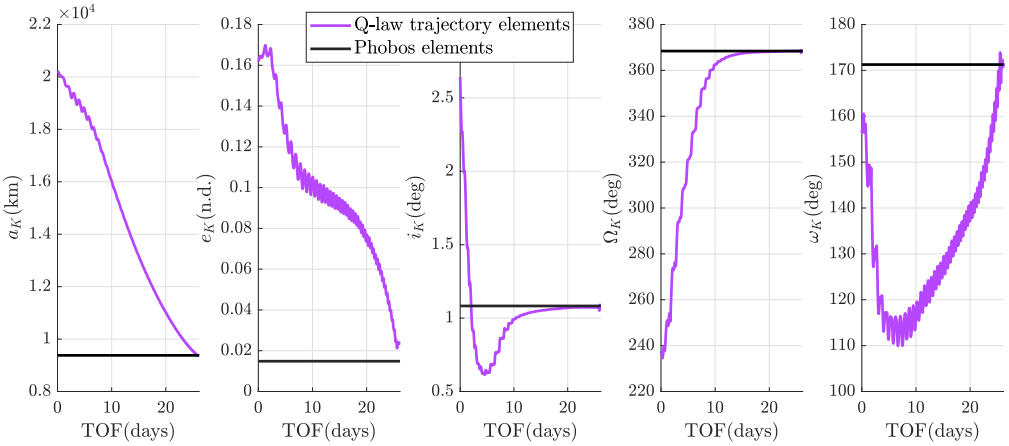

(b) Time history of the orbital elements of the transfer trajectory

Figure 5.11. An example of the preliminary transfer solution generated with the Q-law algorithm

5.3.4 Interface

Recall that the main challenge with a Q-law control approach for the application of the spiral-down (B) scheme is that it fails to target the true anomaly of the s/c upon its arrival at the Phobos science orbit. To address this deficiency, the results from Q-law are now passed to a direct collocation algorithm that not only accommodates the Phobos rendezvous, but also serves as an optimizer under the higher-fidelity ephemeris model. The algorithm that interfaces the Q-law control history and the direct collocation targeting is described with the following steps:

1. The initial state from a selected Deimos science orbit, is rotated into the MARSIAU frame at the initial epoch, JD_0. The position and velocity components in the MARSIAU frame are converted to the osculating Keplerian elements in the same frame and utilized as the initial œ for the Q-law algorithm.

2. The final state, defined as either the state along the stable manifold associated with the Phobos capture orbit when it crosses the SoI for Phobos (Figure 5.9(b)) or the state along the Phobos flyby orbits (Figure 5.6(a)), is converted into the osculating orbital elements in the Mars-2BP at an estimated final epoch, $JD_{f,est}$. These elements serve as the target variables for the Q-law guidance process. The position of this final state in a Mars-centered inertial frame is represented as the yellow circle in Figure 5.12(a). $JD_{f,est}$ is provided by the user with the estimates on the time of flight the transfer requires from JD_0, can be adjusted by trial and error.

3. A preliminary transfer from the elements of the initial state to the target elements of the final state is generated with the Q-law algorithm. As a result, the state and control history for this transfer is constructed, where the position history is represented as the dotted purple arc in Figure 5.12(a).

4. Since Q-law fails to target the true anomaly, the location at the end of the preliminary transfer (red circle in Figure 5.12(a)) does not coincide with the anticipated final state. This discrepancy in positions is accommodated by shifting the yellow circle closer to

the red circle by selecting a different final epoch. This new final epoch is determined via the equation,

$$JD_{f,new} = \arg\min_{JD_f} |\bar{\bar{R}}_{12,Qf} - \bar{\bar{R}}_{12,f}(JD_f)| \tag{5.32}$$

Here, $\bar{\bar{R}}_{12}$ denotes a position vector of the spacecraft with respect to Mars in the MARSIAU frame. The additional subscripts f and Qf correspond to the actual final state to be targeted (yellow circle in Figure 5.12(a)) and the final location along the preliminary transfer generated with the Q-law strategy (red circle in Figure 5.12(a)), respectively. Note that $\bar{\bar{R}}_{12,f}$ depends on the final epoch, JD_f, since the epoch determines the location of Phobos as well as the location of the final state in the MARSIAU frame. On the contrary, $\bar{\bar{R}}_{12,Qf}$ is computed once from the preliminary transfer of the Q-law algorithm and is constant over different epochs, which is a valid assumption if the osculating orbital elements of Phobos around Mars do not change substantially over the period between $JC_{f,est}$ and $JD_{f,new}$. Then, Eq. (5.32) is equivalent to determining a new final epoch that minimizes the distance between the final state at the final epoch, $\bar{\bar{R}}_{12,f}(JD_f)$, represented as the yellow circle, and the final location (the red circle) along the original trajectory generated with the Q-law guidance scheme, $\bar{\bar{R}}_{12,Qf}$, represented as the red circle.

5. The difference between the estimated and the new final epoch is defined as $\Delta JD_f = JD_{f,new} - JD_{f,est}$. An intermediate Mars-centered conic arc, with a period equal to ΔJD_f, is introduced. Then, the semi-major axis corresponding to this period is computed as $a_{K,I} = (\tilde{G}\tilde{m}_{Mars}\Delta JD_f^2)^{1/3}$, where $\tilde{G}\tilde{m}_{Mars}$ the gravitational parameter of Mars included in Table 2.1. When the a_K from the Q-law preliminary solution crosses $a_{K,I}$, one revolution of the corresponding conic, i.e., the blue arc in Figure 5.12(a), is inserted into the state history of the state generated by Q-law. As the s/c spends more time on this conic, the distance between $\bar{\bar{R}}_{12,Qf}$ and $\bar{\bar{R}}_{12,f}$ is minimized. It is noted that as the preliminary solution from the Q-law is not an explicit function of time, inserting one revolution of an intermediate conic does not shift the final state of the Q-law preliminary trajectory, $\bar{\bar{R}}_{12,Qf}$. The key is to utilize the Q-law algorithm once

and to utilize that information, as time of flight of the Q-law algorithm shifts every time it is solved again.

6. The state and control histories, including the intermediate ballistic conic, is discretized to form an initial guess for the direct collocation scheme, as illustrated in Figure 5.12(b). Each revolution of the spiral-down arc is discretized into five to ten segments. And the orbital elements history from the Q-law algorithm is converted into the Cartesian states in the MARSIAU frame, i.e., position and velocity. For better scaling, the states are nondimensionalized using Mars-Deimos CR3BP characteristic quantities included in Table 2.1. While the orbital elements are not utilized within the direct collocation algorithm to avoid singularity issues and thus position and velocity are employed instead, it is possible to utilize modified equinoctial elements to circumnavigate the issue, investigated by Shannon et al. [88]. It is noted that the thrust vector of each segment is still defined in the LVLH frame to facilitate convergence,

$$\boldsymbol{u}_{LVLH,\mathrm{i}} = \begin{bmatrix} T_{\mathrm{i}} & u_{r,\mathrm{i}} & u_{t,\mathrm{i}} & u_{h,\mathrm{i}} \end{bmatrix}, \tag{5.33}$$

where T_{i} corresponds to the nondimensional thrust magnitude over each segment, and each of the control component at each segment is defined as,

$$u_{r,\mathrm{i}} = \frac{\tilde{T}_r}{\tilde{T}} \tag{5.34}$$

$$u_{t,\mathrm{i}} = \frac{\tilde{T}_t}{\tilde{T}} \tag{5.35}$$

$$u_{h,\mathrm{i}} = \frac{\tilde{T}_h}{\tilde{T}}. \tag{5.36}$$

Subsequently, the initial guess is computed for a feasible solution where the trajectory is continuous along all segments while satisfying the boundary conditions. The ephemeris model incorporating Sun, Mars, Phobos and Deimos is utilized for verification of the strategy. The feasible solution is then optimized for propellant consumption. An example of an optimized solution is plotted in Figure 5.20(a).

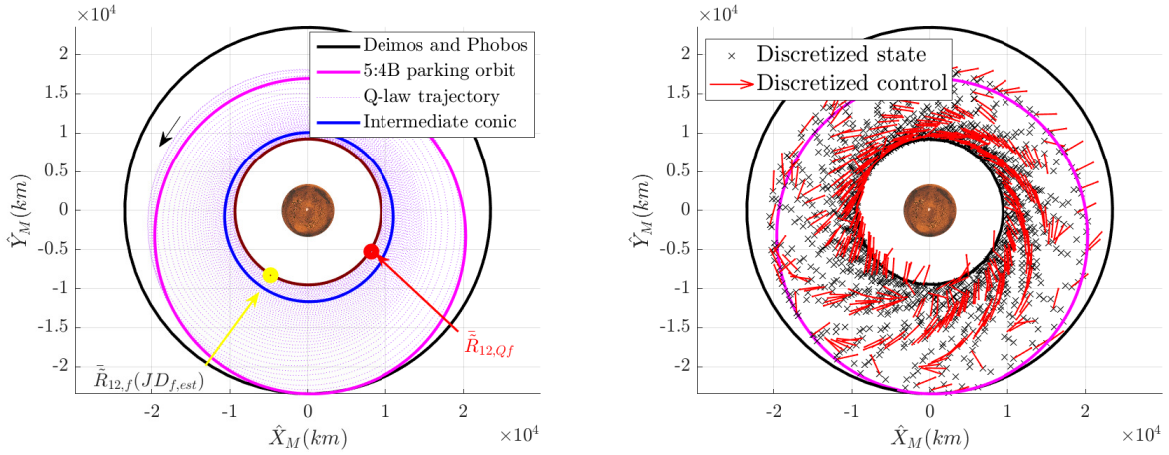

(a) Preliminary transfer generated with Q-law (b) Discretized state and control for direct collocation

Figure 5.12. Interfacing Q-law and direct collocation for generating spiral-down (B)

The above steps consist the interface between the Q-law control and the direct collocation targeter, and succeed in acquiring optimized transfers from each Deimos science orbit to the Phobos science orbit. The associated costs are included in Table 5.5. Again, ΔV corresponds to the equivalent ΔV computed as $\Delta V = \tilde{I}_{sp}\tilde{g}_0 \log\left(\tilde{m}_0/(\tilde{m}_0 - \Delta m)\right)$.

5.4 Results

The resulting geometries in different frames and the thrust histories are illustrated in Figures 5.13-5.20. Each figure consists of six plots associated with different information. The spiral-down (A) arc is not demonstrated due to the similar geometry where it gradually spiral in from the heliocentric leg, represented in Figure 5.8. Taking the capture to capture scenario as an example, the first plot in Figure 5.13(a) demonstrates the orbits of the moons and the spiral-down (B) arc in the MARSIAU inertial frame. It is followed by the history of the thrust magnitude and thrust components in the LVLH frame along the transfer, illustrated in Figure 5.13(b). Recall that the initial guess from the Q-law algorithm has consistent maximum thrust throughout the transfer, and the regions where the the thrust magnitude is not maximum are the results of optimization via the direct collocation algorithm. The thrust magnitude is nondimensionalized with respect to the maximum thrust, and the y axis of the plot corresponds to the ratio of the thrust with respect to the maximum level of thrust. The thrust components in the LVLH are associated with which of the orbital elements are changed at the given time along the transfer trajectory, via Equations (5.2)-(5.7). The following plot in Figure 5.13(c) corresponds to the view in the Mars-Deimos CR3BP rotating frame, where Figure 5.13(d) provides a zoomed-in view near Deimos to illustrate the departure from the Deimos science orbit. It is noted that the Deimos science orbits are also computed in the ephemeris model including Sun, Mars, and the moons. The spiral-down (B) arc appears to be in a counter-clockwise motion in the Mars-Deimos rotating frame. The last two plots in Figures 5.13(e) and 5.13(f) correspond to the views in the Mars-Phobos CR3BP rotating frame, where the latter corresponds to the view near the vicinity of the Phobos to illustrate the arrival at the Phobos science orbit through the manifold, or at the MP-RO. The Phobos science orbits are computed in the same ephemeris model as well. The spiral-down (B) arc is in a clockwise motion in the Mars-Phobos CR3BP rotating frame.

5.4.1 Capture to Capture Scenario

For the Deimos capture orbit to the Phobos capture orbit scenario (Figure 5.13), the spiral-down (B) arc connects the initial and final states defined as the unstable and stable manifold crossings at Deimos's SoI and Phobos's SoI (Figure 5.13(d) and 5.13(f)), respectively. The geometry of the transfer exhibits little variations in the eccentricity, as both the Deimos and Phobos capture orbits are associated with small eccentricities in the MARSIAU frame. This tendency is also indirectly illustrated in the thrust profile in Figure 5.13(b), where the portion of the thrust in the radial direction is relatively small compared to other scenarios that involve science orbits with non-negligible eccentricities (Figure 5.14(b) and 5.15(b)).

5.4.2 Capture to Flyby Scenario

For the Deimos capture orbit to the Phobos flyby orbit scenario (Figure 5.14-5.17), the Mars-Deimos CR3BP rotating frame view also illustrates one period of the selected MP-RO. Note that as orbits of Phobos and Deimos around Mars have a period ratio of approximately $1:4$, apparent from the values in Table 2.1, the $1:2$ MP-RO and $3:4$ MP-RO also appear to have repeating geometries in the Mars-Deimos CR3BP rotating frame (Figure 5.14(c) and 5.16(c)), whereas the other two ratios, $2:3$ and $4:5$ do not appear to be periodic in the same frame (Figure 5.15(c) and 5.17(c)). It is noted that the eccentricity of the Phobos flyby orbits decreases as the p/q ratio increases. The portion of the radial direction thrust $\tilde{T}_r$ tends to decrease as the p/q ratio increases as well for the selected epoch, JD_0. The spiral-down (B) arcs corresponding to this scenario originate from the end of the unstable manifold of the Deimos capture orbit at Deimos's SoI, and finally arrive at the apoapsis of the Phobos flyby orbits.

5.4.3 Flyby to Capture Scenario

The Deimos flyby orbit to the Phobos capture orbit scenario options are illustrated in Figures 5.18-5.20. The MD-ROs have repeating geometries in the Mars-Deimos CR3BP rotating frame. And due to the orbital period ratio between Phobos and Deimos, $2:1$ MD-

RO appears to be periodic in the Mars-Phobos rotating frame as well, while orbits with different ratios, 3 : 2 MD-RO and 5 : 4 MD-RO do not have repeating geometries in the Mars-Phobos CR3BP rotating frame. It is apparent that due to the eccentricity of 2 : 1 MD-RO, significantly more portion of the maneuvers are in the radial direction, compared to the less eccentric 5 : 4 MD-RO. The spiral-down (B) arcs all originate from the periapsis of the MD-ROs, and arrive at the end of the stable manifold of the Phobos capture orbit at Phobos's SoI.

5.4.4 Concluding Remarks

A capability of the framework to generate the tour trajectories of the Martian moons utilizing a low-thrust engine is developed. The sequence of the exploration is fixed to be in the order of Deimos and Phobos. The science orbits for each moon are defined to be either capture or flyby orbits. Three scenarios, (1) Deimos capture to Phobos capture, (2) Deimos capture to Phobos flyby, and (3) Deimos flyby to Phobos capture are examined, and the associated costs corresponding to both types of arc, (A) and (B), are included in Table 5.5.

The costs are represented with the propellant consumption, Δm, the equivalent ΔV, and the time of flight, TOF. As the spiral-down (A) assumes a constant thrust at the maximum level, and the initial guess for spiral-down (B) from the Q-law algorithm also assumes the maximum thrust, Δm and TOF are generally proportional, where variations may result from the optimization of the spiral-down (B) arcs for the propellant consumption. As the total time of flight combined for both types of arcs, (A) and (B), is much smaller than the time of flight of the Earth to Mars trajectory, more fuel efficient trajectories may be obtained in exchange for more time of flight.

The capture to capture scenario represents a tour option that offers the maximum science gain from both moons, as it offers an opportunity to orbit around both Phobos and Deimos. For the capture to flyby scenario, both 1 : 2 and 4 : 5 MP-ROs offer similar level of propellant savings compared to the capture to capture scenario. It is noted that 4 : 5 offers more time for the observation (Table 5.3) of Phobos, and may be preferred to 1 : 2. The propellant saving from utilizing the flyby option for Phobos is approximately 10%. The best candidate orbit for the flyby to capture scenario is 5 : 4 MD-RO, where it results in about 3% saving

of propellant. If this propellant saving is deemed negligible compared to the extra science gain from orbiting around both moons, the capture to capture scenario may be preferred to the scenarios where the spacecraft is captured by one of the moons but only visits the other through flybys.

It is noted that the costs in Table 5.5 are bound to the simplifying assumptions regarding the spiral-down (B) trajectories. From the dynamics perspective, Mars and the moons are assumed to be centrobaric, and the potential eclipse from Mars for the spacecraft is neglected. Also, the locations of the departure from and arrival at the science orbits are fixed for consistent analysis, that may be removed for further optimization of the costs. More importantly, the initial epoch of the departure, JD_0, is fixed for all investigated options, which may restrict the generalization of the obtained costs since the relative phasing as well as the relative orientation of the orbital planes of the moons heavily depend on the epoch. Despite these restrictions from the underlying assumptions, the values in Table 5.5 may support potential low-thrust tour missions in the Martian system by providing a set of reference values.

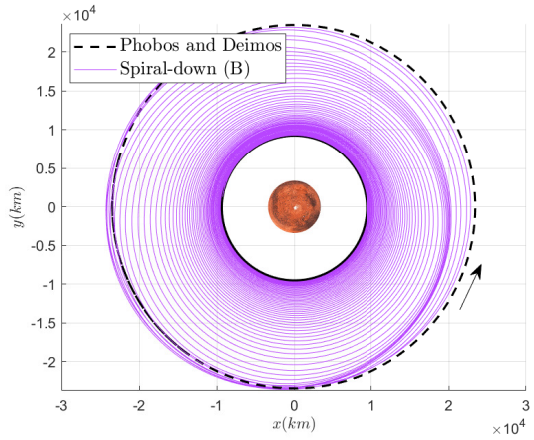

(a) Spiral-down (B) in MARSIAU frame

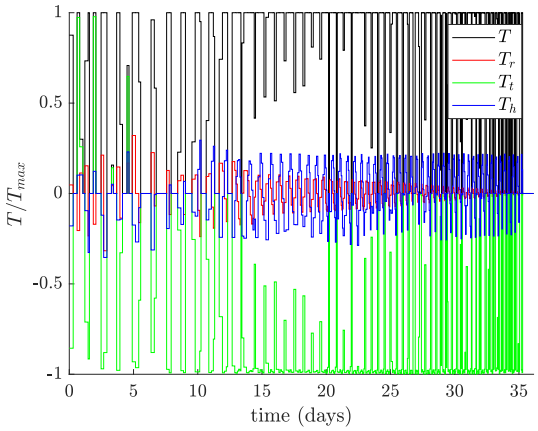

(b) Thrust history

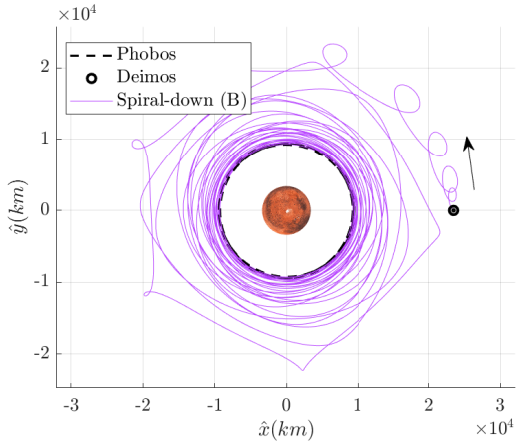

(c) Spiral-down (B) in Mars-Deimos CR3BP rotating frame

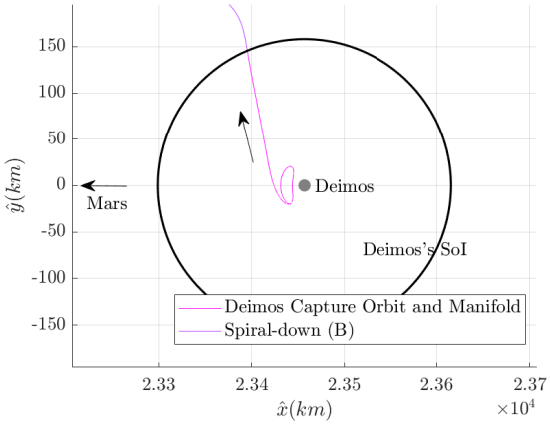

(d) Zoomed-in view near Deimos

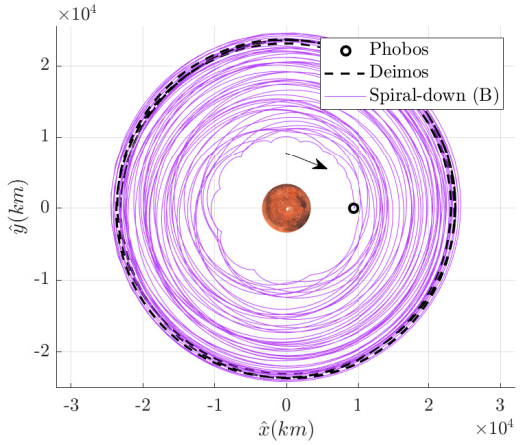

(e) Spiral-down (B) in Mars-Phobos CR3BP rotating frame

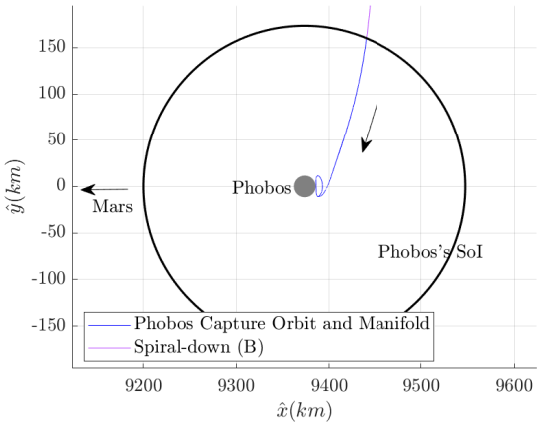

(f) Zoomed-in view near Phobos

Figure 5.13. Deimos capture orbit to Phobos capture orbit

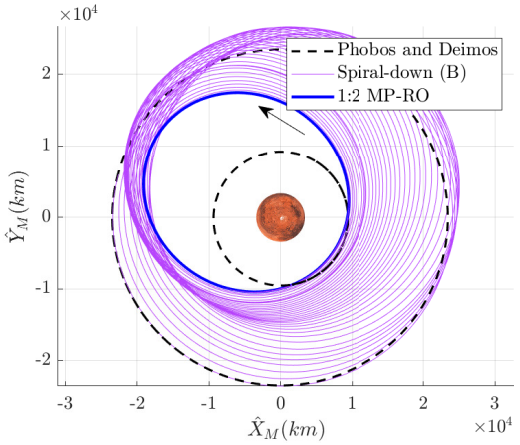

(a) Spiral-down (B) in MARSIAU frame

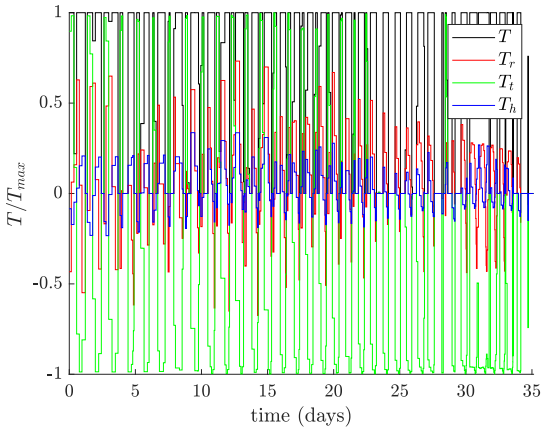

(b) Thrust history

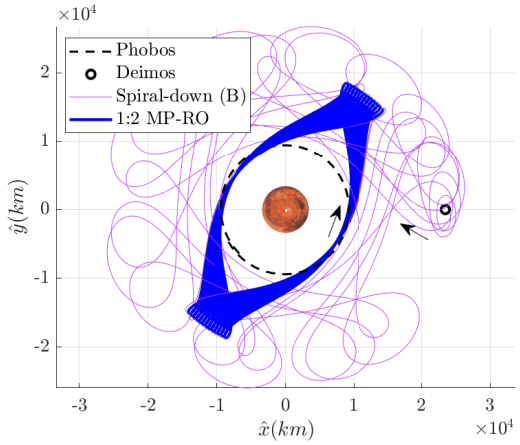

(c) Spiral-down (B) in Mars-Deimos CR3BP rotating frame

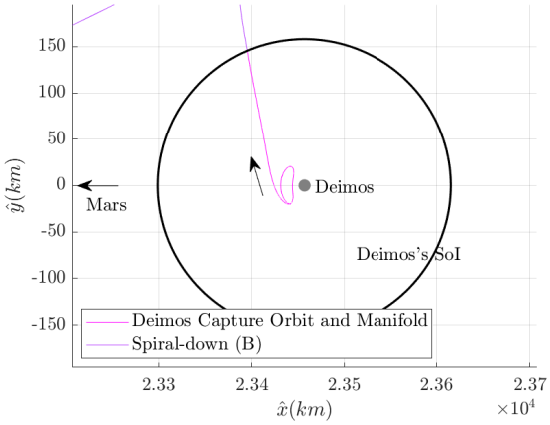

(d) Zoomed-in view near Deimos

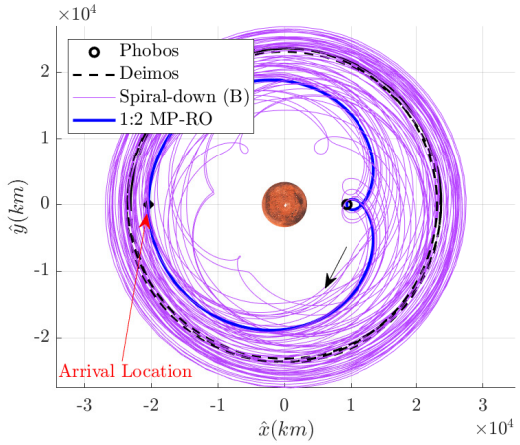

(e) Spiral-down (B) in Mars-Phobos CR3BP rotating frame

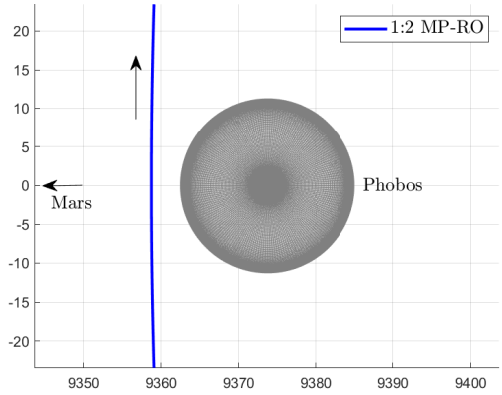

(f) Zoomed-in view near Phobos

Figure 5.14. Deimos capture orbit to Phobos flyby orbit, 1 : 2 MP-RO

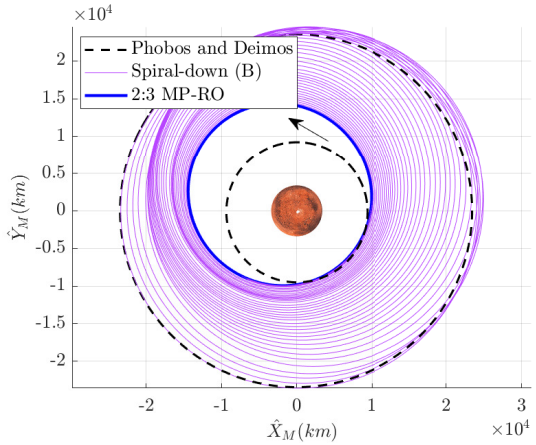

(a) Spiral-down (B) in MARSIAU frame

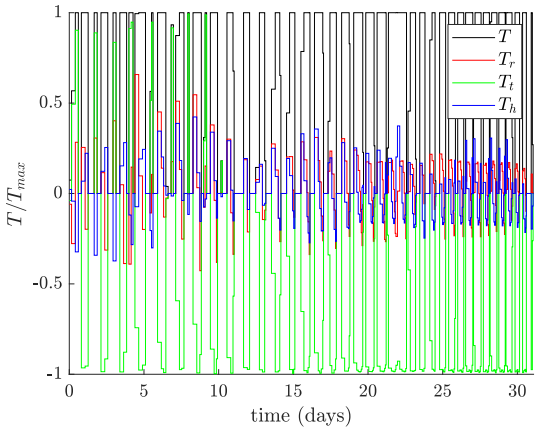

(b) Thrust history

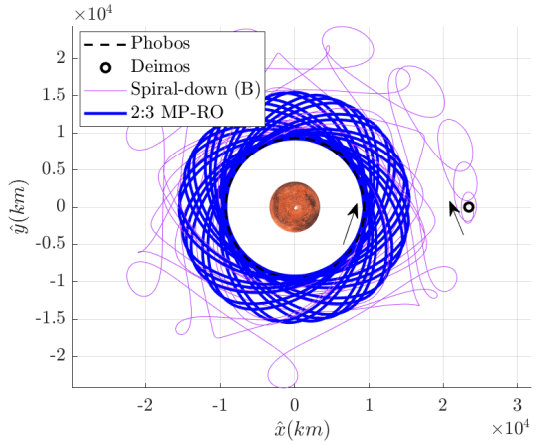

(c) Spiral-down (B) in Mars-Deimos CR3BP rotating frame

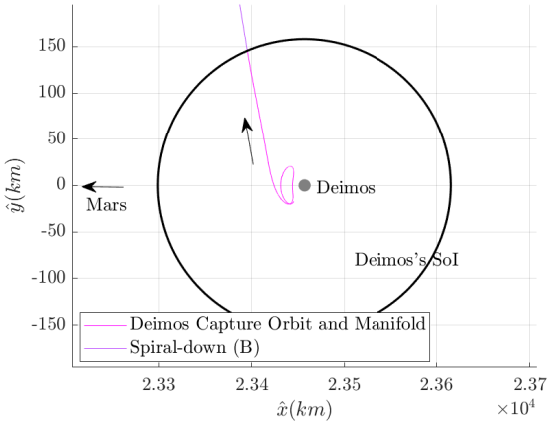

(d) Zoomed-in view near Deimos

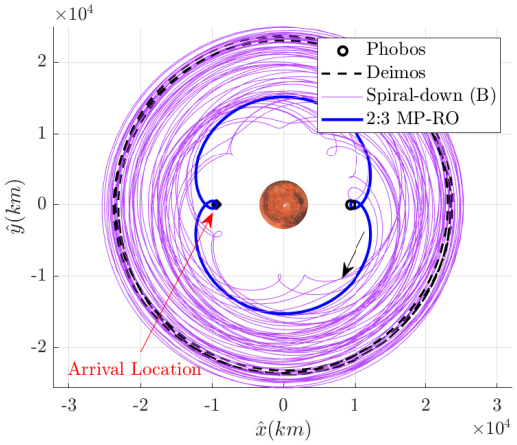

(e) Spiral-down (B) in Mars-Phobos CR3BP rotating frame

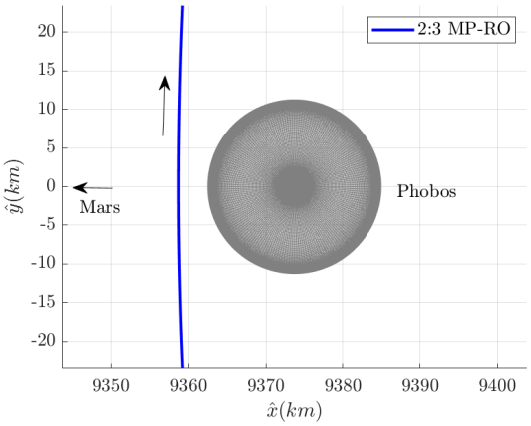

(f) Zoomed-in view near Phobos

Figure 5.15. Deimos capture orbit to Phobos flyby orbit, 2 : 3 MP-RO

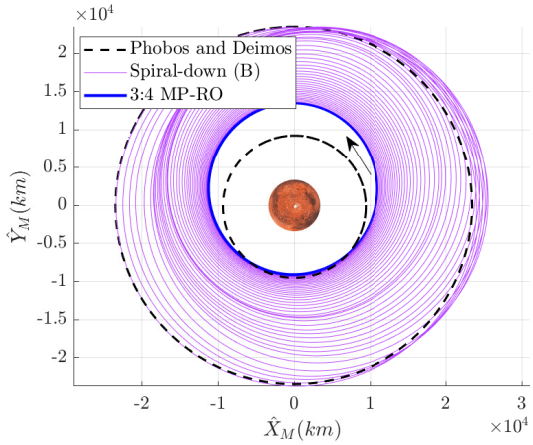

(a) Spiral-down (B) in MARSIAU frame

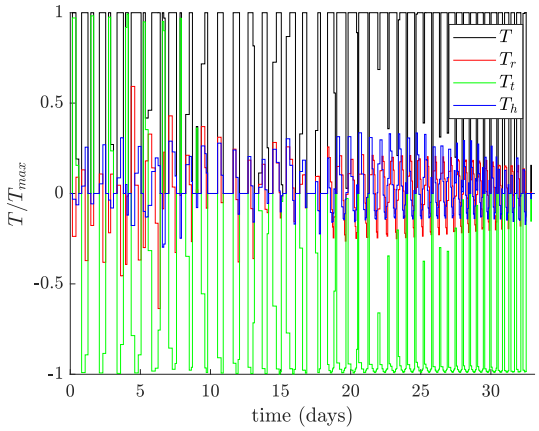

(b) Thrust history

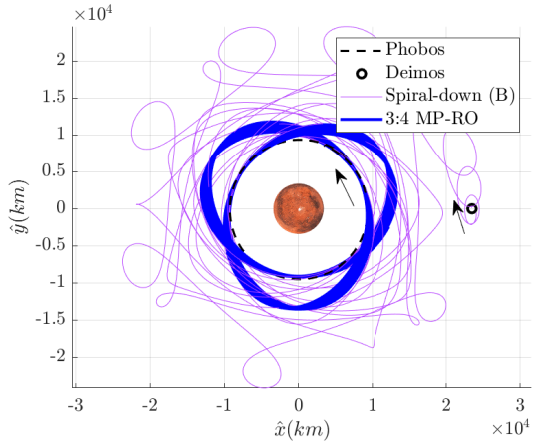

(c) Spiral-down (B) in Mars-Deimos CR3BP rotating frame

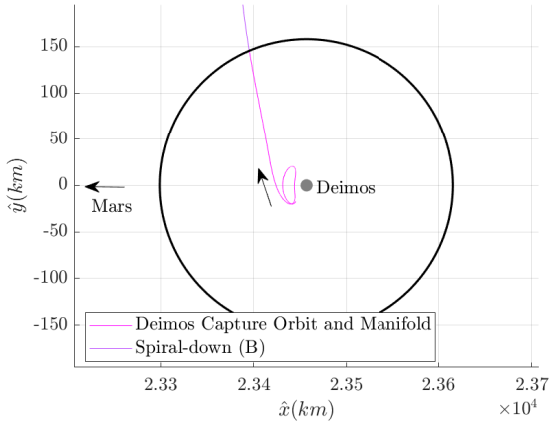

(d) Zoomed-in view near Deimos

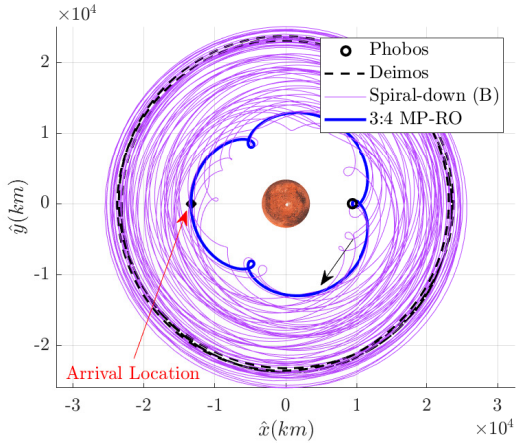

(e) Spiral-down (B) in Mars-Phobos CR3BP rotating frame

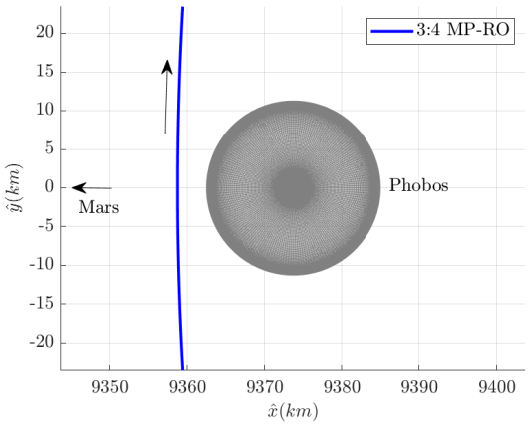

(f) Zoomed-in view near Phobos

Figure 5.16. Deimos capture orbit to Phobos flyby orbit, 3 : 4 MP-RO

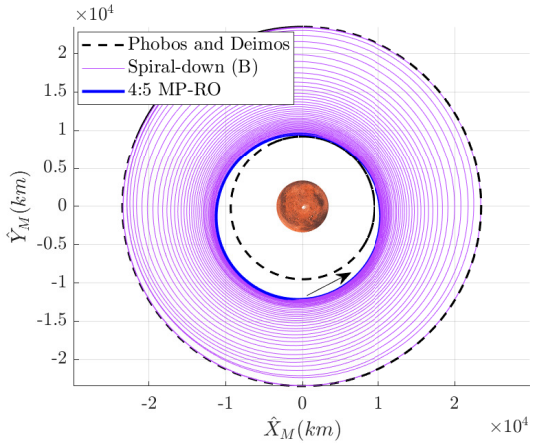

(a) Spiral-down (B) in MARSIAU frame

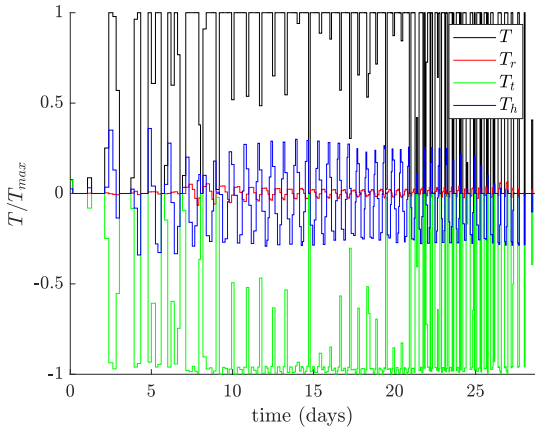

(b) Thrust history

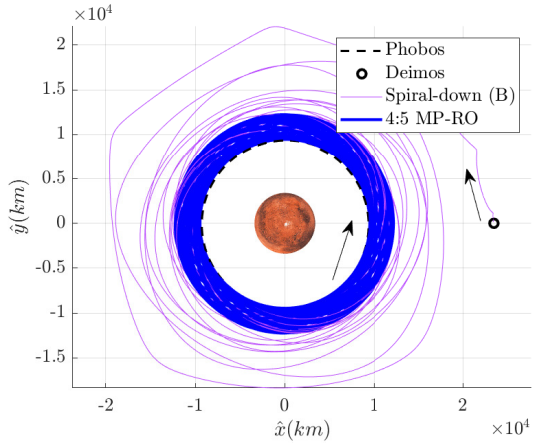

(c) Spiral-down (B) in Mars-Deimos CR3BP rotating frame

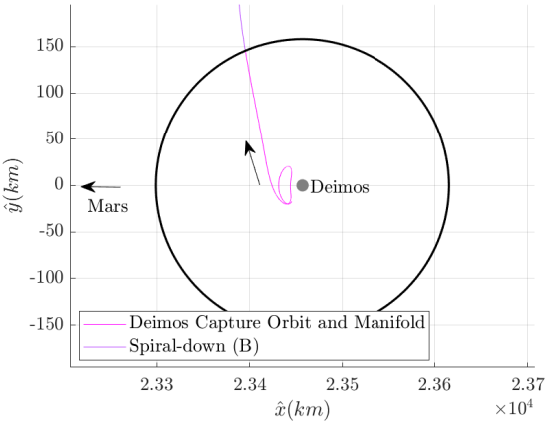

(d) Zoomed-in view near Deimos

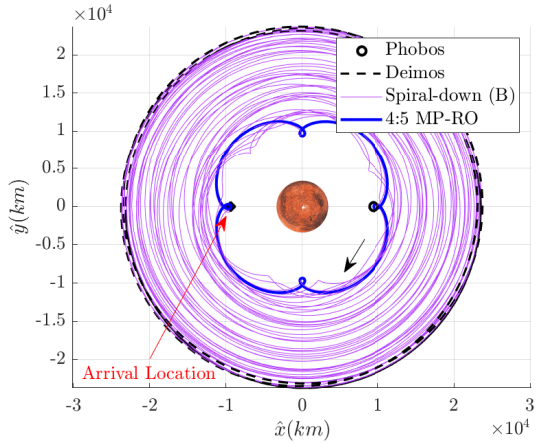

(e) Spiral-down (B) in Mars-Phobos CR3BP rotating frame

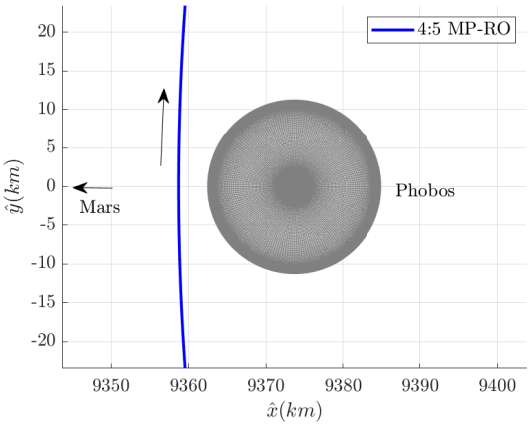

(f) Zoomed-in view near Phobos

Figure 5.17. Deimos capture orbit to Phobos flyby orbit, 4 : 5 MP-RO

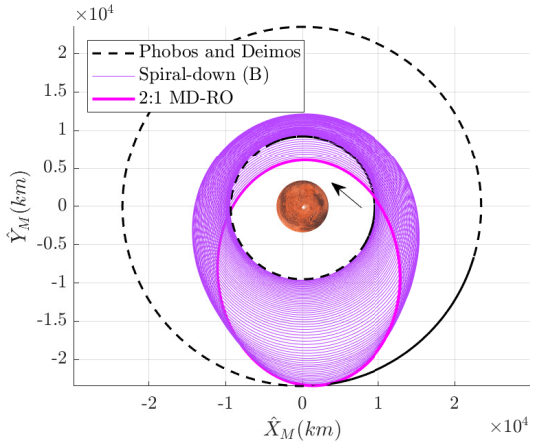

(a) Spiral-down (B) in MARSIAU frame

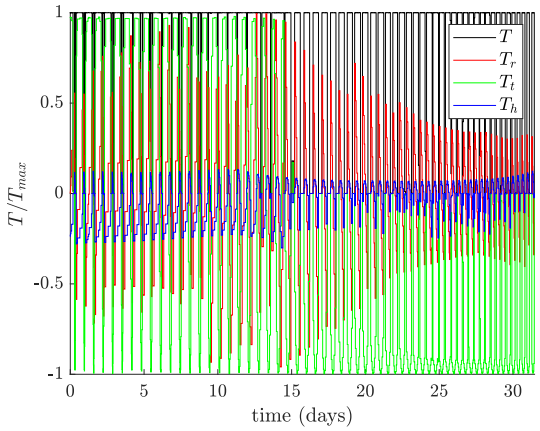

(b) Thrust history

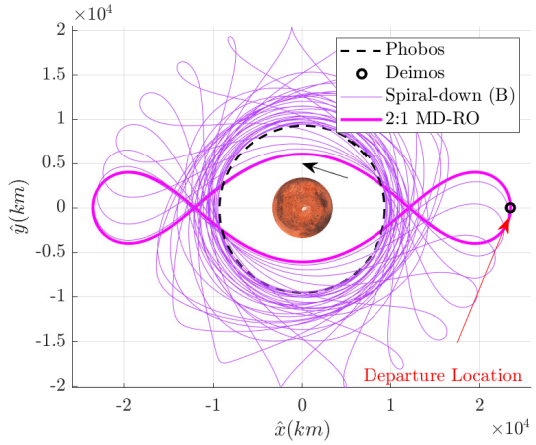

(c) Spiral-down (B) in Mars-Deimos CR3BP rotating frame

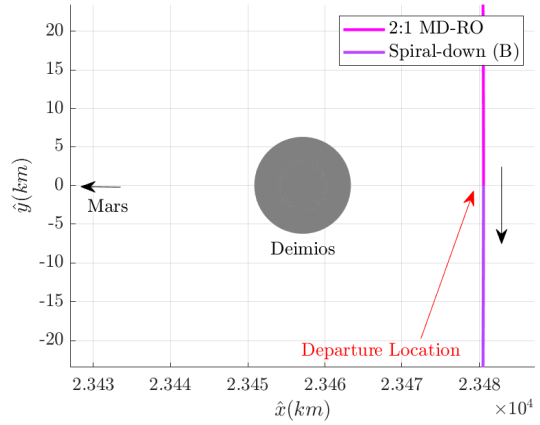

(d) Zoomed-in view near Deimos

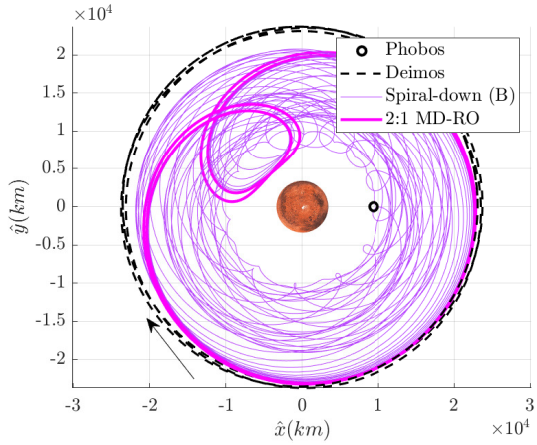

(e) Spiral-down (B) in Mars-Phobos CR3BP rotating frame

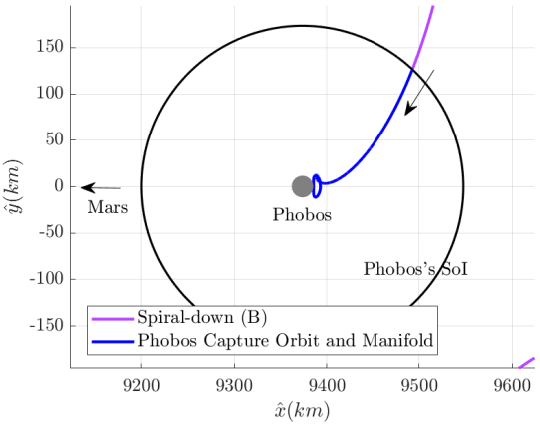

(f) Zoomed-in view near Phobos

Figure 5.18. Deimos flyby orbit, $2:1$ MD-RO, to Phobos capture orbit

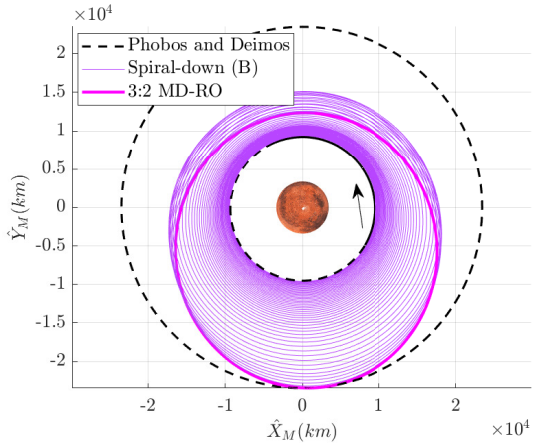

(a) Spiral-down (B) in MARSIAU frame

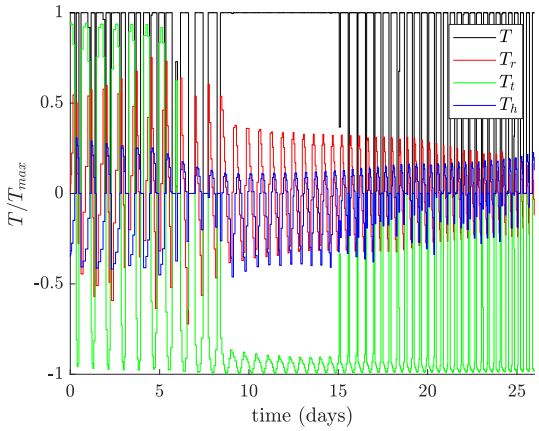

(b) Thrust history

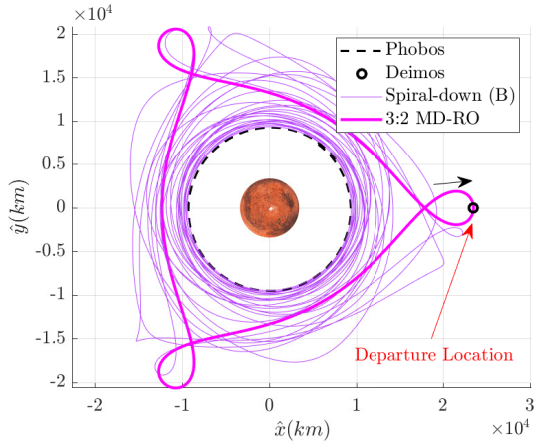

(c) Spiral-down (B) in Mars-Deimos CR3BP rotating frame

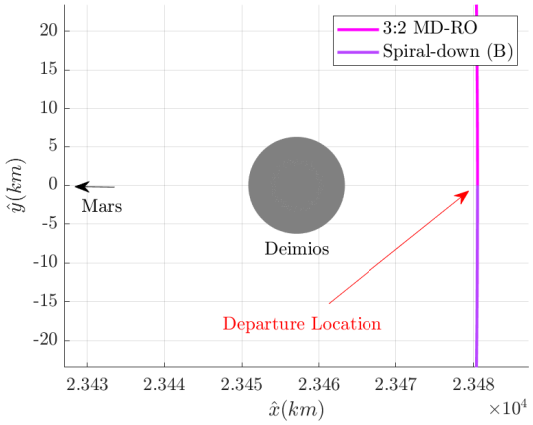

(d) Zoomed-in view near Deimos

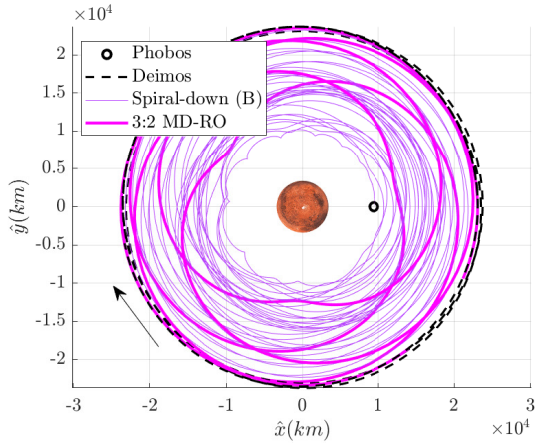

(e) Spiral-down (B) in Mars-Phobos CR3BP rotating frame

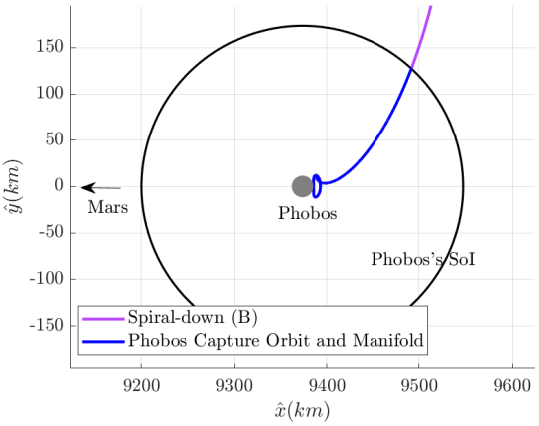

(f) Zoomed-in view near Phobos

Figure 5.19. Deimos flyby orbit, 3 : 2 MD-RO, to Phobos capture orbit

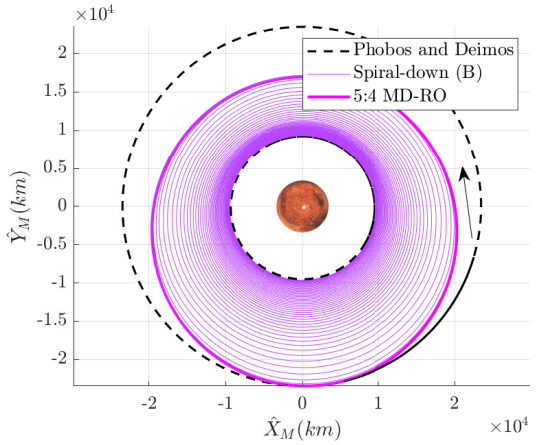

(a) Spiral-down (B) in MARSIAU frame

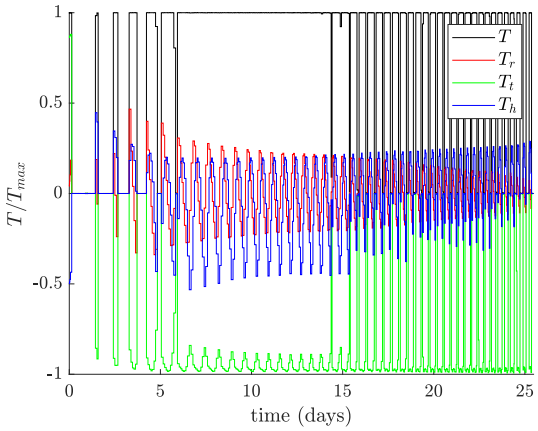

(b) Thrust history

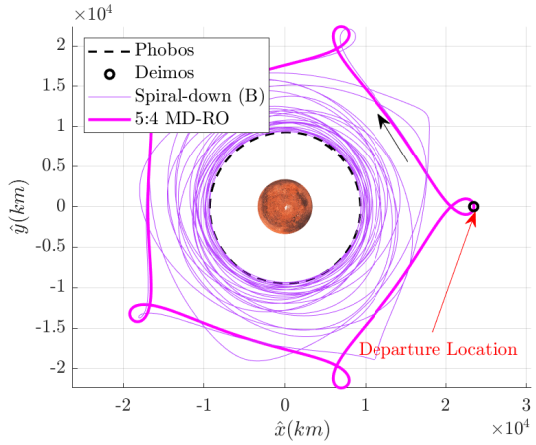

(c) Spiral-down (B) in Mars-Deimos CR3BP rotating frame

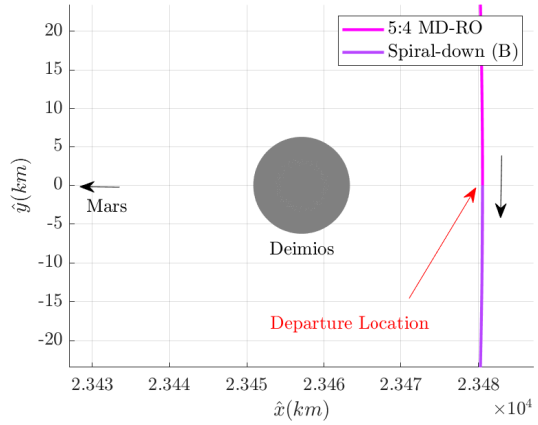

(d) Zoomed-in view near Deimos

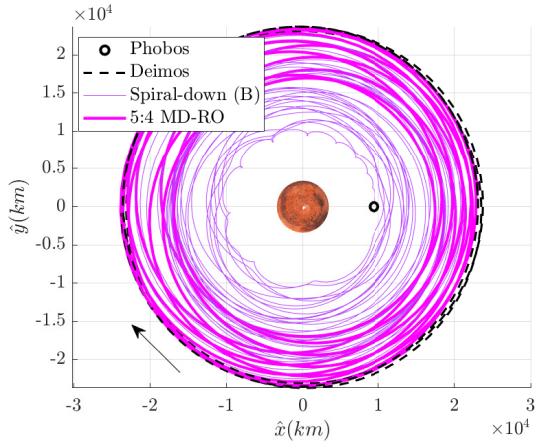

(e) Spiral-down (B) in Mars-Phobos CR3BP rotating frame

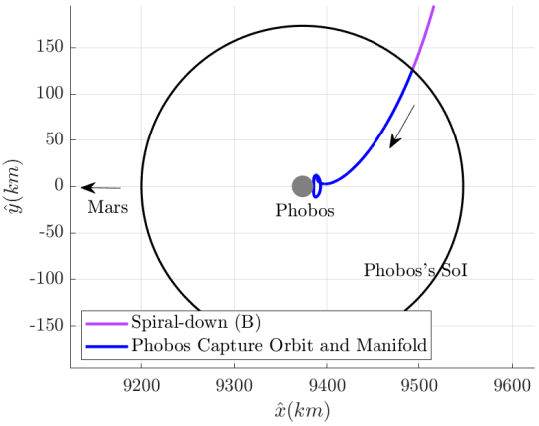

(f) Zoomed-in view near Phobos

Figure 5.20. Deimos flyby orbit, 5 : 4 MD-RO, to Phobos capture orbit

Table 5.5. The costs associated with each option of three scenarios of tour: (1) capture to capture, (2) capture to flyby, and (3) flyby to capture

Scenario	Resonant Orbit	Phase 3: Spiral-down (A)			Phase 4: Spiral-down (B)			(A) + (B)		
		Δm [kg]	ΔV [m/s]	TOF [days]	Δm [kg]	ΔV [m/s]	TOF [days]	Δm [kg]	ΔV [m/s]	TOF [days]
Capture to Capture	-	4.89	944	27.75	4.19*	834*	36.14	9.08	1778	63.89
Capture to Flyby	1:2	4.89	944	27.75	3.31*	656*	28.64	8.20	1601	56.40
	2:3	4.89	944	27.75	3.33*	660*	31.08	8.22	1605	58.84
	3:4	4.89	944	27.75	3.66*	726*	33.12	8.55	1671	60.88
	4:5	4.89	944	27.75	3.31*	657*	28.64	8.20	1601	56.40
Flyby to Capture	2:1	7.10	1431	40.31	4.43*	928*	31.46	11.53	2359	71.77
	3:2	6.00	1205	34.07	3.62*	752*	25.98	9.63	1957	60.06
	5:4	5.47	1096	31.02	3.35*	693*	25.48	8.82	1789	56.49

6. END-TO-END TRAJECTORY DESIGN

The strategies discussed the preceding chapters are combined to generate an end-to-end trajectory between the Earth and the tour of the Martian moons. A higher-fidelity model that incorporates the gravity of the Sun, Earth, Moon, Mars, and Martian moons is utilized to validate the multi-phase framework illustrated in Figure 1.1. Note that an end-to-end trajectory consists of four distinct phases, where Phase 2 and Phase 4 are separately discussed in Chapters 4 and 5, respectively. The current chapter provides the method to generate the rest of the trajectory, Phase 1 and 3, and the steps to convert the piece-wise solutions to an end-to-end trajectory. Each step is illustrated with an exemplary scenario, and the resulting end-to-end trajectory is plotted in different coordinate frames and the associated costs are provided.

6.1 End-to-End Trajectory Design Process

The process of generating an end-to-end trajectory is discussed in detail. It is illustrated in Figure 6.1, consisting of five steps.

6.1.1 Selecting a Pair of Epochs for Phase 2

The process is initiated by a user-provided pair of the epochs for the departure and arrival of the heliocentric leg, or Phase 2. The selected pair is illustrated in Figure 6.2(a), where the departure epoch is selected as 08/08/2026 and the arrival epoch is 500 days after the departure date. The optimal transfer corresponding to this point is plotted in Figure 6.2(b). While the rest of the example proceeds with this selected pair, it is noted that any point of the colored region of the contour plot may be utilized instead. Figure 6.1(a) illustrates the schematic for the current step, where the selected pair of the epochs, JD_D and JD_A, are assigned to the interface points between Phase 1/2 and Phase 2/3, respectively. Note that the vertical dotted lines of the schematic correspond to the interface points between the phases.

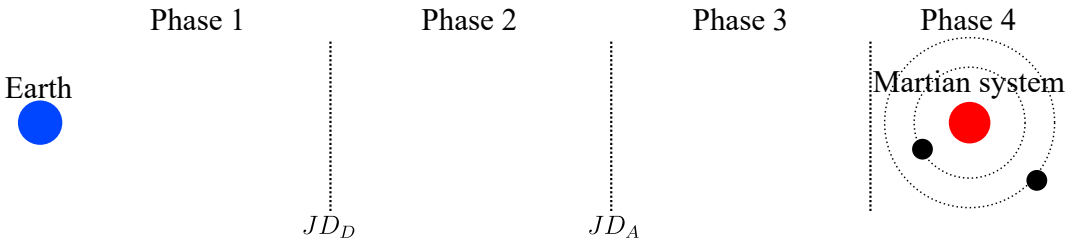

(a) Selecting a pair of epochs for Phase 2

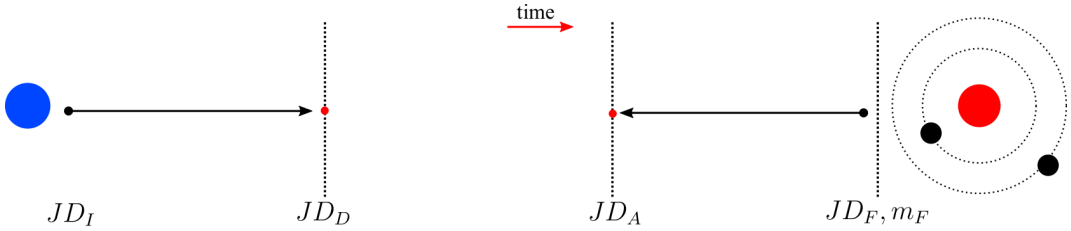

(b) Generating Phase 1 and 3 trajectories

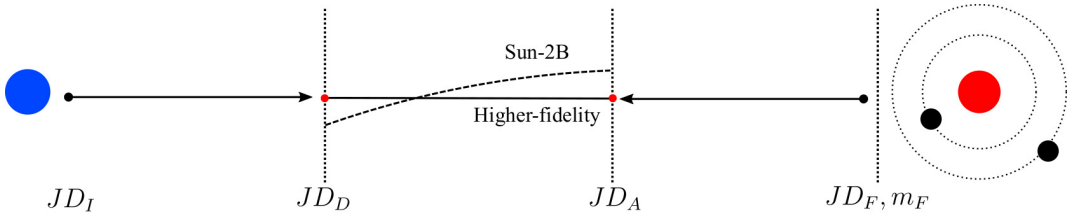

(c) Reconverging Phase 2

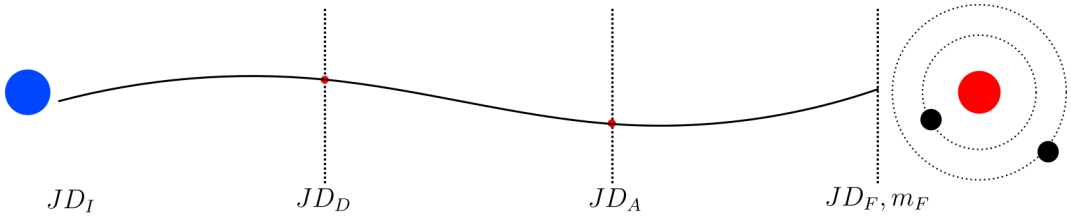

(d) Reconverging Phase 1 through 3

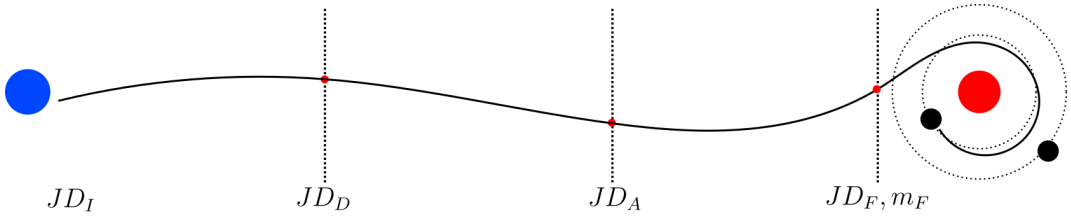

(e) Reconverging Phase 4

Figure 6.1. The steps of constructing an end-to-end trajectory

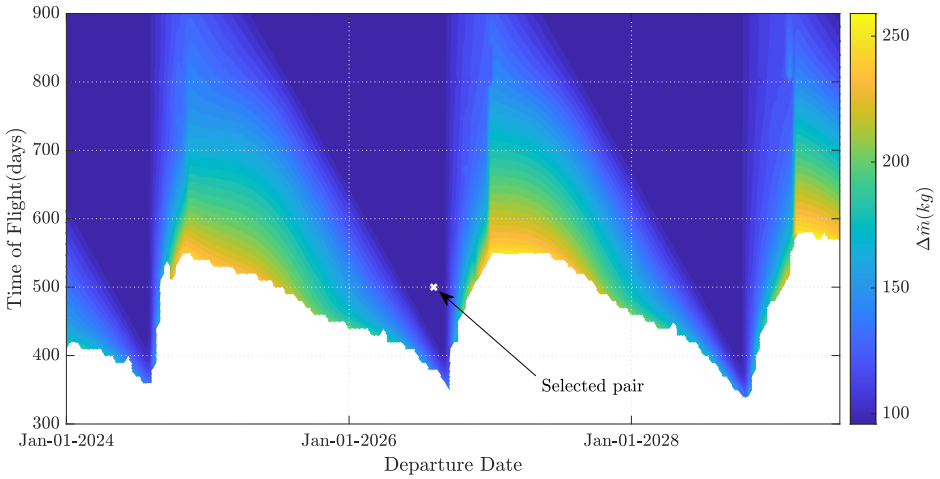

(a) Selected pair of epochs from the contour plot

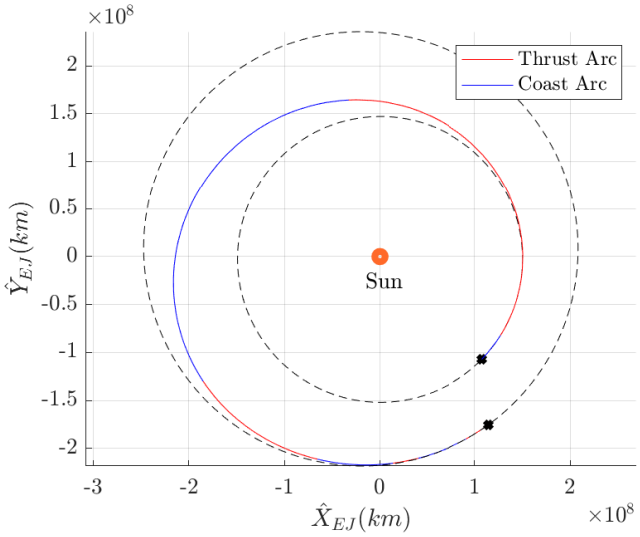

(b) Selected heliocentric leg in the Sun-centered ECLIPJ2000 frame

Figure 6.2. The selected pair of epochs and the corresponding heliocentric leg

6.1.2 Generating Phase 1 and 3 Trajectories

The heliocentric leg plotted in Figure 6.2(b) is generated between the exact states of the planets in the heliocentric space, also denoted the rendezvous condition. Under this strategy, it is impossible to incorporate the gravity of the Earth and Mars as the trajectory coincides with the planetary states at both end points. Thus, realistic planetocentric spiral arcs must be computed, between which the heliocentric leg is generated again within the higher-fidelity model. These arcs correspond to Phase 1 and Phase 3 according to the multi-phase formulation of the current investigation, illustrated in Figure 1.1. These arcs are generated via simple control laws, following the assumptions in Table 1.1.

For Phase 1, or the spiral arc that departs from the Earth, a velocity-aligned control law is utilized. However, it is first necessary to define the exact state of the spacecraft upon the departure along the initial orbit. The current work assumes the departure from a GTO, where the definition of the specific GTO utilized is introduced in Table 6.1, where the orbital elements are computed with respect to the J2000 frame. The set of values corresponds to a GTO with an apogee at the geostationary orbit (35,622 km altitude) and a perigee at 1,000 km altitude which appears in a relevant work by Ojeda Romero and Howell [92]. Note that the the orbital plane of the GTO coincides with the mean Earth equator plane as plotted in Figure 6.3 in the Earth-centered J2000 frame. It is further assumed that the spacecraft departs from the perigee of the GTO, illustrated as the red point in the same figure. With this assumption, the position and velocity at the beginning of Phase 1 is parameterized as a function of JD_I, or the initial epoch at the GTO departure. Note that the initial mass is not a function of time, and is fixed as 409.8 kg, following the value from Table 1.2. Given a JD_I value, the initial state is fully determined and Phase 1 arc is computed by propagating the differential equations from the dynamical model, the higher-fidelity ephemeris model. The thrust magnitude is fixed at the maximum value, and the direction is aligned with the direction of the velocity in the Sun-Earth CR3BP rotating frame. The duration of the propagation is given as the time difference between JD_D and JD_I. Thus, the end state of Phase 1, under the current formulation, only depends on JD_I which needs to be properly selected. Recall that the contour plot in Figure 6.2(a) is generated with an assumption that

the gravity of the Earth is ignored at the beginning of the heliocentric arc. This escape condition is enforced at JD_D, or at the interface point between Phase 1 and 2 to find a suitable initial epoch, JD_I. To this end, the end state of Phase 1 is obtained in the Earth-centered ECLIPJ2000 frame. The position and velocity magnitude are computed as $\tilde{R}_E$ and $\tilde{V}_E$. Then, the escape condition is equal to the following equation,

$$\tilde{V}_{inf,E}^2 = 2(\frac{\tilde{V}_E^2}{2} - \frac{\tilde{G}\tilde{m}_E}{\tilde{R}_E}) = 0, \tag{6.1}$$

where $\tilde{V}_{inf,E}$ is also denoted the Earth-2BP excess velocity and $\tilde{m}_E$ corresponds to the mass of the Earth. The value of JD_I that satisfies Equation (6.1) after propagating for $JD_D - JD_I$ is found by a differential corrector. The corresponding spiral arc around the Earth is plotted in Figure 6.4, where the end of the Phase 1 is associated with the selected JD_D, and corresponding states for position, velocity and mass define the beginning of the heliocentric leg, or Phase 2. The spiral arc around the Earth is also represented as a black arrow from the Earth in Figure 6.1(b), where the red dot corresponds to the end of Phase 1 but also the beginning of Phase 2.

For Phase 3, or the Mars-centered spiral arc, a similar process is repeated. From Chapter 5, it is assumed that the spacecraft arrives at one of the Deimos science orbits listed in Table 5.3. Here, for the demonstrative purpose, 5:4 MD-RO is selected, but the same process applies to the other science orbits as well. For simplicity, the arrival state along the science orbit is assumed to be the apoapsis from Mars. Then, it only requires two additional inputs to specify the arrival state: the final epoch, JD_F, and the final mass, $\tilde{m}_F$, upon the arrival at the Deimos science orbit. The largest difference between Phase 1 and 3 is the mass. While at the beginning of Phase 1, the mass is fixed as the initial value of the spacecraft, the mass value at the end of Phase 3 is not known a priori as it depends on Phase 1 and 2. Thus, the final state of Phase 3 is a function of two variables that must be selected: JD_F and also $\tilde{m}_F$. For a preliminary analysis, it is first assumed that $\tilde{m}_F$ is 95% of the mass value corresponding to the end state of heliocentric leg in Figure 6.2(b). Then, provided a value for JD_F, the arrival state along 5:4 MD-RO is fully determined and is back propagated for $JD_F - JD_A$, or the time difference between the arrival epoch of the heliocentric leg and the final epoch.

The thrust magnitude is fixed at the maximum available value, while the direction is in the opposite direction of the velocity in the Sun-Mars CR3BP rotating frame. At the interface point between Phase 2 and 3, it is desired that the spacecraft escapes the Martian gravity, or,

$$\tilde{V}_{inf,M}^2 = 2(\frac{\tilde{V}_M^2}{2} - \frac{\tilde{G}\tilde{m}_M}{\tilde{R}_M}) = 0, \tag{6.2}$$

where the subscript M refers to the values are computed with respect to Mars. $\tilde{R}_M$ and $\tilde{V}_M$ correspond to the inertial position and velocity magnitudes in the Mars-centered ECLIPJ2000 frame. The value of JD_F is iteratively searched such that at the end of the back propagation, or at the beginning of Phase 3, Equation (6.2) is satisfied. The computed spiral arc around Mars is illustrated in Figure 6.5, in the Sun-Mars CR3BP rotating frame. It is also represented as the black arrow originating from the Martian system in Figure 6.1(b), where the direction of propagation is in reverse time.

Table 6.1. The orbital parameters of the Earth GTO

Orbital Parameters	a_K [km]	e_K [n.d.]	ω_K [°]	i_K [°]
Values	$2.4689 \times 10^4 km$	0.70116	0	0

6.1.3 Reconverging Phase 2

The heliocentric leg is solved again utilizing the new boundary points linked to the planetocentric spiral arcs. The heliocentric leg computed in the Sun-2BP, plotted in Figure 6.2(b), is utilized as an initial guess of its counterpart in the higher-fidelity ephemeris model. This is illustrated in Figure 6.1(b), where the dotted line corresponds to the solution for Phase 2 computed in the Sun-2BP. The solution in the Sun-2BP is computed again in the ephemeris model to link the boundary points of the spiral arcs while optimizing for the maximum mass value at the end of the heliocentric leg. Note that between Phase 1 and 2, the state and epoch continuity is achieved. However, between Phase 2 and 3, the position, velocity and epoch continuity is obtained but the mass is discontinuous in general. From Phase 2, the mass value at the interface point is an optimized variable and cannot be exactly

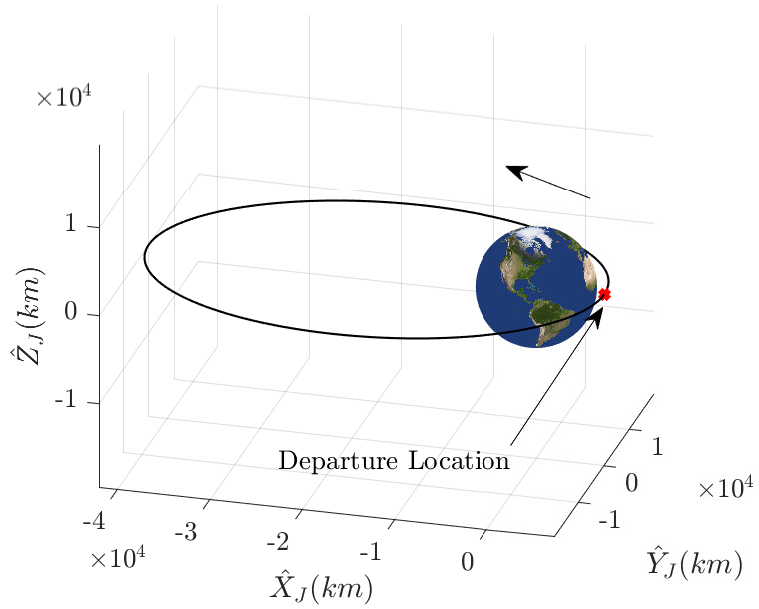

Figure 6.3. The GTO and the departure location (Earth-centered J2000 frame view)

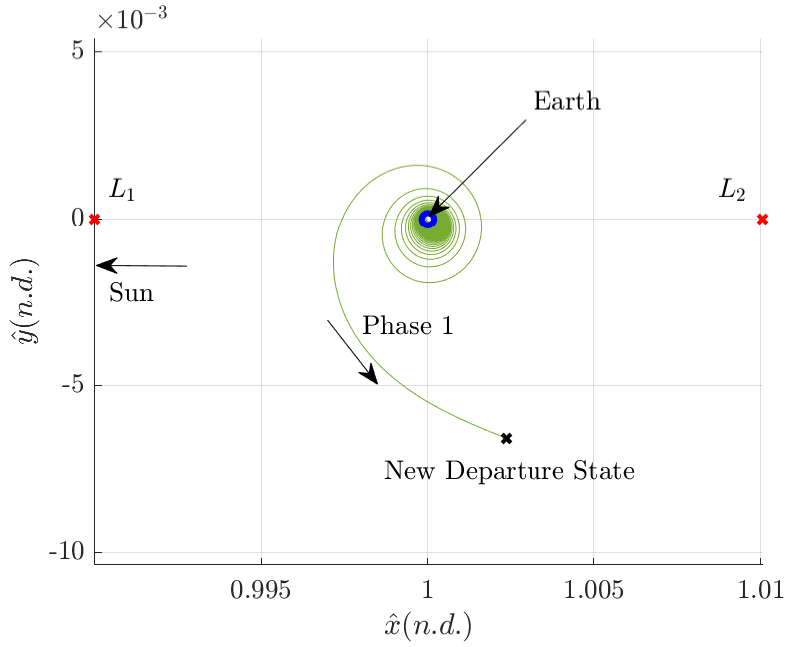

Figure 6.4. Phase 1 and the new departure state for Phase 2 (Sun-Earth CR3BP rotating frame view)

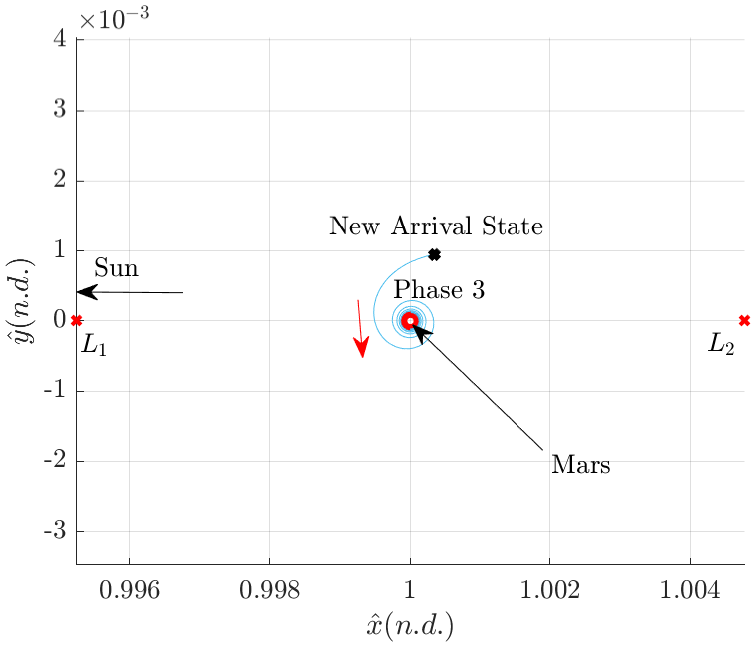

Figure 6.5. Phase 3 and the new arrival state for Phase 2 (Sun-Mars CR3BP rotating frame view)

targeted, and from Phase 3, the value depends on $\tilde{m}_F$. This discontinuity necessitates the next step.

6.1.4 Reconverging Phase 1 through 3

As the computed trajectory involves the discontinuity in mass at the interface point between Phase 2 and 3, the problem is solved again as a whole for continuity. The planetocentric spiral arcs are parameterized by three variables. JD_I fully determines Phase 1 arc, whereas JD_F and $\tilde{m}_F$ determine the Phase 3. A differential corrector is employed to search for these three variables while simultaneously solving for a feasible heliocentric leg, Phase 2, such that the continuity of state end epoch is achieved at the interface points. This step is illustrated in Figure 6.1(d), where now the trajectory is continuous at all locations throughout Phase 1, 2, and 3. Note that the resulting trajectory is suboptimal, due to the assumptions in generating the planetocentric arcs, i.e., simple control laws are employed and the solution space explored by the optimizer is restricted. Although it is possible to further optimize the result, since the planetocentric arcs involve multiple revolutions around the planets, it is observed that only little improvements are achieved while requiring long computation times. Instead, the Phase 1 and 3 can be discretized and incorporated into the direct collocation scheme, but this approach remains out of the scope of the current investigation.

6.1.5 Computing Phase 4

The state of the spacecraft at the interface point between Phase 3 and 4 is retrieved. Utilizing this value as well as the final epoch, JD_F, the tour trajectory between the Martian moons, Phase 4, is computed. The method is explained in Chapter 5, where the results are plotted in Figure 5.20 for the scenario between 5:4 MD-RO and the Phobos capture orbit. It is possible that the spacecraft stays in the Deimos science orbit to achieve multiple Deimos flybys. In this case, the epoch at the beginning of Phase 4 does not coincide with JD_F. For the example result, it is assumed that the spacecraft leaves the Deimos science orbit as soon as the spacecraft arrives at 5:4 MD-RO.

6.2 Results

The obtained end-to-end trajectory is illustrated in Figure 6.6 utilizing different coordinate frames. Figure 6.6(a) illustrates the position of the spacecraft along the trajectory in the Sun-centered ECLIPJ2000 frame. Note that the transfer also has spatial components, but it is represented in the $\hat{X}_{EJ} - \hat{Y}_{EJ}$ plane. The different colors represent the trajectories corresponding to each phase. Compared to the heliocentric leg plotted in Figure 6.2(b), the end-to-end trajectory is much longer as it incorporates the other phases before and after the heliocentric leg. Figure 6.6(b) illustrates the vicinity of the Earth in the Sun-Earth CR3BP rotating frame, where the Phase 1 arc spirals out from the GTO and is linked to the Phase 2 arc at JD_D. Similarly, trajectory in the vicinity of Mars is plotted in Figure 6.6(c) where the Phase 2 arc is interfaced with Phase 3 arc at JD_A. The views of the tour trajectory are available when this plot is further zoomed in near Mars, as in Figure 6.6(d). JD_F denotes the interface point between Phase 3 and 4. When the Phase 4 trajectory is rotated, the geometry of the tour of the moons becomes more apparent as illustrated in Figure 5.20.

The corresponding costs, measured as the consumed propellant, equivalent delta-V, and time of flight, are listed in Table 6.2. These values are bound to the assumptions listed in Table 1.1 as well as the selected pair of the epochs and the Deimos science orbit. It is noted that the propellant consumption for the heliocentric leg, or Phase 2, decreased compared to the Sun-2B solution as the optimizer leverages the gravity of the planets. Next to the heliocentric leg, the spiral arc around the Earth accounts for the most significant amount of propellant consumption as well as the time of flight. Similar mission scenarios where the spacecraft departs from a GTO requires corresponding propellant and/or time of flight to escape the Earth's gravity.

Table 6.2. The costs of the sample end-to-end trajectory

	$\tilde{m}$ [kg]	$\Delta\tilde{V}$ [km]	Time of flight [days]
Phase 1	81.4	3.766	178
Phase 2	86.2	5.180	500
Phase 3	12.5	0.900	27
Phase 4	9.4	0.714	26
Total	189.6	10.559	732

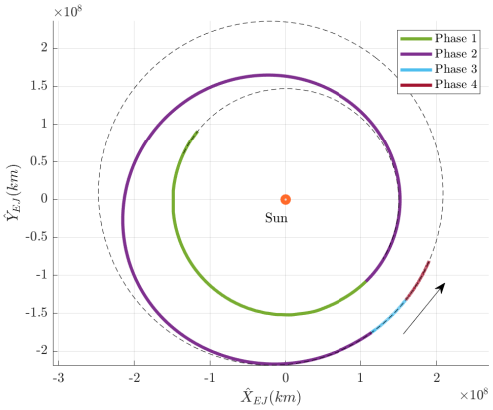

(a) Sun-centered ECLIPJ2000 frame view

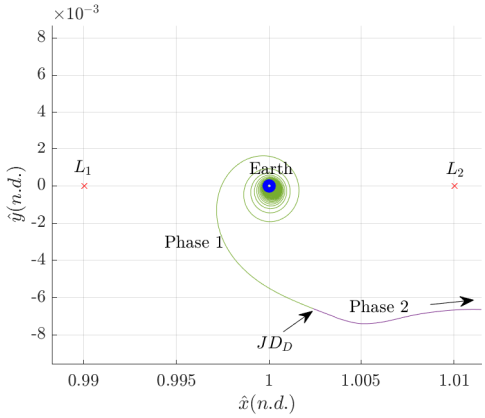

(b) Sun-Earth CR3BP rotating frame view

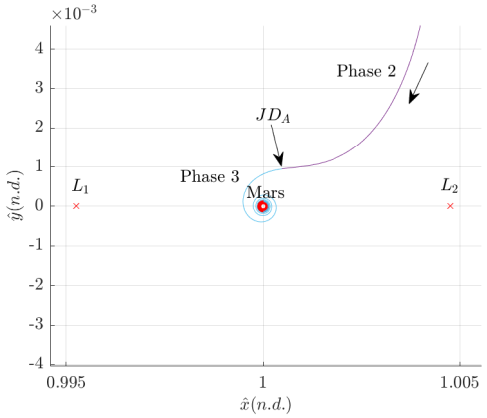

(c) Sun-Mars CR3BP rotating frame view

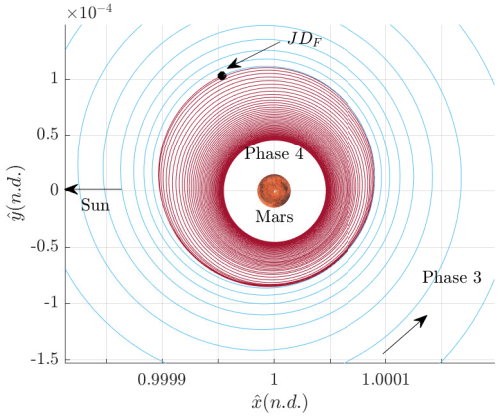

(d) Sun-Mars CR3BP rotating frame view (Zoomed-in)

Figure 6.6. Sample end-to-end trajectory in differnt coordinate frames

7. CONCLUSIONS

7.1 Investigation Summary

While the interest in the exploration of the Martian moons increases, the low-thrust propulsion technology enables novel mission scenarios with smaller spacecrafts. The current investigation focuses on the trajectory design challenges associated with one of such scenarios, where a spacecraft departs from a GTO and finally explores both Martian moons utilizing a low-thrust engine. The low-thrust trajectory design problem is set up within a multi-phase framework, where simplifications are introduced to focus on the heliocentric leg (Phase 2) and the tour of the Martian moons (Phase 4). Design challenges associated with these phases are defined and solved independently. Initial guesses are generated within two types of lower-fidelity models, two-body problem (2BP) and the circular restricted three body problem (CR3BP). Then, the direct collocation algorithm is utilized to obtain feasible as well as optimal trajectories. Finally, the results from each phase are combined to a end-to-end trajectory in the higher-fidelity ephemeris model, proving the validity of the framework.

7.1.1 Heliocentric Leg Design (Phase 2)

The heliocentric leg, or the transfer trajectory between the Earth and Mars in the heliocentric space, accounts for a considerable amount of propellant consumption and needs to be properly characterized. As the states of the planets in the heliocentric space are time-dependent, multiple optimal control problems are constructed over a grid of the departure epoch and the time of flight, in the Sun-2BP model. While the boundary constraints of the problems consist of the planetary states obtained via the ephemerides, two initial guess generation strategies that involve polynomial approximation and a continuation scheme are provided. A contour plot is generated from the optimized trajectories over the grid to characterize the heliocentric leg; the trend of propellant consumption over different relative configurations of the planets is efficiently captured.

7.1.2 Martian Moons Tour Design (Phase 4)

The structure of the tour of the Martian moons is discussed, where Deimos is visited first prior to Phobos, considering the energy of the moons in the Sun-Mars CR3BP. The science orbits for the moons are selected based on the capture and flyby exploration opportunities they grant. The tour scenarios are then divided into (1) capture to flyby, (2) flyby to capture and (3) capture to capture, and the transfer trajectories between the science orbits of the moons are generated for each specific scenario. The main challenge for the transfer trajectory design is the presence of the terminal rendezvous constraint between the spacecraft and the Phobos science orbit while involving multiple revolutions of spiral arcs around Mars. To address this challenge, a strategy that combines an initial guess generated via the Q-law algorithm and the direct collocation algorithm is developed and explained. The proposed strategy succeeds in obtaining transfer trajectories for all the investigated scenarios, and the reference costs are generated assuming a set of spacecraft parameters. To better estimate the costs associated with each scenario, the arrival costs from the heliocentric space to each Deimos science orbit are included as well, generated with an anti-velocity control law (Phase 3).

7.1.3 End-to-End Trajectory Design (Phase 1 - 4)

The results obtained separately for Phase 2 and 4 are combined to generate an end-to-end trajectory within a higher-fidelity ephemeris model. The steps of such process are provided along with an illustrative example. First, a pair of departure and arrival epochs of the heliocentric leg are selected. Planetocentric spiral arcs, corresponding to Phase 1 and 3, are incorporated to update the end points of the heliocentric leg. From the Earth's side, a velocity-aligned control law is employed to escape the gravity field of the Earth, assuming departure from an initial state along a GTO. Similarly, an anti-velocity control law is employed to back propagate a spacecraft state along a Deimos science orbit until the spacecraft escapes the gravity of Mars. Then, the trajectories for Phase 1 through 3 are combined to be solved for a feasible solution, i.e., the position, velocity, mass, and the epoch along the trajectory are continuous. And based on the final values of the Phase 3, the

tour of the Martian moons, or Phase 4, is generated and completes the end-to-end trajectory design. Although the resulting trajectory remains suboptimal, the validity of the multi-phase framework proposed in the current investigation is confirmed via the end-to-end trajectory.

7.2 Recommendations for Future Work

This research effort proposes a multi-phase framework for the Earth to Martian moons low-thrust trajectory design. Many avenues for future research are apparent, mainly related to removing the simplifying assumptions introduced in the current work.

7.2.1 Low-Thrust Design Factors

The current analysis is bound to the low-thrust design factors listed in Table 1.1. The numbers provided in the current investigation correspond to a potential mission scenario with departure from a GTO, while different departure scenario would introduce different sets of values for the spacecraft numbers as well as the initial state. For the future work, it is necessary to validate the multi-phase framework with the alternative scenarios to compare the results. These scenarios include, but are not limited to, launch as a secondary payload on interplanetary and cislunar missions.

7.2.2 Higher-Fidelity Analysis

The results of the current investigation may be validated within a more realistic model. From an operational aspect, the low-thrust engine cannot provide thrust when the eclipse occurs, or when the planets block the line-of-sight between the spacecraft and the Sun. It is possible to update the direct collocation algorithm to detect the eclipse regions and enforce the no-thrust constraint. Also, while the current analysis assumes that a constant amount of power is available throughout the whole trajectory, it can be treated as a variable quantity that mainly depends on the distance of the spacecraft from the Sun. And the rest of the engine parameters, including the maximum thrust and the specific impulse, will also be a function of the available power. Finally, all the celestial bodies are assumed to be centrobaric

in the current work, but this assumption can be reconsidered in the vicinity of the planets to incorporate the precise geopotential models.

7.2.3 Planetocentric Spiral Trajectories (Phase 1 and 3)

Phase 1 and 3, corresponding to the departure from the Earth and arrival at Mars, respectively, are generated with simple control laws in the current investigation. For a more complete analysis, the trade-off between the time of flight and propellant consumption for the arcs must be analyzed. Either a parametrized model [22] or fully discretized model of the spiral arcs [87] can be utilized to navigate the trade-off relationship. And the knowledge about the relationship can be leveraged to further optimize the end-to-end trajectory to locate a solution associated with desirable costs: time of flight and propellant consumption.

7.2.4 Low-Energy Transfers for the Heliocentric Leg (Phase 2)

The Sun-2BP is mainly utilized for the the characterization of heliocentric leg in the current investigation. Previous authors introduce low-energy transfers between the Earth and Mars where the gravity of the Sun and the planets are considered together to produce propellant-efficient trajectories [93], [94]. Future studies may involve exploiting dynamical structures in the multi-body dynamics regime to characterize low-energy transfers between the Earth and Mars.

7.2.5 Different Martian Moons Science Orbits (Phase 4)

Different science orbits may be considered when specific science requirements are imposed to a potential mission. These may include, but are not limited to, the minimum altitude constraint from the moons, a window for observation of the surface, and the required stationkeeping maneuver for the spacecraft to stay within the orbit. The currently introduced strategy for the tour of the Martian moons may be then validated with various science orbits.

REFERENCES

[1] S. L. Murchie, D. T. Britt, and C. M. Pieters, "The Value of Phobos Sample Return," *Planetary and Space Science*, vol. 102, no. C, pp. 176–182, 2014. DOI: 10.1016/j.pss.2014.04.014.

[2] T. Usui, K. Bajo, W. Fujiya, Y. Furukawa, M. Koite, Y. N. Miura, H. Sugahara, S. Tachibana, Y. Takano, and K. Kuramoto, "The Importance of Phobos Sample Return for Understanding the Mars-Moon System," *Space Science Reviews*, vol. 216, no. 4, 2020. DOI: 10.1007/s11214-020-00668-9.

[3] S. S. Board, N. R. Council, *et al.*, *Vision and Voyages for Planetary Science in the Decade 2013-2022*. National Academies Press, 2012.

[4] G. A. Landis, "Teleoperation from Mars Orbit: a Proposal for Human Exploration," *Acta Astronautica*, vol. 62, no. 1, pp. 59–65, 2008. DOI: 10.1016/j.actaastro.2006.12.049.

[5] K. D. Pang, J. B. Pollack, J. Veverka, A. L. Lane, and J. M. Ajello, "The Composition of Phobos: Evidence for Carbonaceous Chondrite Surface from Spectral Analysis," *Science (American Association for the Advancement of Science)*, vol. 199, no. 4324, pp. 64–66, 1978.

[6] O. Witasse, T. Duxbury, A. Chicarro, N. Altobelli, T. Andert, A. Aronica, S. Barabash, J.-L. Bertaux, J.-P. Bibring, A. Cardesin-Moinelo, *et al.*, "Mars Express Investigations of Phobos and Deimos," *Planetary and Space Science*, vol. 102, pp. 18–34, 2014.

[7] B. G. Drake, S. J. Hoffman, and D. W. Beaty, "Human Exploration of Mars, Design Reference Architecture 5.0," in *2010 IEEE Aerospace Conference*, Big Sky, Montana, 2010.

[8] A. C. Muscatello, R. P. Mueller, G. B. Sanders, and W. E. Larson, "Phobos and Deimos Sample Collection and Prospecting Missions for Science and ISRU," in *Concepts and Approaches for Mars Exploration*, Houston, Texas, 2012.

[9] R. Sagdeev and A. Zakharov, "Brief History of the Phobos Mission," *Nature*, vol. 341, no. 6243, pp. 581–585, 1989.

[10] S. Barraclough, A. Ratcliffe, R. Buchwald, H. Scheer, M. Chapuy, M. Garland, and D. Rebuffat, "Phootprint: a European Phobos Sample Return Mission," in *11th International Planetary Probe Workshop*, vol. 1795, 2014, p. 8030.

[11] P. Lee, M. Benna, and D. Britt, "PADME (Phobos and Deimos and Mars Environment): A Proposed NASA Discovery Mission to Investigate the Two Moons of Mars.," in *46th Lunar and Planetary conference*, 2015.

[12] C. A. Raymond, S. Diniega, and T. H. Prettyman, "Pandora-Discovering the Origin of the Moons of Mars (a Proposed Discovery Mission)," in *AGU Fall Meeting Abstracts*, vol. 2015, 2015, P11B–2101.

[13] M. Fujimoto, H. Miyamoto, K. Kuramoto, and the MMX Science Board members, "JAXA's Martian Moons eXploration, MMX," in *European Planetary Science Congress*, 2017.

[14] M. Zamaro and J. D. Biggs, "Identification of New Orbits to Enable Future Mission Opportunities for the Human Exploration of the Martian Moon Phobos," *Acta Astronautica*, vol. 119, pp. 160–182, 2016. DOI: https://doi.org/10.1016/j.actaastro.2015.11.007.

[15] M. D. Rayman, P. A. Chadbourne, J. S. Culwell, and S. N. Williams, "Mission Design for Deep Space 1: a Low-Thrust Technology Validation Mission," *Acta Astronautica*, vol. 45, no. 4-9, pp. 381–388, 1999.

[16] H. Kuninaka, K. Nishiyama, Y. Shimizu, I. Funaki, H. Koizumi, S. Hosoda, and D. Nakata, "Hayabusa Asteroid Explorer Powered by Ion Engines on the Way to Earth," in *31st International Electric Propulsion Conference*, Ann Arbor, Michigan, 2009.

[17] C. R. Koppel and D. Estublier, "The SMART-1 Hall Effect Thruster around the Moon: In Flight Experience," in *29th International electric propulsion conference*, Princeton, New Jersey, 2005.

[18] C. Russell, F. Capaccioni, A. Coradini, M. De Sanctis, W. Feldman, R. Jaumann, H. Keller, T. McCord, L. McFadden, S. Mottola, *et al.*, "Dawn Mission to Vesta and Ceres," *Earth, Moon, and Planets*, vol. 101, no. 1-2, pp. 65–91, 2007.

[19] D. Lev, R. M. Myers, K. M. Lemmer, J. Kolbeck, H. Koizumi, and K. Polzin, "The Technological and Commercial Expansion of Electric Propulsion," *Acta Astronautica*, vol. 159, no. November 2018, pp. 213–227, 2019. DOI: 10.1016/j.actaastro.2019.03.058.

[20] N. Barba, T. Komarek, R. Woolley, L. Giersch, V. Stamenkovic, M. Gallagher, and C. D. Edwards, "Mars Small Spacecraft Studies: Overview," *IEEE Aerospace Conference*, 2019. DOI: 10.1109/AERO.2019.8741735.

[21] S. Tardivel, A. T. Klesh, and S. Campagnola, "Technology Enabling Interplanetary Trajectories for Nanospacecraft," *Journal of Spacecraft and Rockets*, vol. 55, no. 1, pp. 95–105, 2018. DOI: 10.2514/1.A33789.

[22] R. Woolley and Z. Olikara, "Optimized Low-Thrust Missions from GTO to Mars," in *IEEE Aerospace Conference*, 2019. DOI: 10.1109/AERO.2019.8741558.

[23] G. Genta and P. F. Maffione, "A Graphical Tool to Design Two-Ways Human Mars Missions," *Acta Astronautica*, vol. 154, pp. 301–310, 2019. DOI: 10.1016/j.actaastro.2018.03.035.

[24] M. T. Ozimek, "Low-Thrust Trajectory Design and Optimization of Lunar South Pole Coverage Missions," Ph.D. Dissertation, Purdue University, West Lafayette, Indiana, May 2010.

[25] B. Prado Pino, R. Pritchett, K. C. Howell, and D. C. Folta, "Extended Mission Options for the Lunar IceCube Low-Thrust Spacecraft by Leveraging the Dynamical Environment," in *71st International Astronautical Congress*, The CyberSpace Edition, 2020.

[26] R. Pritchett, K. Howell, and D. Folta, "Low-Thrust Trajectory Design for a Cislunar Cubesat Leveraging Structures from the Bicircular Restricted Four-Body Problem," in *70th International Astronautical Congress*, Washington, D.C., 2019.

[27] G. J. Whiffen and T. Lam, "The Jupiter Icy Moons Orbiter Reference Trajectory," in *AAS/AIAA Space Flight Mechanics Meeting*, Tampa, Florida, 2006.

[28] P. A. Penzo, *Planetary Missions from GTO Using Earth and Moon Gravity Assists*. 1998. [Online]. Available: https://trs.jpl.nasa.gov/bitstream/handle/2014/19526/98-0946.pdf?sequence=1.

[29] J. M. Longuski and S. N. Williams, "Automated Design of Gravity-Assist Trajectories to Mars and the Outer Planets," *Celestial Mechanics and Dynamical Astronomy*, vol. 52, no. 3, pp. 207–220, 1991.

[30] P. Ghosh, "A Survey of the Methods Available for the Design of Many-Revolution Low-Thrust Planetocentric Trajectories," in *29th AAS/AIAA Space Flight Mechanics Meeting*, 2019.

[31] A. E. Petropoulos, Z. B. Tarzi, G. Lantoine, T. Dargent, and R. Epenoy, "Techniques for Designing Many-Revolution, Electric-Propulsion Trajectories," in *24th AAS/AIAA Space Flight Mechanics Meeting*, Santa Fe, New Mexico, 2014.

[32] S. Tang and B. A. Conway, "Optimization of Low-Thrust Interplanetary Trajectories Using Collocation and Nonlinear Programming," *Journal of Guidance, Control, and Dynamics*, vol. 18, no. 3, pp. 599–604, 1995.

[33] A. L. Herman and B. A. Conway, "Direct Optimization Using Collocation Based on High-Order Gauss-Lobatto Quadrature Rules," *Journal of Guidance, Control, and Dynamics*, vol. 19, no. 3, pp. 592–599, 1996.

[34] A. V. Rao, "A Survey of Numerical Methods for Optimal Control," *Advances in the Astronautical Sciences*, vol. 135, no. 1, pp. 497–528, 2009.

[35] M. Ozimek, D. Grebow, and K. Howell, "Design of Solar Sail Trajectories with Applications to Lunar South Pole Coverage," *Journal of guidance, control, and dynamics*, vol. 32, no. 6, pp. 1884–1897, 2009.

[36] N. L. Parrish, J. S. Parker, S. P. Hughes, and J. Heiligers, "Low-Thrust Transfers from Distant Retrograde Orbits to L2 Halo Orbits in the Earth-Moon System," in *6th International Conference on Astrodynamics Tools and Techniques*, 2016, pp. 14–17.

[37] R. Pritchett, K. Howell, and D. Grebow, "Low-thrust Transfer Design Based on Collocation Techniques: Applications in the Restricted Three-Body Problem," *Advances in the Astronautical Sciences*, vol. 162, pp. 299–318, 2018.

[38] R. C. Woolley, F. Laipert, A. K. Nicholas, and Z. Olikara, "Low-thrust Trajectory Bacon Plots for Mars Mission Design," *Advances in the Astronautical Sciences*, vol. 168, pp. 2833–2846, 2019.

[39] J. A. Sims, P. A. Finlayson, E. A. Rinderle, M. A. Vavrina, and T. D. Kowalkowski, "Implementation of a Low-Thrust Trajectory Optimization Algorithm for Preliminary Design," in *AIAA/AAS Astrodynamics Specialist Conference and Exhibit*, 2006. DOI: 10.2514/6.2006-6746.

[40] P. E. Gill, W. Murray, and M. A. Saunders, "SNOPT: An SQP Algorithm for Large-Scale Constrained Optimization," *SIAM review*, vol. 47, no. 1, pp. 99–131, 2005.

[41] G. Genta and P. F. Maffione, "Comparison between Different Approaches to Interplanetary Mission Design," *International Journal of Signal Processing*, vol. 2, pp. 54–66, 2017.

[42] B. Dachwald, "Optimization of Very-Low-Thrust Trajectories Using Evolutionary Neurocontrol," *Acta Astronautica*, vol. 57, no. 2-8, pp. 175–185, 2005.

[43] F. Cremaschi, F. Topputo, G. Sangiovanni, and M. Vasile, "Low Thrust Interplanetary Transfers through Invariant Manifolds and an Evolutionary Neurocontrol," *Proceedings of the XVIII Congresso Nazionale AIDAA*, 2005.

[44] U. Derz, A. Ohndorf, and B. Bischof, "Mission Analysis of Robotic, Low Thrust Missions to the Martian Moons Deimos and Phobos," in *62nd International Astronautical Congress*, 2011.

[45] G. Lantoine and R. P. Russell, "A Hybrid Differential Dynamic Programming Algorithm for Constrained Optimal Control Problems. Part 2: Application," *Journal*

of Optimization Theory and Applications, vol. 154, no. 2, pp. 418–442, 2012. DOI: 10.1007/s10957-012-0038-1.

[46] J. D. Aziz, "Low-Thrust Many-Revolution Trajectory Optimization," Ph.D. dissertation, University of Colorado Boulder, Boulder, Colorado, 2018.

[47] E. ZhiBo and D. Guzzetti, "Multi-Revolution Low-Thrust Trajectory Optimization Using Symplectic Methods," *Science China Technological Sciences*, vol. 63, no. 3, pp. 506–519, 2020, ISSN: 1862281X. DOI: 10.1007/s11431-019-9511-7.

[48] A. E. Petropoulos, "Low-Thrust Orbit Transfers Using Candidate Lyapunov Functions with a Mechanism for Coasting," in *AIAA/AAS Astrodynamics Specialist Conference*, 2004.

[49] D. A. Vallado, *Fundamentals of Astrodynamics and Applications*. Springer Science & Business Media, 2001, vol. 12.

[50] C. Acton, N. Bachman, B. Semenov, and E. Wright, "A look towards the Future in the Handling of Space Science Mission Geometry," *Planetary and Space Science*, vol. 150, pp. 9–12, 2018.

[51] E. M. Standish Jr, "Orientation of the JPL Ephemerides, DE 200/LE 200, to the Dynamical Equinox of J2000," *Astronomy and Astrophysics*, vol. 114, pp. 297–302, 1982.

[52] P. K. Seidelmann, *Explanatory Supplement to the Astronomical Almanac*. University Science Books, 2006.

[53] B. V. Semenov. (Feb. 1, 2017). "Reference Frames," [Online]. Available: https://naif.jpl.nasa.gov/pub/naif/toolkit_docs/C/req/frames.html (visited on 02/05/2021).

[54] C. Ocampo, "An Architecture for a Generalized Spacecraft Trajectory Design and Optimization System," *Libration Point Orbits and Applications*, pp. 529–571, 2003. DOI: 10.1142/9789812704849_0023.

[55] A. D. Cox, "A Dynamical Systems Perspective for Preliminary Low-thrust Trajectory Design in Multi-body Regimes," Ph.D. dissertation, Purdue University, West Lafayette, Indiana, 2020.

[56] V. Muralidharan, "Orbit Maintenance Strategies for Sun-Earth/Moon Libration Point Missions: Parameter Selection for Target Point and Cauchy-Green Tensor Approaches," M.S. thesis, Purdue University, West Lafayette, Indiana, 2017.

[57] J. T. Betts, "Survey of Numerical Methods for Trajectory Optimization," *Journal of guidance, control, and dynamics*, vol. 21, no. 2, pp. 193–207, 1998.

[58] F. Topputo and C. Zhang, "Survey of Direct Transcription for Low-Thrust Space Trajectory Optimization with Applications," *Abstract and Applied Analysis*, vol. 2014, 2014. DOI: 10.1155/2014/851720.

[59] B. A. Conway, *Spacecraft Trajectory Optimization*. Cambridge University Press, 2010, vol. 29.

[60] R. E. Pritchett, "Strategies for Low-Thrust Transfer Design Based on Direct Collocation Techniques," Ph.D. Dissertation, Purdue University, West Lafayette, Indiana, 2020.

[61] A. Iserles, *A First Course in the Numerical Analysis of Differential Equations*, 44. Cambridge university press, 2009.

[62] D. J. Grebow and T. A. Pavlak, *AMMOS Report on Collocation Methods*. Pasadena, California: Jet Propulsion Laboratory, Califormia Institute of Technology, 2015, pp. 1–20.

[63] J. M. Longuski, J. J. Guzmán, and J. E. Prussing, *Optimal Control with Aerospace Applications*. Springer, 2014.

[64] T. Coleman, M. A. Branch, and A. Grace, "Optimization Toolbox," *For Use with MATLAB. User's Guide for MATLAB 5, Version 2, Release II*, 1999.

[65] A. Wächter and L. T. Biegler, "On the Implementation of an Interior-Point Filter Line-Search Algorithm for Large-Scale Nonlinear Programming," *Mathematical programming*, vol. 106, no. 1, pp. 25–57, 2006.

[66] M. A. Patterson and A. V. Rao, "GPOPS-II: A MATLAB Software for Solving Multiple-Phase Optimal Control Problems Using hp-Adaptive Gaussian Quadrature Collocation Methods and Sparse Nonlinear Programming," *ACM Transactions on Mathematical Software (TOMS)*, vol. 41, no. 1, pp. 1–37, 2014.

[67] B. Prado Pino and K. C. Howell, "An Energy-Informed Adaptive Algorithm for Low-Thrust Spacecraft Cislunar Trajectory Design," in *AAS/AIAA Astrodynamics Specialist Conference*, 2020.

[68] L. M. Burke, R. Falck, and M. Mcguire, *Interplanetary Mission Design Handbook: Earth-to-Mars Mission Opportunities 2026 to 2045*. Washington, D.C.: NASA, 2010.

[69] R. Potter, R. Woolley, A. Nicholas, and J. Longuski, "Features and Characteristics of Earth-Mars Bacon Plots," *Advances in the Astronautical Sciences*, vol. 162, pp. 3799–3817, 2018.

[70] P. R. Patel, A. D. Gallimore, T. H. Zurbuchen, and D. J. Scheeres, "An Algorithm for Generating Feasible Low Thrust Interplanetary Trajectories," in *International Electric Propulsion Conference*, 2009.

[71] A. A. Wolf, "Touring the Saturnian system," *The Cassini-Huygens Mission*, pp. 101–128, 2003.

[72] S. D. Ross, W. S. Koon, M. W. Lo, and J. E. Marsden, "Design of a Multi-Moon Orbiter," in *AAS/AIAA Space Flight Mechanics Meeting*, 2003.

[73] J. A. Sims, "Jupiter Icy Moons Orbiter Mission Design Overview," in *AAS/AIAA Space Flight Mechanics Meeting*, 2006.

[74] O. Grasset, M. Dougherty, A. Coustenis, E. Bunce, C. Erd, D. Titov, M. Blanc, A. Coates, P. Drossart, L. Fletcher, *et al.*, "JUpiter ICy moons Explorer (JUICE): An ESA Mission to Orbit Ganymede and to Characterise the Jupiter System," *Planetary and Space Science*, vol. 78, pp. 1–21, 2013.

[75] C. R. Short, D. Blazevski, K. C. Howell, and G. Haller, "Stretching in Phase Space and Applications in General Nonautonomous Multi-Body Problems," *Celestial Mechanics and Dynamical Astronomy*, vol. 122, no. 3, pp. 213–238, 2015. DOI: 10.1007/s10569-015-9617-4.

[76] W. S. Koon, J. E. Marsden, and S. D. Ross, "Constructing a Low Energy Transfer," in *Celestial Mechanics: Dedicated to Donald Saari for His 60th Birthday: Proceedings of an International Conference on Celestial Mechanics, December 15-19, 1999, Northwestern University, Evanston, Illinois*, American Mathematical Soc., vol. 292, 2002, p. 129.

[77] D. Canales, K. C. Howell, and E. Fantino, "Moon-To-Moon Transfer Methodology for Multi-Moon Systems in the Coupled Spatial Circular Restricted Three-Body Problem," in *AAS/AIAA Astrodynamics Specialist Conference*, 2020, pp. 1–20.

[78] D. Canales, M. Gupta, B. Park, and K. Howell, "Exploration of Deimos and Phobos Leveraging Resonant Orbits," in *31st AAS/AIAA Space Flight Mechanics Meeting*, 2021.

[79] H. Chen, E. Canalias, D. Hestroffer, and X. Hou, "Stability Analysis of Three-Dimensional Quasi-Satellite Orbits around Phobos," in *69th International Astronautical Congress, IAC*, 2018.

[80] M. S. Wallace, J. S. Parker, N. J. Strange, and D. Grebow, "Orbital Operations for Phobos and Deimos Exploration," *AIAA/AAS Astrodynamics Specialist Conference 2012*, 2012.

[81] M. Zamaro and J. D. Biggs, "Natural Motion around the Martian Moon Phobos: the Dynamical Substitutes of the Libration Point Orbits in an Elliptic Three-Body Problem with Gravity Harmonics," *Celestial Mechanics and Dynamical Astronomy*, vol. 122, no. 3, pp. 263–302, 2015.

[82] Y. Wang and X. Wu, "Analysis of Phobos' Dynamical Environment Considering Effects of Ephemerides and Physical Libration," *Monthly Notices of the Royal Astronomical Society*, vol. 497, pp. 416–434, 2020. DOI: 10.1093/mnras/staa1948.

[83] P. J. Llanos, J. D. Jordan, G. Hintz, and M. S. Rivo, "Trajectory Analysis between Quasi-Periodic Orbits and the Lagrangian Points Around Phobos," *AIAA/AAS Astrodynamics Specialist Conference 2014*, 2014. DOI: 10.2514/6.2014-4349.

[84] E. Joffre, M. Zamaro, N. Silva, A. Marcos, and P. Simplıcio, "Trajectory Design and Guidance for Landing on Phobos," *Acta Astronautica*, vol. 151, pp. 389–400, 2018.

[85] A. L. Genova, D. Korsmeyer, L. Plice, M. Loucks, and F. Y. Yang, "Trajectory Design for the Phobos and Deimos & Mars Environment (PADME) Spacecraft," *AIAA/AAS Astrodynamics Specialist Conference, 2016*, pp. 1–12, 2016.

[86] F. Gonzalez-Franquesa, N. Ozaki, and Y. Kawakatsu, "Deimos Flyby Observation Analysis Using Resonant Flybys for the MMX Mission," in *31st AAS/AIAA Space Flight Mechanics Meeting*, 2021.

[87] "Optimal Low-Thrust Orbit Transfers with Eclipsing," *Optimal Control Applications and Methods*, vol. 36, no. 2, pp. 218–240, 2015. DOI: 10.1002/oca.2111.

[88] J. L. Shannon, M. T. Ozimek, J. A. Atchison, and C. M. Hartzell, "Q-law Aided Direct Trajectory Optimization for the High-Fidelity, Many-Revolution Low-Thrust Orbit Transfer Problem," *Advances in the Astronautical Sciences*, vol. 168, no. January, pp. 781–800, 2019.

[89] A. E. Petropoulos, "Simple Control Laws for Low-Thrust Orbit Transfers," in *AIAA/AAS Astrodynamics Specialist Conference*, 2003.

[90] S. Lee, P. von Ailmen, W. Fink, A. Petropoulos, and R. J. Terrile, "Design and Optimization of Low-Thrust Orbit Transfers," in *2005 IEEE Aerospace Conference*, 2005.

[91] G. I. Varga and J. M. Sánchez Pérez, "Many Revolution Low-Thrust Orbit Transfer Computation Using Equinoctial Q-law Including J2 and Eclipse Effects," *AIAA/AAS Paper*, 2016.

[92] J. A. Ojeda Romero and K. C. Howell, "Transfers from GTO to Sun-Earth Libration Orbits," in *AAS/AIAA Astrodynamics Specialist Conference*, Portland, Maine, 2019.

[93] G. Mingotti, F. Topputo, and F. Bernelli-Zazzera, "Earth-Mars Transfers with Ballistic Escape and Low-Thrust Capture," *Celestial Mechanics and Dynamical Astronomy*, vol. 110, no. 2, pp. 169–188, 2011.

[94] P. Pergola, K. Geurts, C. Casaregola, and M. Andrenucci, "Earth-Mars Halo to Halo Low Thrust Manifold Transfers," *Celestial Mechanics and Dynamical Astronomy*, vol. 105, no. 1, pp. 19–32, 2009. DOI: 10.1007/s10569-009-9205-6.